Dissertation
submitted to the
Combined Faculties for the Natural Sciences and for Mathematics
of the Ruperto-Carola University of Heidelberg, Germany
for the degree of
Doctor of Natural Sciences

presented by

Diplom-Physicist: Fereidoun Rezanezhad

born in: Ramsar, Iran

Oral examination: May 23, 2007

Experimental Study of Fingering Flow in Porous Hele-Shaw Cells

Referees: Prof. Dr. Kurt Roth
Prof. Dr. Bernd Jähne

Zusammenfassung

Mit dem Ziel, die physikalischen Prozesse der Bildung von Flussinstabilitäten (fingering) in zwei Dimensionen zu untersuchen, wurden in Laborexperimenten vertikale Infiltrationsexperimente in geschichtetem Sand mit Hilfe von Hele-Shaw Zellen durchgeführt. Es wurde eine Lichttransmissions-Methode entwickelt, um die Dynamik der Wassersättigung innerhalb der Fließfinger detailliert, mit hoher räumlicher und zeitlicher Auflösung zu untersuchen. Die Methode wurde mit Hilfe von Röntgen-Absorptionsmessungen kalibriert. Die bei der Lichttransmission auftretenden Streueffekte wurden über eine Dekonvolution mit Hilfe der Punktbildfunktion korrigiert. Dies ermöglicht quantitative, räumliche hoch aufgelöste Messungen. Nach der vollständigen Entwicklung der Finger wurde ein Farbstoff aufgegeben, um mobile und immobile Anteile des Wassers unterscheiden zu können. Vollständig entwickelte Finger bestehen aus einer Fingerspitze, einem Kern aus mobilem Wasser und einem Rumpf aus immobilem Wasser. Es wurde die Dynamik der Wassersättigung innerhalb der Fingerspitze, entlang des Kerns und im Bereich des Randes während seines radialen Wachstums untersucht. Dabei konnten vorausgegangene Untersuchungen bestätigt werden, die ein Überschwingen der Sättigung im Bereich der Fingerspitze zeigten. Weiterhin wurde ein Sättigungsminimum direkt hinter der Spitze als neues Phänomen gefunden. Die Entwicklung eines Fingers lässt sich durch einen sukzessiven Anstieg des Wassergehaltes innerhalb des Fingerkerns hinter dem Minimum sowie eine kontinuierliche Verbreiterung bis hin zu einem quasi-stabilen Zustand charakterisieren. Dieser Zustand ist erst lange Zeit nach der Entwicklung des Fingers erreicht. In diesem Stadium lässt sich ein Kern mit einem schnellen konvektiven Fluss sowie ein Rand mit zunehmend langsamerem Fluss feststellen. Sämtliche beobachteten Phänomene, außer des Überschwingens der Sättigung, konnten mit der hysteretischen Natur der Boden-Wasser-Charakteristik erklärt werden.

Abstract

With the aim of studying the physical process concerning the unstable fingering phenomena in two dimensions, experiments of vertical infiltration through layered sand were carried out in the laboratory using Hele-Shaw cells. We developed a light transmission method to measure the dynamics of water saturation within flow fingers in great detail with high spatial and temporal resolution. The method was calibrated using X-ray absorption. We improved the measured light transmission with correction for scattering effects through deconvolution with a point spread function which allows us to obtain quantitative high spa-

tial resolution measurements. After fingers had fully developed, we added a dye tracer in order to distinguish mobile and immobile water fractions. Fully developed fingers consist of a tip, a core with mobile water, and a hull with immobile water. We analyzed the dynamics of water saturation within the finger tip, along the finger core behind the tip, and within the fringe of the fingers during radial growth. Our results confirm previous findings of saturation overshoot in the finger tips and revealed a saturation minimum behind the tip as a new feature. The finger development was characterized by a gradual increase in water content within the core of the finger behind this minimum and a gradual widening of the fingers to a quasi-stable state which evolves at time scales that are orders of magnitude longer than those of fingers' evolution. In this state, a sharp separation into a core with fast convective flow and a fringe with exceedingly slow flow was detected. All observed phenomena, with the exception of saturation overshoot, could be consistently explained based on the hysteretic behavior of the soil-water characteristic.

Contents

List of Figures

List of Tables

List of Symbols and Abbreviations

This list contains the most important symbols and notations used. The dimension is indicated in brackets. The mathematical structure of symbols is indicated by their typographical appearance:

a	scalar
$\mathbf{a}$, $\widehat{\mathbf{a}}$	vector, unit length vector
A	tensor
sin	standard function

Subscripts usually refer to a component of a vector (x, y, z, or 1, 2, 3) or to the phase (air, $water$, $matrix$).

The arguments of functions are suppressed if they are clear from the context, e.g., $\frac{\partial}{\partial x} f$ instead of $\frac{\partial}{\partial x} f(x)$. They are written, however, if the dependence on an argument is emphasized, e.g., $A(\theta(z))$ for a vertical profile that depends on the water content.

The pressure is sometimes given in units of [cm] or [cmWC] which means the pressure of a hanging water column with the same height.

Below L stands for length, T for time, and M for mass.

Sign Convention

The vertical (z) axis points downward, in the direction of the acceleration of gravity. Its origin is typically chosen at the soil surface. Accordingly, z is called the depth.

Lowercase Latin Symbols

$\mathbf{g}$	acceleration of gravity [$\mathrm{L\,T^{-2}}$]
$\mathbf{j}_\mathrm{w}$	volume flux of water [$\mathrm{L\,T^{-1}}$]
h	matric head [L]
p	pressure [$\mathrm{M\,L^{-1}T^{-2}}$]
p_a	pressure in air phase [$\mathrm{M\,L^{-1}T^{-2}}$]

p_w pressure in water phase [M $L^{-1}T^{-2}$]
p_{wt} threshold water pressure [M $L^{-1}T^{-2}$]
r pore radius [L]
$\mathbf{v}$ velocity [L T^{-1}]
x position [L]

Uppercase Latin Symbols

A light absorption moduli
Bo bond number
Ca capillary number
$\mathbf{F}$ force [M L T^{-2}]
I light intensity [counts]
I_0 measured light intensity without any porous material (input light) [counts]
I_d measured intensity of the dark image [counts]
K hydraulic conductivity tensor [$M^{-1}L^3T$]
K_s hydraulic conductivity at water saturation [L^3T^{-1}]
M viscosity ratio
n refractive indices
S saturation [–]
τ light transmission factor
V volume [L^3]

Lowercase Greek Symbols

ψ_g gravitional potential [M $L^{-1}T^{-2}$]
ψ_w water potential [M $L^{-1}T^{-2}$]
ψ_m matric potential [M $L^{-1}T^{-2}$]
ρ mass density of soil sample [M L^{-3}]
ρ_w mass density of water [M L^{-3}]
θ volumetric fraction [–]
θ_w volumetric water content of water phase [–]
θ_s volumetric water content at saturation [–]

θ_r residual volumetric water content [–]

ϕ porosity of porous media [–]

η viscosity [M $T^{-1}L^{-1}$]

σ surface tension [M T^{-2}]

μ X-ray absorption coefficient, the subscripts will indicate the material [L^{-1}]

Mathematical Notation

$\frac{d}{dt}$ total derivative with respect to time [T^{-1}]

$\frac{\partial}{\partial t}$ partial derivative with respect to time [T^{-1}]

∇ partial derivative with respect to space [L^{-1}]

Abbreviations

HSI system to specify the color space Hue, Saturation, Intensity

LTM Light Transmission Method

PSF Point Spread Function

RGB system to specify the color space Red, Green, Blue

1. Introduction

The study of water flow and transport in porous media has applications in many disciplines such as fate and transport of chemicals, and plant-root activity, dissolved contaminants and non-aqueous phase liquids in soils and it is of fundamental importance in hydrologic science. Of particular interest is the unsaturated zone, the so-called vadose zone, found between the ground surface and the groundwater table. The most important processes in this zone include evaporation, plant-soil interactions, water infiltration, and contaminant transport. These processes control the formation of groundwater, the transport of chemicals, and various remediation technologies. Soil physicists and hydrologists have given an enormous attention to the problem of infiltration and redistribution of water in soil. Redistribution of water in soil following infiltration is important because it determines the amount of water held near the surface for subsequent use by plants.

Due to different types of geological media in the unsaturated zone (ranging from relatively homogeneous sand to heterogeneous fractured media.), it is generally accepted that water and solutes may flow through the unsaturated zones via preferential paths until they reach groundwater. Preferential flow in the vadose zone is the focusing of flow into narrow channels. The flow through preferential paths is extremely important in agriculture, in the hydrological processes of infiltration and in the transport of agrochemicals through the soil profile. The important aspect of preferential flow is that water, as well as pollutants dissolved in it, can infiltrate downward through such pathways much faster than predicted by homogeneous flow with plane wetting fronts.

The term preferential flow actually describes three different processes: macropore, funnel and fingered flow. Macropore flow refers to water passing through some preferred path such as decayed roots and earthworm paths. Funnel flow occurs when the downward water flow gets funneled or diverted toward a preferred direction because of impermeable layers. Fingered flow occurs in a perfect homogeneous sandy porous media, where the wetting front breaks up like a flame front. It refers to an instability of the interface between two immiscible fluids when one invades the other. Early examples were air invading water and water invading oil where the instability results from a difference in the viscosity.

More recently, fingered flow in porous media was studied, both in petroleum industry to better understand oil recovery and in environmental sciences as an instance of preferential flow of water through soil. The latter is of obvious interest for the general understanding of various hydrological aspects including the quantity and quality of groundwater recharge or the efficiency of irrigation. Fingered flow is also of fundamental interest, however, since it challenges our understanding of multiphase flow in porous media.

Unstable flow of water during infiltration was first reported by Hill (1952). The fingering phenomenon has been the subject of numerous experimental studies. Hill and Parlange (1972) examined instability of the wetting front in layered soils by direct visual observation of the flow field through transparent panels. Diment and Watson (1985) described laboratory results for front infiltration into layered soils with different uniform initial moisture contents. Glass *et al.* (1989a) and Liu *et al.* (1993) found that if the moisture content was spatially variable as a result of an earlier infiltration with fingered flow, the previous finger paths were preserved during subsequent infiltration cycles because of hysteresis in the soil moisture characteristic curve. Selker *et al.* (1992a) reported a study of matric potential and finger development as functions of time, using a homogeneous sand. The occurrence and types of fingering flow in homogeneous soils, however, is sensitive to many factors such as initial water content, size and distribution of soil particles, rainfall intensity, water repellency and so on. This was studied by Diment and Watson (1985), Baker and Hillel (1990), Selker *et al.* (1992b), Dekker and Ritsema (1994), Yao and Hendrickx (1996) and DiCarlo (2004). It has also been observed a phenomenon where the saturation and pressure profiles within the fingers are inverted for certain initial and boundary conditions (Geiger and Durnford 2000, DiCarlo 2004). This is often called "saturation overshoot" as there exists a high water saturation followed by region with a low water saturation directly behind the wetting front.

The theoretical analysis of wetting front instability has been studied for many years. Most of the studies were based on the stability analysis of the classic governing equation for unsaturated flow through porous media (Hill and Parlange 1972, Raats 1973, Philip 1975a, Diment *et al.* 1982, Glass *et al.* 1989a). Many mathematical models have been developed to attempt to model the saturation overshoot and it has been shown that this phenomenon simply cannot be described by the Richards' equation with standard non-monotonic pressure-saturation curves (Eliassi and Glass 2001, Egorov *et al.* 2003, DiCarlo 2005). This is because of the parabolic nature of the Richards' equation, which requires the saturation to move continuously from the initial low saturation to the final saturation. Implicit in the Richards' equation is the fact that one can

define a length scale where properties such as porosity, conductivity, and saturation can be considered continuous. More exactly, the continuum description of the phenomena only fails at the wetting front where there is a jump from the initial low saturation to a high saturation. Behind this jump, Richards' equation has been shown to describe the flow behavior well Selker *et al.* (1992b). Although, it has been argued that additional continuum terms are necessary, in particular for when the local saturation changes quickly (Eliassi and Glass 2002; 2003, DiCarlo 2005). Some simulation and conceptual models have been used for the mechanisms of finger formation, propagation and persistence in unsaturated porous media and calculating the size and speed of the fingered preferential flow (Wang *et al.* 1998, Jury *et al.* 2003). Therefore, the theory of the fingered flow is still under development and not understood well.

Laboratory measurements of soil moisture are of great interest in soil science and are limited by the ability to measure dependent variables in heterogeneous and/or transient systems. A number of tools for nondestructive measurement of water saturation in the laboratory have been developed. Advanced methods for visualization and imaging of flow and transport in porous media are Magnetic Resonance Imaging (MRI), X-ray Computed Tomography (XCT), Neutron Computed Tomography (NCT), and Gamma-ray Computed Tomography (GCT). Each of these methods for measuring saturation within laboratory test cells is limited in spatial or temporal resolution or in size of the sample and requires very specialized and expensive equipment. In this study, we applied the very simple visible light transmission laboratory techniques of Glass *et al.* (1989c) for mapping the water content at high spatial and temporal resolutions in a thin porous Hele-Shaw cell. The 3 mm thin and thus translucent sand sample was placed in front of a constant light source and images were recorded with a digital camera. The Light Transmission Method (LTM) captures the spatial resolution of the water content and can provide new insights into rapidly changing, two-phase and three-phase flow systems.

This research presents the development and application of the LTM for two-phase flow, aimed at investigating unstable fingered flow in a sand-air-water system. We established a Hele-Shaw cell where a layer of fine-textured sand was placed on top of a coarse-textured sand and studied experimentally the flow paths and instabilities of gravity driven fingers through an initially dry porous medium. We used the intensity of transmitted light through the Hele-Shaw cell to measure water saturation, since water saturation is a function of light intensity.

The overall objectives of the present study has been to advance: 1) infiltration experiments in a large Hele-Shaw cell to observe fingering flow patterns

during redistribution, 2) our understanding of the special and interesting case of water infiltration through porous media (fingered flow), 3) realistically describing this type of flow using the relevant physical processes, 4) understanding of two crucial phenomena for fingering flow (i) the observed saturation overshoot which initializes a finger and (ii) the hysteresis of the soil-water characteristic which stabilizes it by dramatically reducing lateral flow, and 5) application of a visualization and monitoring method (LTM) with high spatial and temporal resolution to characterize multiphase and transient flow in porous media.

Outline

The thesis is divided in the following order. In chapter Theoretical Background (2), first an overview of the theoretical background and fundamental principles of water flow in porous media is illuminated (sec. 2.1). Section 2.2 describes the physical phenomena of viscous, gravity and capillary forces. Different visualization and imaging methods to visualize the flow and transport are described in sec. 2.3. In section 2.4, the different terms of preferential flow and a history of this type of flow is reviewed.

A description of the experimental setup, used materials and methods together with a detailed description of the calibration process using X-ray absorption are presented in chapter 3.

Readers who are familiar with the physics of image analysis may continue directly to the next chapter, Image Processing (4). The purpose of this chapter is to provide an accurate and complete presentation of the image processing applied in this study. In section 4.2 an advanced and improved process for the LTM is presented, where a deconvolution is applied on images to correct for the scattering effect occurring during the transmission of light through porous materials.

The results of our experiments and analysis are presented in the fifth chapter, Results and Discussion (5). All essential results with a complete discussion of the experimental evidences are given here. Section 5.2 and 5.3 describe the physical explanation of the finger initiation and the saturation overshoot phenomenon. After the qualitative description, quantitative analysis of measurements of finger behavior, including dynamics of water saturation and pressure in flow fingers, dynamics and stabilization of fingers, finger width, and finger tip velocity under different conditions are presented. Further experiments follow in section 5.7 and 5.8 and 5.9.

Finally, there is a short closing chapter, Summary and Conclusions (6) where the whole work is summarized.

2. Theoretical Background

Over the years, there has been considerable interest in the multiphase fluid flow and transport phenomena in the unsaturated and saturated zones of the subsurface environment. Many of the current pressing problems of single-phase flow and very complex processes of multiphase flow involve flow and transport issues including preferential flow development, groundwater contamination and subsurface storage of materials. Unsaturated hydrology has gained increased attention within the last decades. Different geological material is found in the unsaturated zone, ranging from relatively homogeneous sand to heterogeneous fractured media. Within all these different types of media preferential flow and transport have been observed. Preferential flow paths significantly increase the vertical water and solute velocity which in turn may lead to the rapid movement of harmful chemicals and microbial organisms. These flow paths may arise as a result of fluid instabilities, created by density or viscosity differences, or because of capillary and gravity effects.

The following chapter will briefly introduce the reader to the different physical aspects of flow in porous media. In the first section we will have an introduction and review on the fundamental principles and scientific progress in the case of water flow through saturated and unsaturated porous media. The second section presents the physical phenomena of viscous, gravity and capillary effects to generation of stable and unstable flow conditions. Section 2.3 introduces the different methods for visualization and imaging of transient flow phenomena. Section 2.4 describes three different types of preferential flow in unsaturated porous media.

2.1. Water Flow through Porous Media

A porous medium consists of a matrix with a large amount of microscopic pores and throats. The pores are typically connected such that there are narrow tubes through which one or more fluids (e.g. water, oil and gas) can pass through. The flow process in porous media is very complex. The reasons for the complexity are many, but a major factor is the intricate nature of the pore spaces between matrix material. Such a matrix and pore space configuration can be found in a

lot of materials, like soils, rocks, cemented sandstones, foam rubbers and many others. The pores tend to have irregular surfaces, which is one of the reasons why fluid flow through them is so complex.

The fundamental equation governing motion of fluid substances such as liquids and gases in a medium at the pore-scale is the well-known Navier-Stokes equations. These equations established using the Newton's law into the conservation law of linear momentum (acceleration). The external forces $\mathbf{F}_{\mathrm{i}}^{ext}$ acting on a moving fluid element of arbitrary volume $\triangle V$ are pressure ($\mathbf{F}_p$), dissipative viscosity ($\mathbf{F}_v$) and gravity ($\mathbf{F}_g$). The momentum $m\mathbf{v}$ of the fluid element is $[\int_V \rho\, dV]\mathbf{v}$, where $\mathbf{v}$ is the velocity vector and ρ is the density of fluid. The rate of change of the momentum is $m\, d\mathbf{v}/dt$ and by definition the mass of a fluid element remains constant. Thus, the Navier-Stokes equations are a dynamical statement of the balance of forces acting at any given region of the fluid. hence

$$m\,\frac{d\mathbf{v}}{dt} = \sum_{\mathrm{i}} \mathbf{F}_{\mathrm{i}}^{ext}$$

$$\left[\int_V \rho\, dV\right]\frac{d\mathbf{v}}{dt} = \overbrace{\mathbf{F}_g + \mathbf{F}_p + \mathbf{F}_v} = \int_V [\rho\mathbf{g} - \nabla p + \eta\nabla^2\mathbf{v}]dV \ , \tag{2.1}$$

where p is the pressure and η is the dynamic viscosity of the fluid. Since V is an arbitrary volume, this implies

$$\rho\,\frac{d\mathbf{v}}{dt} = \rho\mathbf{g} - \nabla p + \eta\nabla^2\mathbf{v} \ , \tag{2.2}$$

which is called the Navier-Stokes equation. Substituting the total derivative $\frac{d\mathbf{v}}{dt} = \frac{\partial\mathbf{v}}{\partial t} + \mathbf{v}\cdot\nabla\mathbf{v}$ leads to the Navier-Stokes equation for an incompressible Newtonian fluid

$$\rho\frac{\partial\mathbf{v}}{\partial t} + \rho[\mathbf{v}\cdot\nabla]\mathbf{v} = \rho\mathbf{g} - \nabla p + \eta\nabla^2\mathbf{v} \ . \tag{2.3}$$

Dividing it by the constant fluid density ρ, yields the kinematic form

$$\frac{\partial\mathbf{v}}{\partial t} + (\mathbf{v}\cdot\nabla)\mathbf{v} = \mathbf{g} - \frac{1}{\rho}\nabla p + \frac{\eta}{\rho}\nabla^2\mathbf{v} \ . \tag{2.4}$$

This equation describes the classical hydrodynamics of momentum conservation for an incompressible Newtonian fluid in the void space of a medium on the microscopic level with the known geometry of the solid phase and the accompanying surface properties (Roth 2006). This equation is a non-linear partial

differential equation and, in theory, it is too difficult to solve it analytically because of the non-linear term $(\mathbf{v} \cdot \nabla)\mathbf{v}$. During the last years much effort was made to find a general solution for the incompressible Navier-Stokes equations with spatial assumptions and boundary conditions.

Henry Darcy (1856), a French scientist seeking a means to design sand filters for drinking water, innovated the theoretical basis for quantifying the process of water flow through soil. He investigated the uniform flow of water through packed sand columns and introduced the well known Darcy Equation, which describes the apparent water velocity based on the discharge per unit area.

For a saturated medium the only resistivity to the fluid flow is given by the solid matrix. The so-called saturated hydraulic conductivity is influenced by the pore geometry and the fluid mobility. Conductivity of an unsaturated porous medium is additionally influenced by the presence of other fluids as they share the same pore space. In general, water flow through porous media can be considered into two regimes; the saturated and the unsaturated zones (Fig. 2.1).

2.1.1. Water flow through saturated porous media

The saturated zone is the region below an underlying water table. It is recharged by the percolation of water through the unsaturated zone that reaches the saturated zone. When soil is saturated, all the pores are filled with water and the water phase becomes continuous (Fig. 2.1). The most common example for a saturated zone is the groundwater region in an aquifer. When soils are saturated with isotropic homogeneous or anisotropic heterogeneous media, the flow of water in this zone is well described by Darcy's law. The flux density can then easily be obtained if the conductivity of the soil is known and the total potential or matric potential at the ends of the soil are specified. Darcy developed the following relationship for isotropic media where the volumetric water flux is proportional to the pressure gradient as

$$\mathbf{j}_{\mathrm{w}} = -K_{\mathrm{s}} \nabla p \ , \tag{2.5}$$

where $\mathbf{j}_{\mathrm{w}} = (j_{\mathrm{w,x}}, j_{\mathrm{w,y}}, j_{\mathrm{w,z}})$ is the volumetric water flux passing through the soil, K_{s} the saturated hydraulic conductivity and ∇p the applied pressure gradient vector as the driving force. Equation 2.5 is the so-called Darcy's law which describes the water movement in saturated materials.

This equation for the one-dimensional vertical flow can be simplified as

$$\mathbf{j}_{\mathrm{w,z}} = -K_{\mathrm{s,z}} \frac{\partial p}{\partial z} \ , \tag{2.6}$$

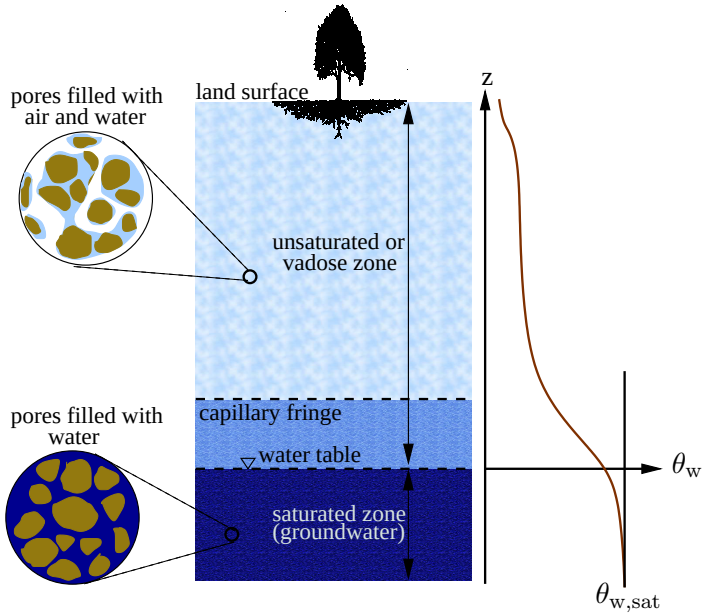

Figure 2.1.: Schematic cross-section of the saturated and unsaturated zones with a vertical distribution of soil moisture. The unsaturated zone is the part of the subsurface between the ground water table and the land surface where water content (θ_w) is typically small and the pores are partially filled with water and air. The saturated zone is below the water table and the pores are completely filled with water.

where z is the vertical distance, positive upwards, and the saturated hydraulic conductivity ($K_{s,z}$) depends on the fluid and solid material property.

When there are other driving forces (e.g. gravitation force) in addition to the negative pressure gradient, they can be included by replacing $\partial p/\partial z$ with the sum of all driving forces per unit volume. Darcy's law may be written as

$$\mathbf{j}_{w,z} = -K_{s,z}\left(\frac{\partial p}{\partial z} - \rho_w g\right) \quad , \tag{2.7}$$

where ρ_w is the density of water and g the gravitational acceleration constant.

2.1.2. Water flow through unsaturated porous media

The unsaturated zone, so-called vadose zone, is the portion of the subsurface from above the groundwater table to the land surface. In contrast to the saturated zone, the pores are partially filled with water (Fig. 2.1). Its thickness can range from 0, when a lake or marsh is at the surface, to hundreds of meters, as is common in arid regions. It is a zone that to a large degree controls the transmission of water to other substances, as well as to the land surface, to water on the surface, and to the atmosphere. The most important processes in the unsaturated zone include evaporation, plant-soil interactions, water infiltration, and transport. These processes control, e.g., the formation of groundwater, the transport of chemicals, and various remediation technologies. Water flow and chemical transport in unsaturated soils is a complex process and difficult to describe quantitatively. Since the hydraulic conductivities in unsaturated soils depend upon the heterogeneous nature of soil which often entail changes in the state and content of soil water during flow.

The flux density of water movement through saturated soil can be easily obtained if the saturated hydraulic conductivity of the soil is known and if the total considered soil volume potential is specified (Eq. 2.5). However, the problem becomes more difficult when the soil is unsaturated, i.e. when air is also present in the pores, and water infiltrates through partially saturated pores to the groundwater.

Edgar Buckingham (1907) extended Darcy's law (Eq. 2.5) to a more general form of flux law to describe flow through unsaturated soils yielding

$$\mathbf{j}_{\mathrm{w}} = -K(\theta_{\mathrm{w}})\nabla\psi_{\mathrm{w}} \ , \tag{2.8}$$

where $K(\theta_{\mathrm{w}})$ is the unsaturated hydraulic conductivity, which is sensitive and highly non-linear dependent on volumetric water content, θ_{w}, in contrast to the constant K_{s} in Eq. 2.5. The water potential ψ_{w} is the sum of the matric and gravitational potentials. This equation is called the Buckingham-Darcy flux law.

The more general case of unsteady or transient water flow (varies in time as well as space) in unsaturated soils is a highly dynamic phenomenon. At the macroscopic scale, the dynamics of water flow in unsaturated porous media is usually described by the highly non-linear Richards' equation (Richards 1931). This equation is represented quantitatively by a combination of Darcy's law (Eq. 2.9) and the conservation of mass law,

$$\frac{\partial}{\partial t}\theta_{\mathrm{w}} + \nabla \cdot \mathbf{j}_{\mathrm{w}} = 0 \ . \tag{2.9}$$

Inserting Eq. 2.8 into the Eq. 2.9 yields a formula which leads to the differential equation

$$\frac{\partial}{\partial t}\,\theta_{\mathrm{w}} - \nabla \cdot \Big[K(\theta_{\mathrm{w}})\nabla\psi_{\mathrm{w}}\Big] = 0 \ , \tag{2.10}$$

which includes two state variables. The water potential can be written as $\psi_{\mathrm{w}} = \psi_{\mathrm{m}} - \rho_{\mathrm{w}} g z$ where ψ_{m} is the matric potential that represents the pressure jump across the water-air interface and is negative for unsaturated soil. Hence, basically Richards' equation describes the one-dimensional uniform (equilibrium) form of unsaturated water movement through a partially saturated rigid porous medium and is written as

$$\frac{\partial}{\partial t}\,\theta_{\mathrm{w}} - \nabla \cdot \Big[K(\theta_{\mathrm{w}})[\nabla\psi_{\mathrm{m}} - \rho_{\mathrm{w}}\mathbf{g}]\Big] = 0 \ . \tag{2.11}$$

This equation was deduced with the assumptions that the effect of displaced air during infiltration can be neglected, and that air pressure and temperature are constant. Inserting $\theta(\psi_{\mathrm{m}})$, a typically strongly hysteretic water retention function, into Eq. 2.11 yields a form with one state variable as

$$C_{\mathrm{w}}(\psi_{\mathrm{m}})\,\frac{\partial}{\partial t}\,\psi_{\mathrm{w}} - \nabla \cdot \Big[K(\psi_{\mathrm{m}})[\nabla\psi_{\mathrm{m}} - \rho_{\mathrm{w}}\mathbf{g}]\Big] = 0 \tag{2.12}$$
$$\text{with} \quad C_{\mathrm{w}}(\psi_{\mathrm{m}}) := \frac{\partial\theta}{\partial\psi_{\mathrm{m}}} \ ,$$

where $C_{\mathrm{w}}(\psi_{\mathrm{m}})$ is the soil water capacity function. This equation is called the potential or ψ-form of Richards' equation. And when matric potential is expressed in terms of matric head $h = \psi_{\mathrm{m}}/\rho_{\mathrm{w}} g$, Eq. 2.12 changes into

$$C^{*}_{\mathrm{w}}(h)\,\frac{\partial}{\partial t}\,h - \nabla \cdot \Big[K(h)[\nabla h + 1]\Big] = 0 \tag{2.13}$$
$$\text{with} \quad C^{*}_{\mathrm{w}}(h) := \frac{\partial\theta}{\partial h} \ ,$$

(Roth 2006). Since Richard's equation is a non-linear partial differential equation, it generally can not be solved directly but only by some approximations and numerical methods.

A mathematical description of water flow and transport in the unsaturated zone by Richards' equation requires knowledge of two functional relationships characterizing the soil: (1) the unsaturated hydraulic conductivity function, $K(\theta_{\mathrm{w}})$, and (2) the soil-water retention function, $\theta(\psi_{\mathrm{m}})$. The functional relationships have been parameterized by several researchers, where the most common applied model is by Brooks and Corey (1966) and van Genuchten (1980).

Simulation of water dynamics in this zone requires input data including the model parameters, the geometry of the system, the boundary conditions and, when simulating transient flow, initial conditions. A complete theoretical details can be found in several textbooks, e.g. (Bear 1972, Jury *et al.* 1991, Kutìlek and Nielsen 1994, Roth 2006).

2.1.3. Infiltration with wetting front through porous media

Water infiltrating downward into dry unsaturated soils forms the air-water interface which, in soil physics, is called the wetting front. A knowledge of the structure of the wetting front is very important for predicting wetting front propagation through soil, which in turn makes it possible to predict both deep-soil and ground water pollution. When water is poured in excess at the top of a soil column, the water will flow into the soil due to the gravitational forces at a rate depending on the water flux, water content in the column and the physical properties of the soil. In the first stage the moisture profile gradually changes, but later, in a column of uniform soil that is initially at a constant moisture content, it maintains a fixed profile which moves downwards at constant speed. Infiltration is defined as the initial process of water entering the soil resulting from application at the soil surface. Downward infiltration into an initially unsaturated soil generally occurs under the combined influence of capillary and gravity gradients where capillary forces are dominated by gravity forces. Three different zones can be assumed during infiltration into a soil column: a saturated zone with constant water content θ_s (except for entrapped air), a transition zone where moisture content decreases rapidly from θ_s to θ_i (initial water content) with depth and the wetting front zone which is a zone of a very steep moisture gradient (Fig. 2.2).

Green and Ampt (1911) neglected the evolution of the infiltration front during the initial stage of the infiltration. They quantitatively reproduced the temporal change of the infiltration flux and of the depth profile of the water. Green and Ampt assumed a homogeneous soil and an infiltration wetting front that is sharp. This model is also called "plug flow" or "piston flow" model. The water content profile is piston-type with a well-defined wetting front. The piston-type model assumes the soil is saturated at a volumetric water content of θ_s down to the wetting front. At the wetting front, the water content drops abruptly to an antecedent value of θ_i.

Raats (1973) studied the infiltration process with wetting front instability for Green and Ampt flow, i.e. infiltration with a sharp front separating the dry from the wetted soil. He noted that the wetting front would break up into

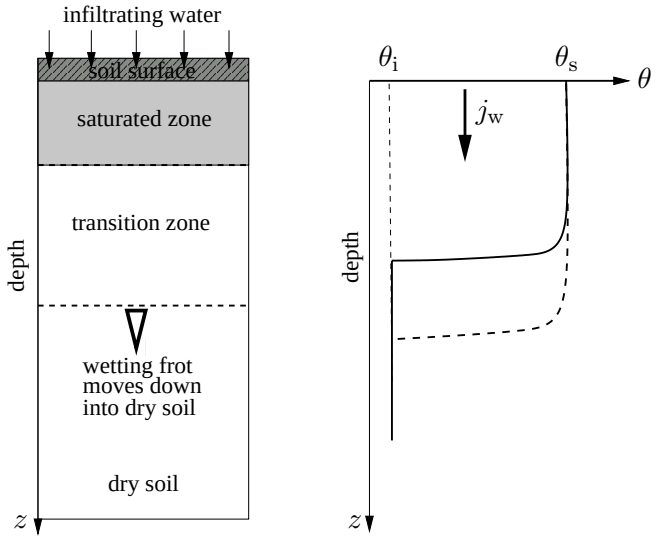

Figure 2.2.: **Left**: Moisture zones during infiltration and **Right:** Illustration of transient one-dimensional infiltration following the Green-Ampt approach with conceptualized water content profile, which demonstrated the sharp wetting front during water infiltration through soils.

fingers if the velocity of the front increased with depth. He also found that infiltration of water into a soil without the possibility for air to escape would lead to an unstable front with downward moving fingers of water inter-spaced with fingers of air moving up. For different cases he derived criteria that must be satisfied for the wetting front to become unstable.

2.1.4. Hysteresis of soil water-retention function

The most basic information on water in an unsaturated medium is water content or wetness. It is defined as the volume of water per bulk volume of the medium. Water is held in an unsaturated medium by forces whose effect is expressed in terms of the energy state or pressure of the water, the so-called matric pressure or matric potential. It is the pressure of water in a pore of an unsaturated medium relative to the air pressure ($\psi_m = p_w$-p_a), where p_w is the water pressure and p_a is the air pressure. In an unsaturated medium, the water is generally at lower pressure than the air, so the matric potential is negative. Higher water content is related with higher matric poten-

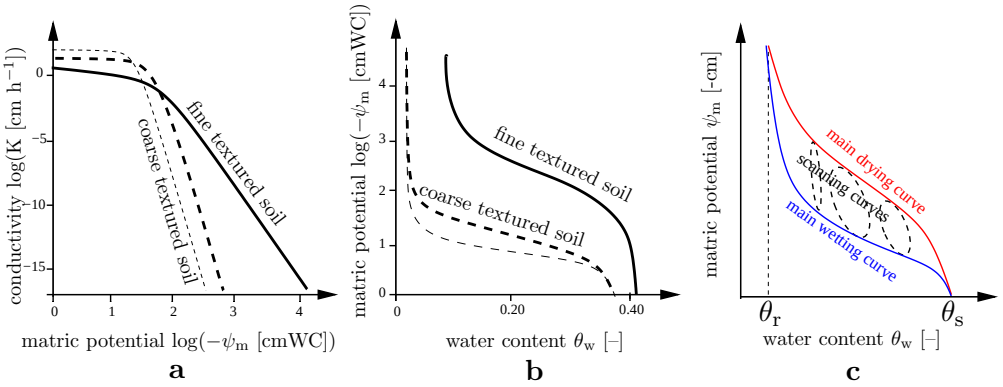

Figure 2.3.: **a,b**) Typical hydraulic conductivity function and soil-water characteristic curves for two different classes of the fine-textured soil, e.g. loamy soil, (solid line) and a coarse-textured soil, e.g. sandy soil, (dashed line). The thin dashed line represents a sand with larger grains and thus, larger pores. **c**) The main soil-water characteristic curves for wetting and drying (solid lines), and three sets of scanning curves (dashed lines) in hysteresis loop.

tial and as matric potential decreases the water content decreases, but in a way that is non-linear and hysteretic. Figure 2.3a,b shows typical shapes of conductivity-pressure and pressure-saturation relationships of a coarse textured porous medium , e.g. sandy soil, and a fine textured porous medium, e.g. loamy soil, for a drainage cycle. As the soil is finer dispersed the soil-water interaction forces are greater. This means that in the same humidity conditions, clays have considerably higher values of soil suction in comparison to sands. The curve showing the relationship between water content and matric potential, $\theta(\psi_m)$, for a soil is called soil-water characteristic curve or retention curve, which is characteristic for a porous medium that depends on the nature of its pores. This relation strongly influences the movement of water and other substances in unsaturated media.

There are two branches defining the soil-water characteristic curve. One is related to wetting whereas the other to drying. Spatial variations in soil properties dominate over hysteretic effects. In order to describe the hysteretic behavior of a particular soil, many wetting and drying experiments have been performed during the last years (Topp and Miller 1966, Parlange 1976b, Jaynes 1992, Lehmann *et al.* 1998), because the water-retention function may change with each drying and wetting process. Thus, a theory is needed to estimate

the water-retention function for any drying and wetting loop based on the envelope of main drying and wetting curves. The main drying curve (drainage equilibrium curve) describes the drying from the highest reproducible saturation degree (θ_s), which is usually not complete due to entrapped air, to the residual water saturation (θ_r). The main wetting curve (imbibition equilibrium curve) describes the wetting from the residual water content to the highest saturation degree. Starting from a boundary wetting or drying curve, a sequence of wetting and drying cycles can be expressed by scanning curves in primary, secondary or higher order. According to the hysteresis function, the drying scanning curves are scaled from the main drying, and wetting scanning curves from the main wetting curves (Fig. 2.3c). The hysteresis effect is caused by different radii of the controlling pores and different contact angles for wetting and drying processes.

2.1.5. Multiphase flow in porous media

Darcy's equation is an empirical macroscopic equation based on average quantities and derived for one-dimensional single-phase flow. Oftentimes, fluid flow in porous media involves more than one fluid and the difficulties arise when describing two or multi-phase flow in porous media. In case of a single-phase system the pore space of the porous medium is filled by a single fluid (e.g. water) and in a multiphase system the pore space is filled by two or more fluids (e.g. air, water, oil, etc.). Multiphase flow is a very complex physical phenomenon, where many flow types can occur (e.g. gas/solid, gas/liquid, liquid/liquid and solid/liquid) and with each flow type, several possible flow regimes can exist.

Two general types of fluid displacement are possible when two or more fluids in motion occupy a porous medium (Bear 1972):

- **Miscible displacement:** In this process, a fluid is displaced in a porous medium by another fluid that is miscible with the first one. The two fluids are completely soluble in each other. The interfacial tension between the two fluids is zero and the fluids dissolve in each other. Therefore, in this type of displacement, there is no capillary effect, but instead there is dispersive mixing between the two fluids which can play an analogous role. In miscible displacement, when two fluids are in contact with each other, a transition zone due to hydrodynamic dispersion is immediately created. The composition of the fluids varies from one to the other fluid across the zone. This makes the miscible displacement a very efficient

recovery procedure, where the elimination of capillary forces might lead to a total recovery of the displaced phase.

- **Immiscible displacement:** This process is a transient process where one fluid displaces another fluid from a porous medium with no mixing at the interface. It is a simultaneous flow of two or more immiscible fluids or phases in the porous medium. The interfacial tension between the two fluids is non-zero and a distinct fluid-fluid interface separates the fluids within each pore. The flow of immiscible fluids in a porous medium can be conveniently subdivided into two types: steady-state, where all the macroscopic properties of the system are time independent at all points, or unsteady-state where the fluid and flow properties change with time. In equilibrium (steady-state) flow of immiscible fluids, the saturation of the medium with respect to all fluids contained in the system is constant at all points. Therefore, in steady-state flow there is no displacement of any fluid by any of the other fluids in the pores. This means each fluid flows through its own path without affecting the flow of the other fluids. However, in unsteady-state flow, the saturation at a given point in the system is changing with time.

On the microscopic level the sharp interfaces between fluid phases give rise to a capillary force that plays an important role in multiphase flows. When two immiscible fluids are in contact within the interstices of a porous medium, a discontinuity in pressure across the interface separates them. Its magnitude depends on the interface curvature at that point. The difference between the phase pressure of the two fluids is called capillary pressure. It is an important parameter to quantify multiphase flow in porous media. At equilibrium, this pressure (p_c^{eq}) is the difference between the pressure in the non-wetting and the wetting phase:

$$p_c^{\mathrm{eq}} = p_{\mathrm{nw}} - p_{\mathrm{w}} \ , \tag{2.14}$$

where nw and w label the non-wetting and wetting phases, respectively. These differences occur because, in a confined geometry, the contact angles cause a curvature of the fluid interface and thus a capillary pressure difference between the two phases. At equilibrium, this pressure difference can be given through the Young-Laplace equation and it depends on the interfacial tension between the fluids (σ_{12}) and the principal radii of curvature of the surface, r_1 and r_2, as shown:

$$\triangle p_{12} := p_2 - p_1 = \sigma_{12} \left(\frac{1}{r_1} + \frac{1}{r_2} \right) = \frac{2\sigma_{12}}{r^*} \ , \tag{2.15}$$

where r^* is the mean radius of curvature ($2/r^*=1/r_1+1/r_2$). The capillary pressure is thus a measure of the tendency of a porous medium to suck in the wetting fluid phase or to repel the non-wetting phase. The direction and magnitude of this pressure depends on the interface geometry at any particular instant in time. The interface is dynamically deforming or has arrived at a stable equilibrium shape.

When two fluids are simultaneously present, the ability of one fluid to flow depends on the local configuration of the other. Depending on the wetting properties of the fluids, there are two basic terms of displacement in two-phase flow in porous media to describe the fluid displacements: drainage and imbibition. The two processes are due to different mechanisms and usually result in completely different pressure and saturation profiles. In the imbibition (displacement of non-wetting fluid by the wetting fluid or increase in wetting phase saturation) the wetting fluid invades. The capillary pressure difference creates a driving force such that the invading fluid spontaneously imbibes until it is balanced by hydrostatic pressure. For drainage (displacement of wetting fluid by the non-wetting invading fluid or reduction of wetting phase saturation), the pressure at an invading interface must rise above the pressure in the adjacent displaced fluid by an amount that allows the interface to deform to the curvature of the local pore.

The dynamic saturation during a displacement process and the final average saturation that is left behind after displacement, are important parameters. In many processes, they are important either directly or because of their effect on other quantities. Saturation is affected by how uniformly a displacement front moves through the medium and the amount of displaced fluid that is trapped behind the front. The displacement pattern depends on the morphology of the medium, mobility ratio, wettability, and the balance between gravity, capillary and viscous forces. For any medium and specific fluids, the gravity, capillary and viscous forces alone dictate the displacement.

2.2. Physical Phenomena of Viscous, Gravity and Capillary Forces

Depending on the conditions of drainage displacement, the process where a non-wetting fluid displaces a wetting fluid, different flow regimes may be observed. This process provides pattern formations between the interface of the two fluids and the different structures obtained can be divided into two main flow regimes of stable and unstable displacement. Before discussion on the

properties of these two regimes, to quantify the relative importance of various driving forces in flow domain, we employ three dimensionless numbers using three type of forces in two-phase fluid displacements: viscous forces in the displacing fluid ($\mathbf{F}_v = \eta_2[v/r]r^2$), capillary forces due to the interface ($\mathbf{F}_c = \sigma r$) between them and gravity forces ($\mathbf{F}_g = \rho g r^3$), where η_1 and η_2 refer to the viscosity of the displaced and displacing fluid, respectively, v is the velocity, σ is the surface tension, ρ is the fluid density, r is the microscopic length scale of grain, and g is the gravitational acceleration constant. This leads to three dimensionless numbers that characterize the different properties of immiscible displacement in porous media: the capillary number (Ca), the bond number (Bo), and the viscosity ratio (M). The capillary number describes the relative magnitude of viscosity over capillary forces, the bond number describes the relative magnitude of gravity over capillary forces and the viscosity ratio gives the ratio of the two viscosities, as

$$\mathrm{Ca} = \frac{\mathbf{F}_v\,(\text{viscous forces})}{\mathbf{F}_c\,(\text{capillary forces})} = \frac{\eta_2\, v}{\sigma} \tag{2.16}$$

$$\mathrm{Bo} = \frac{\mathbf{F}_g\,(\text{gravity forces})}{\mathbf{F}_c\,(\text{capillary forces})} = \frac{\rho\, g\, r^2}{\sigma} \tag{2.17}$$

$$\mathrm{M} = \frac{\eta_2}{\eta_1}\ , \tag{2.18}$$

Friedman (1999) evaluated the magnitude of the various forces in soils for a representative case of a water-air interface moving. Inserting the values, when water is displacing air from a representative pore of radius 10 μm at a high velocity of 0.1 cm s^{-1} (using the rounded values of $g = 10^3\,\mathrm{cm\,s^{-2}}$, $\rho = 1\,\mathrm{g\,cm^{-3}}$, σ=10^2 dyne[a] $\mathrm{cm^{-1}}$ and $\eta = 10^{-2}\,\mathrm{g\,cm^{-1}s^{-1}}$), into Eq. 2.16 and 2.17 yield Ca $\approx 10^{-5}$ and Bo $\approx 10^{-5}$. Hence, the interfacial forces are some five orders of magnitude larger than the viscous forces.

2.2.1. Stable and unstable fluid displacement

The stability of an invading front is controlled by the interplay between viscous, gravity and capillary forces that can act as either stabilizing or destabilizing displacement.

Stable displacement occurs when the front between the two fluids is flat, or when the front width (distance between the most and least advanced portion

[a]dyne is the unit of force in the cgs system and equals 10^{-5} N.

of the front) is constant with time. Stable displacement takes place if viscosity forces are dominated, and capillary effects and pressure drop in the displaced fluid are negligible ($M < 1$ and $Bo > 1$). Here a flat front develops with only a few irregularities of a few pores. Now, the question is that what conditions give rise to transitions from flat to unstable displacement fronts within a porous media?

Unstable displacement can arise as a result of fluid instabilities created by density or viscosity differences between the two immiscible fluids. Destabilizing influences such as large viscosity ratio, action of gravity, or rapid drainage velocities can cause the front width to grow without bound, resulting in instability and onset of fingering. Phase instability displacement or "fingering" separate from the single phase concept of flow channelization, occurs where any of capillary, gravitational and viscous forces are dominated. For unstable displacement, three major flow regimes have been identified: viscous fingering, capillary fingering and gravity-driven instability. The properties of the different regimes are briefly discussed below.

- **Viscous fingering** occurs when a less viscous fluid displaces a more viscous one; a planar boundary between the fluids is unstable against small perturbations, and in the course of time the interface adopts a fingered configuration. The process is obtained by injecting a low viscosity fluid into a medium of high viscosity fluid with a high injection rate. The instability arises from a pressure gradient advancing the less viscous fluid against the more viscous one. The action of such driving-force mechanisms leads to the viscous fingering patterns. Viscous fingering results when viscous forces are significant relative to capillary forces ($Ca \gg 1$).

- **Capillary fingering** is executed by injecting the invading fluid at very low injection rate. The low injection rate causes the viscous forces to vanish and capillary forces dominate the viscosity ($Ca \ll 1$ and $Bo \ll 1$) and local variations in pore throat size govern the flow path. In this case, the non-wetting phase advancing on several pore throats will invade the largest pore first where the critical pressure is lowest. Once that pore has been drained, a new set of pore throats presents itself to the invading front, and the process repeats. Consequently, the principal force is due to capillary forces of the interface between the displacing and the displaced phases.

- **Gravity-driven instability** occurs when a denser fluid displaces a lighter one from above with the principal forces due to gravity, and viscous forces do not act to fully stabilize the displacement front. With Bo $\gg 1$, the instability arises by gravity acts on the fluid phase and serves as a stabilizing force by flattening the interface and eliminating height differences caused by viscous instability or capillary fluctuations. In this case, gravity fingers propagate vertically in the medium and continue to grow rapidly because of the gravitational instability of the process. Thus, fingering due to gravity may take place when water infiltrates into unsaturated porous media.

In the present study, we used experiments to explore the formation of gravity-driven fingers during the infiltration of water into non-horizontal and initially dry porous sand column by influence of gravity and capillarity.

In a recent study, Méheust *et al.* (2002) used 2D glass bead packs to study drainage morphology for a range of Ca and Bo values. They defined a generalized bond number $\mathrm{Bo}^* = \mathrm{Bo} - \mathrm{Ca}$ and showed that experimental drainage front morphology was a function of Bo^*. For $\mathrm{Bo}^* > 0$, indicating Bo > Ca, the predominance of gravitational forces resulted in stable displacement (flattened fronts). For $\mathrm{Bo}^* < 0$ or Ca > Bo, the diminishing stabilizing force produced fronts that became progressively more unstable, indicated by increasing front width as Bo^* became more negative. At slightly negative Bo^* values (in the range of $0 < \mathrm{Bo}^* < -0.05$), capillary forces became significant resulting in behavior characteristic of capillary fingering. As Bo^* decreased further, viscous forces became significant and viscous fingering was observed for values of $\mathrm{Bo}^* < -0.08$ (approximate range).

2.3. Visualization of Flow and Transport in Porous Media

The spatial and temporal variability of water and solute fluxes in soil makes it difficult to obtain a quantitative understanding of the dynamics of water and solute inside the sample without destroying it. During the last half century , soil science methods to study the hydraulic behavior within a sample of porous media without destruction of the sample became more attractive. This section reflects the state of art of non-destructive measurements for visualization and imaging as a means for quantitative analysis of flow and transport phenomena in porous media. The analysis of the sequential dynamic events in two and

three-dimensional space involving one or more temporal variables in single or multiphase systems is improving by outstanding progress in computer science, technology and image processing. Attention is focused on visualization and imaging of dynamic transport phenomena in animate and inanimate systems (Sideman 2002). Of particular interest is the interplay between reality and imaging as well as the application of the quantitative information contained within the visual images of real systems. Visualization is the art of transforming normally invisible phenomena into visible measurable events. Flow dynamic visualization is still attracting the scientific world, probably since it can be tackled both experimentally and theoretically. The need for better methods to image transient flows in porous media has been discussed by a number of authors (Darnault 2001, DiCarlo *et al.* 1997).

At present, very few methods exist for rapid, non-destructive and accurate measurements of fluid contents in three-phase, sand or Non-Aqueous Phase Liquid (NAPL)-air-water systems in transient flow fields. These methods are time consuming and can be used only near steady state flow conditions. These non-invasive imaging techniques that have the potential to provide the required information on the internal structure and/or moisture distribution in soils are:

- **Neutron Computed Tomography (NCT)** is a real-time, non-invasive imaging method that can be used for quantitative imaging of hydrologic phenomena at video frame rates, with great sensitivity to variations in moisture content, sub-millimeter resolution and image fields greater than a few hundred square centimeters. This imaging technique can provide two-dimensional images in transmission. The measurements of moisture content within a flow field can be obtained by measuring the intensity change of a thermal neutron beam as it passed through the experiment chamber and interacts with the nuclei of atoms (Deinert *et al.* 2004, Menon *et al.* 2006).

- **X-ray Computed Tomography (XCT)** or synchrotron X-rays absorption (film-based radiography) imaging technique allows accurate and fast measurements of fluid contents in transient flow fields, in any soil type. However, they are limited to measurements of a few square millimeters of the flow field at one time (Liu *et al.* 1993, McBride and Miller 1994, DiCarlo *et al.* 1997, Bayer *et al.* 2004). The technique is based on the attenuation of an X-ray beam by a substance. The attenuation pattern of the beam is recorded as two-dimensional image in transmission, such

as in traditional medical X-ray imaging. This technique is also used to perform three-dimensional tomography images.

- **Magnetic Resonance Imaging (MRI)** has also found a well established tool applied in studying fluids in porous media. It also provide information on water distribution and also on other pore scale characteristics such as the specific surface, diffusion coefficient, or motion velocity. In this process, the volumetric water content at one voxel is directly proportional to the number of resonating spinning or magnetic properties of the water protons in the voxel. This magnetization at each voxel of matrix material is measured with nuclear magnetic resonance. This technique can also provide two and three-dimensional images to obtain information on soil properties and flow at high spatial resolution. Using this method, a quantitative measurement is not always possible, especially at low saturation levels (Johns and Gladden 1998, Deurer *et al.* 2002, Votrubovà *et al.* 2003).

- **Gamma-ray Computed Tomography (GCT)** can also be used as a tool to investigate and evaluate possible modifications in soil structure and to analyze the variations of soil physical properties such as soil density, porosity, pore size distribution and bulk density within the soil sample volume. This gamma radiation technique uses a radioactive gamma ray source, e.g. ^{241}Am (Ferrand *et al.* 1986, Oostrom *et al.* 1995, Pires *et al.* 2005).

Disadvantages of these methods are that they cannot measure transient flow phenomena with high temporal resolution and that their use involve radiation hazard.

- **Light Transmission Method (LTM)** is the only method that does not use radiation and is the best available method for rapid and accurate measurements of transient flow in porous media on a sub-second time scale. It has been applied since 50 years in Hele-Shaw cells with smooth walls (Saffman and Taylor 1958, Chouke *et al.* 1959). The LTM is a non-destructive method that allows visualization and measurement of fluid content in transient water flow occurring in sandy porous media. The advantages of the LTM are that it does not involve radiation and that it is able to visualize fluid content changes over the whole flow field with a time resolution of tenths of second (Tidwell and Glass 1994, Darnault 2001, Mortensen *et al.* 2001). This method is useful for transparent and

thin slices of porous materials, e.g. coarse sand and crushed glass. The LTM uses the hue or intensity of light transmitted through a slab chamber to measure fluid content, since total liquid content is a function of hue or light intensity. The LTM captures the spatial resolution of the fluid contents and can provide new insights into rapidly changing, two-phase and three-phase flow systems. Application of the LTM as a visualization technique for environmental and physical phenomena, groundwater remediation by surfactants as well as visualization of model cluster growth and fractal dimensions is noted by Darnault *et al.* (2002). Stöhr (2003) used the LTM methods to study flow and transport in porous media particularly solids, liquids and fluorescent dyes and applied this optical method for the highly precise matching of refractive indices using planar laser-induced fluorescence with high temporal and spatial resolution.

Therefore, there is a method, LTM, that allows full field moisture content visualization in two-phase systems with high spatial and temporal resolution. In this research we adapt the LTM to measure the dynamics of water saturation in a sand-air-water system.

2.4. Preferential Flow Phenomena

Two different types of immiscible flow are found in porous media: (1) transient displacement classified as either drainage or imbibition, and (2) steady state flow (Dullien 1992). During transient displacement complex patterns can be found where preferential flow paths develop. From a phenomenological perspective, preferential flow refers to nonuniform and rapid movement of water and solutes into narrow channels of some subregions of the soil. There, water is gated by less permeable layers and funneled through more permeable regions. For inclined and cross-bedded layers this may lead to a strong focusing of the flow to narrow channels (Stagnitti *et al.* 1994, Roth 2006). The soil profile can be distinguished in a distribution layer near the soil surface and a conveyance (preferential) zone below it (Steenhuis *et al.* 1994, Ritsema and Dekker 1995). The distribution zone acts as a linear reservoir resulting in an exponential loss of solutes from this zone and it funnels water and solutes in flow paths within the conveyance zone. By Lawes *et al.* (1882) observations, in the conveyance zone the transport of water and solute collected in drains can be separated into two constituents: preferential flow (direct drainage) and matrix flow (general drainage). As shown schematically in Figure. 2.4, rainfall enters a mixing zone where it mixes with the water and solutes in this layer. Water and solutes from

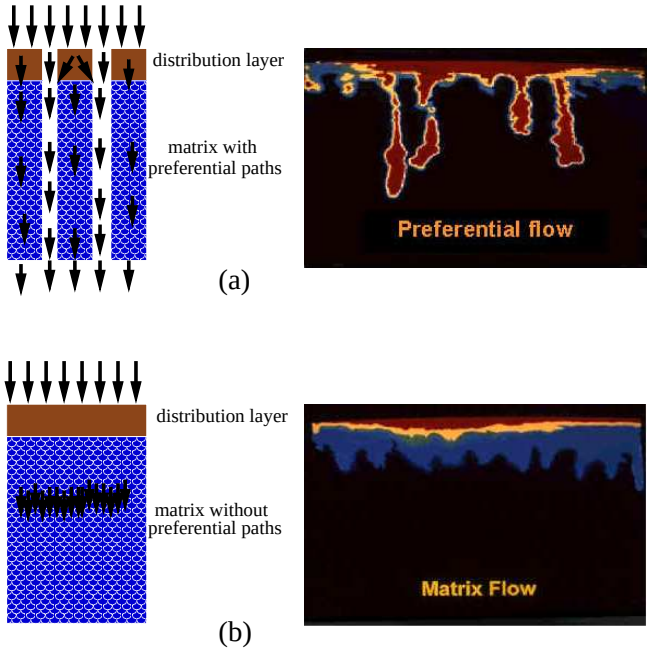

Figure 2.4.: Schematic diagram of flow processes in the mixing layer: wetting front advances in matrix with preferential flow paths (a) and matrix without preferential flow paths (b). The arrows represent the infiltration flux. (Redrawn after Cornell-Website)

the mixing layer are transported downwards as matrix or preferential flow and the latter passes with little modification through the soil channels to the deeper soil or groundwater (Steenhuis *et al.* 1994).

Preferential flow, the rapid non-equilibrium transport of soil solution is more often the rule than the exception. Due to its rapid movement, preferential flow allows much faster contaminant transport. This can provide significant consequences for groundwater quality and has direct impacts on drinking water and human health, animal waste management, nutrient and pesticide management, as well as watershed management.

Matrix flow is a relatively slow and even movement of water and solutes through the soil while sampling all pore spaces, obeying the convective-dispersion theory which assumes that water follows an average flow path through soil.

The chemical composition of preferential flow regions reflects the concentration of water near the surface, while matrix flow represents the concentration

of water around the drain. Thus, when a salt is equally distributed throughout the soil, the salt content of matrix flow is higher than that of the water in preferential flow paths, which is characterized by the rainfall composition. The opposite is true (preferential flow has a higher solute content than the matrix flow), when a fertilizer or tracer were recently applied surface. Consequently, the solute concentration of drainage water depends on the ratio of water in preferential and matrix flow paths (Steenhuis *et al.* 1994; 2001).

The relative importance of the two forms of percolation, preferential and matrix flow depends on the soil type and rainfall intensity. For example, well-structured soils consisting of clay and loam mixes typically experience low permeability rates. In such soils, less than 1% of the pore-volume consists of cracks and subsurface channels. However, during rain events, water infiltrating from the soil surface, often flows through these channels in reference to the surrounding soil-matrix, whose small pores are penetrated comparatively slowly. Even through these channels make up a relatively small percentage of the total pore volume, they may be responsible for the distribution of moisture and solute transport after an infiltration event. Preferential flow may be initiated well below soil-water saturation.

2.4.1. The history of preferential flow and why it is important

Natural soils are mostly non-uniform and often strongly heterogenous. Soil properties are strongly dependent on structure, which determines not only workability and water retention, but also strongly influences soil/plant interaction like root growth, transport of water, air and chemicals and thus can be considered as important parameter for soil quality. Furthermore, soil structure is a main factor determining preferential water and chemical fluxes in soils. The term preferential flow refers to several phenomena which have in common the non-uniform and often rapid movement of water through soils which does not tend to move as a horizontal wetting front. This rapid movement bypasses the bulk of the soil matrix, reducing the potential for pollutant adsorption and/or degradation and increasing the threat of groundwater and surface water contamination.

The concept of bypass flow through macropores and preferred routes and the fact that they will permit rapid movement of water and chemicals dates back to Schumacher (1864) who stated that, the permeability of a soil during infiltration is mainly controlled by big pores, in which water is not held under the influence of capillary forces. Intense studies in the last few decades have also indicated that the preferential flow mechanism is the most significant flow

process influencing the pollution potential and transport of a given chemical in the porous media. Scientists and engineers have devised measurement and modeling strategies in order to characterize and quantify the role of preferential flow processes in water and pollutant transport.

Preferential flow was investigated by Lawes *et al.* (1882) in field drainage experiments. They found that a large portion of water applied to a soil only slightly interacted with that already present in the root zone. As scientists were forced to explain groundwater contamination problems, identified during the mid 20th century, the long-neglected observation of preferential flow phenomena was eventually brought up again. Various pesticides, which were believed to be quickly degraded or strongly sorbed near to where they were applied, were unexpectedly found in the groundwater much more quickly and in higher concentrations than experts would have predicted.

During the last two decades, high concentrations of pesticides in tile lines or shallow groundwater were found in many studies shortly after application. Contamination of groundwater by agricultural chemicals is becoming a serious threat. Modern agriculture is based on a broad range of fertilizers and pesticides to assure reliable crop yields. A long-term hazard is involved that the chemicals get into groundwater, they may remain there for hundreds of years. Although integrated pest management may reduce the amount of chemicals needed, a total ban is currently not feasible.

Preferential flow in soil may occur by three possible mechanisms: flow through large and continuous voids, so-called macropore flow, sub-surface layering in textural interfaces (funnel flow) and instabilities that lead to fingered flow or wetting front instability. All of these terms refer to the fact that water tends to flow only through a portion (sometimes a very small portion) of the total soil volume. Bowman *et al.* (1994) found in one experiment that as much as 80% of the water percolating through the soil profile actually passes through as little as 20% of the cross-sectional area of the profile. The three types of flow are described briefly below, along with the respective soil textures.

2.4.2. Macropore flow

Macropore flow is the result of a variety of soil-forming factors such as flow through non-capillary cracks or channels (Cornell-Website).

Macropores and sub-surface channels can result from either biological activity (e.g., root channels, worm-holes, etc.), geological forces (e.g., subsurface erosion, desiccation and synaeresis cracks and fractures) or agrotechnical prac-

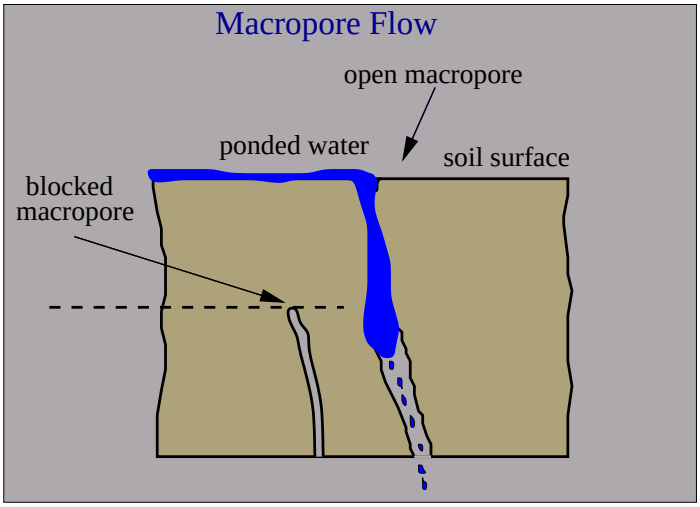

Figure 2.5.: Schematic diagram of water flow through macropores. Water can flow only through those macropores that are open to the soil surface. Blocked macropores remain dry.

tices (e.g., plowing, bores and wells). Surface cracks and channels that lead to a bypass the root zone are also responsible for rapid transport of moisture and chemicals through the unsaturated zone (Beven and Germann 1982, Larsson and Jarvish 1999, Langmaack *et al.* 1999).

Macropores do not begin to conduct water until the soil near the macropore becomes saturated, and there is ponded water on the soil surface that can flow into open or "surface vented" macropores. However, macropores that are blocked by debris or cut off by tillage tend to remain dry and non water-conducting (Fig. 2.5).

These macropores are the result of a variety of soil forming factors such as flow through non-capillary cracks or channels within a profile. In clay and loam soils, for example, areas of relatively low permeability are riddled with channels consisting of cracks partially filled with sand and small stones, as well as passages formed by roots and earthworms as shown in Figure 2.6. When it rains, water infiltrating the ground is more follow these channels than the surrounding matrix, whose small pores are penetrated comparatively slowly. Flow through the uppermost soil horizon (typically the plow layer for current or former agricultural soils) is often fairly uniform. This layer acts as a "distribution layer", distributing the flow to macropores in the subsoil conveyance zone. Water and chemicals that travel in macropores often bypass the bulk of the soil matrix.

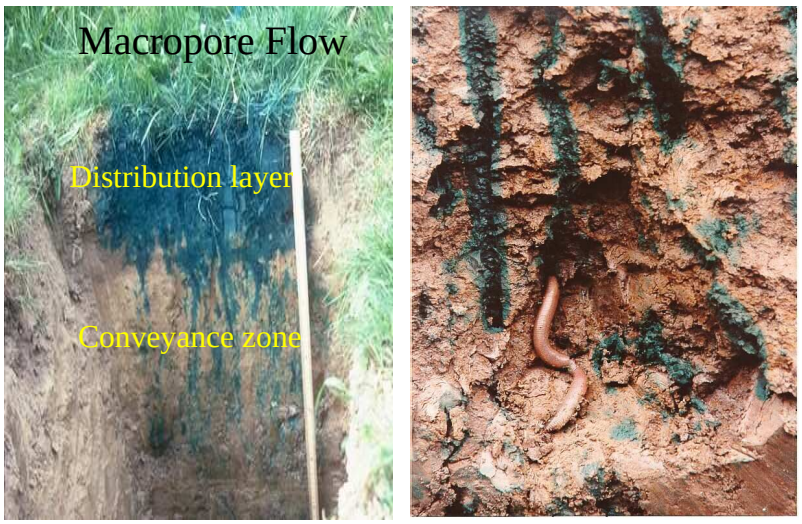

Figure 2.6.: Photographs of macropore flow paths in structured soil dyed by a blue tracer applied at the surface. Below the distribution layer, the dye brached into many fine channels, following structural cracks and continuous earthworm channels, indicating the presence of significant preferential flow paths through macropores. The picture on the right shows an earth worm as pore generator in structured soil (photographs from Cornell-Website).

Flow in macropores and channels can occur with little or no interaction with the surrounding soil-matrix (Pivetz and Steenhuis 1995).

Macropore flow has been identified to be the culprit of contaminations of groundwater with pesticides and other agrochemicals which are typically decomposed or at least retained in the biologically active top soil layers. Corresponding observations in drainage water, the first indirect reports on macropore flow published by Lawes *et al.* (1882). Despite this outstanding study, the understanding of the phenomena remain qualitative and heuristic representations mark the state of the art.

2.4.3. Funnel flow

Funnel flow arises when sloping geological layers cause pore water to flow laterally, accumulating at a low region. If the underlying region is coarser, finger flow may also occur (Cornell-Website).

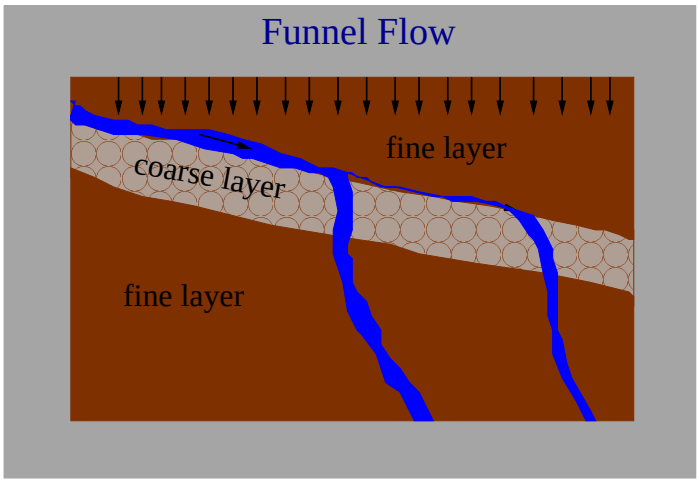

Figure 2.7.: Schematic diagram of the funnel effect in sandy soil. A fast-moving spout forms beneath the lower regions of an inclined layer.

The way soil is layered makes a big difference in how water and solutes find paths down to the groundwater. The way these flow paths merge depends on inhomogeneities in the soil. Sloping structural interfaces have a considerable effect on the degree of merging and rate of flow (Walter *et al.* 2000).

Funneled flow is a unique category of flow phenomena referring to the situation in which a capillary barrier develops above a coarse layer which underlies a relatively fine soil (Walter *et al.* 2000, Kung 1990b). At low flow rates, when the matric potential at the textural interface is so low that water cannot enter into the coarse, underlying soil, the capillary barrier effectively restricts vertical water flux, forcing the water to move laterally along the bedding interface (Fig. 2.7). Since moisture is forced to take this narrow route, the concentration of moisture and solutes may once again bypass much of the soil matrix and be directed to the groundwater.

The diversion of flow caused by layering is significant because even in areas where groundwater monitoring is conducted routinely; pollution may be missed entirely if the detecting is placed in the wrong location. Therefore, in order to prevent groundwater contamination, it is desirable to know where the layers and funnels are.

Sloping interfaces of texturally different layers may act as funnels and concentrate flow. This phenomenon can also be observed in field experiments using dye tracers (Fig. 2.8). Textural interfaces and subsurface layers may

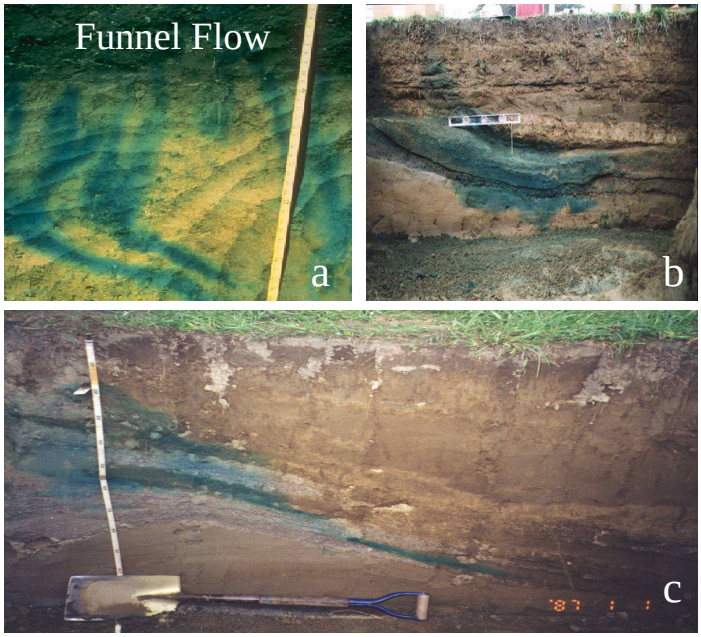

Figure 2.8.: Photographs of funnel flow at field site runs with dye tracers to observe the funnel effect in sandy soil: a) Finger funnel flow with dye penetrating into the fine sand appears to have moved freely and directly into the coarse sand below. b) Textural interfaces and sub-surface layers may cause moisture and solutes to preferentially flow in a prescribed direction. c) Blue dye flowing vertically (unsaturated flow) moves laterally when it encounters a sloping coarse-textured lens (photographs from Cornell-Website).

cause moisture and solutes to preferentially flow in a prescribed direction. The funnel flow phenomenon was coined as an example of preferential flow by Kung (1990a;b).

2.4.4. Fingering flow

Instability in the wetting front leads water to find its way down through a number of channels, so-called fingers (Cornell-Website).

Fingering (flow instability) is one form of preferential flow resulting from instability of infiltration through the unsaturated coarse soil. In general, fingering

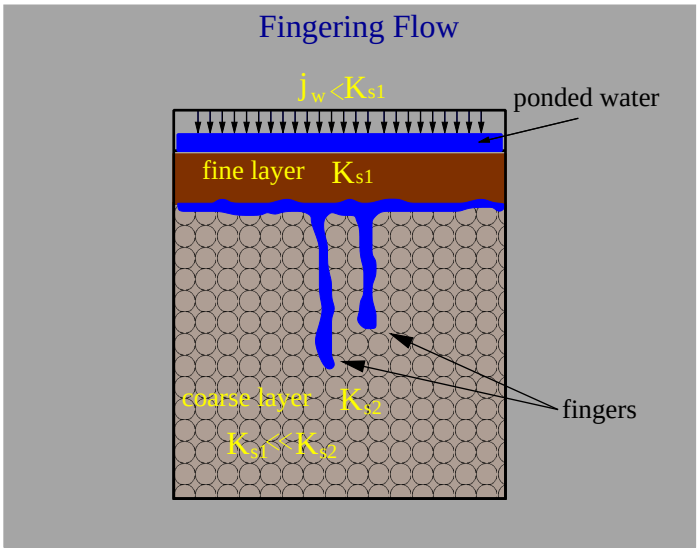

Figure 2.9.: Schematic diagram of fingering flow. Wetting front instability, or gravity driven fingering, can occur during vertical infiltration in homogeneous coarse grained materials when the infiltration rate is below the saturated hydraulic conductivity.

occurs during water infiltration into a dry soil profile with a finer textured soil layer rests on top of a coarse textured layer. The water infiltrates into regions where the saturated hydraulic conductivity increases in the direction of positive flux (Fig. 2.9). When the wetting front in the finer textured medium contacts the boundary with the coarser textured medium there is often insufficient absorbency or capillarity in the coarser medium to pull the water across the boundary and into the coarser soil. Then, fingered flow can emerge as a consequence of the development of an unstable wetting front in the coarse-grained sands, when the infiltration flux is less than the saturated hydraulic conductivity of sand and gravitational influences on the imbibing solution must dominate the forces of capillary.

Unstable flow of water during infiltration was first reported by Hill (1952). In 1972 David Hill and Parlange (Hill and Parlange 1972) documented, for the first time, preferential flow in homogeneous soil at low infiltration rates. Consequently, flow instabilities have been studied extensively, both experimentally (Hill and Parlange 1972, Diment and Watson 1985, Glass *et al.* 1989a;b;c, Baker and Hillel 1990, Liu *et al.* 1993; 1994b, DiCarlo 2004) and theoretically

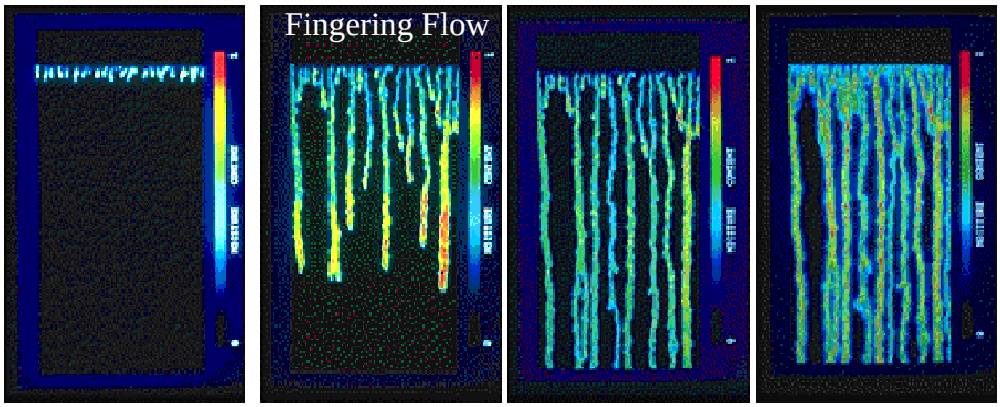

Figure 2.10.: Formation of water fingers in homogeneous sandy soils. These images are produced by passing light through a "sand sandwich" and converting the different intensities to different colors by a computer program. Black color represents regions of low moisture content and red soil-water saturation. The range of colors between black and red represent degree of moisture saturation (photographs from Cornell-Website).

(Eliassi and Glass 2001; 2002; 2003, Egorov *et al.* 2003, Jury *et al.* 2003).

The fingering phenomenon occurs in homogeneous sand. It has been demonstrated by Steenhuis and Parlange (1991) that layered soils are not necessarily required to trigger fingering events, and that fingering can emerge in a relatively homogeneous sand at rainfall rates substantially below the saturated hydraulic conductivity. The main experimental apparatus to monitor fingering flow is the Hele-Shaw cells. It consists of a one-centimeter-thick layer of sand between two glass plates and a light-intensity method. When water is applied in excess at the top of the cell, it will enter and create flow fingers at a rate depending on the water content in the cell and on the physical properties of the sand used, like for example the permeability. Most of the water flows only through a small portion of the cell. In a homogeneous sand profile, the fingers are quite vertical, in contrast they deviate from their vertical paths as the sand becomes more heterogeneous (Fig. 2.10).

Unstable finger flow forms during redistribution following the cessation of ponded infiltration in porous sand and concrete surfaces under both dry and wet initial conditions. Fingers form and propagate rapidly when the porous media are initially dry, but form more slowly and are wider when the media

(a) (b)

Figure 2.11.: Three-dimensional form of fingering flow: a) Frozen fingers of blue-dyed water, exposed by removing dry sand (photograph from Cornell-Website). b) 3-D illustration of a finger formed during redistribution in a 10 cm diameter column with transparent walls. The column was frozen at the end of the experiment to preserve the shape of the finger. The picture was taken after the column was removed from the freezer and the loose soil that had no water in it fell out (photograph from Wang *et al.* (2003)).

are wet (Wang *et al.* 2003, Jury *et al.* 2003).

Some other experiments make use of a chamber that allows observation in three dimensions. Since the light-intensity method cannot be employed in this situation, flow paths are marked by water containing a blue dye. After the water has had a chance to penetrate the soil, the sample is frozen, and when the loose dry sand has fallen out, the congealed flow paths can be examined (Fig. 2.11).

Fingering is an important mechanism causing agricultural herbicides and fertilizers to move rapidly from the soil surface, through the crop root zone and into the groundwater. Flow in these paths is still under extensive study because of its random and its instability in wetting fronts. Classical convective-diffusion models, however, have proven inadequate for the analysis of preferential and multiphase flows in porous media (Glass *et al.* 1991). The effects of these flow types are often cited as reasons for predictive error in multi-component flow

models, such as those used by the oil industry and in predictions for the recovery of pollutants in soils and aquifers. A better understanding of preferential flow will in turn improve the predictions of oil field behavior, the development of better remediation models and the design of pollutant recovery equipment. While considerable effort has been made on the analysis of fingered flow in two-dimensional air-water systems, and on the infiltration of water fingers into oil saturated media, little advances have been achieved in the field of displacement of water by oil or the analysis of fingered flows in three-dimensional systems in real-time (Deinert *et al.* 2002).

The fingering phenomenon will be described extensively in chapter 5 and will focus on the mechanism of finger developing in uniform and non-uniform initial moisture content in a Hele-Shaw cell filled with sand.

3. Experimental Methods and Materials

Fundamental studies on multiphase flow and transport processes of fingering phenomena within porous media require experimental techniques as light transmission system to measure state-variable at high spatial and temporal resolutions. This chapter resumes the development and application of the Light Transmission Method (LTM) for three phase flow systems as method for investigating unstable fingered flow in a sand-air-water system. This technique involves placing a vertical two-dimensional experimental Hele-Shaw cell in front of a uniform and stable light source. The transmitted light is recorded similar to the experiments done by Hoa (1981) and Glass *et al.* (1989c). These experiments were performed in the laboratory. In the present study, methodology is extremely important, because unstable phenomena are very sensitive to initial and boundary conditions. Hence, an experimental approach was developed and improved using a transparent porous Hele-Shaw cell and the visible light transmission method to explore gravity-driven instability with high resolution.

In this chapter, the experimental setup together with the methodology are presented in detail. Additionally, an improved method to measure the phase saturation with high spatial and temporal resolution is described. In the following section 3.1, the experimental setup, material and measurement procedure are presented. Section 3.2 is about the methods with a brief overview of LTM and X-ray absorption techniques used in this project for visualization and imaging of the flow transport phenomena in Hele-Shaw cells. Within this section, we describe an introduction of the physicals process arisen by light propagation through porous media in an optical system used in this experiment. Section 3.3 focuses on the calibration of the measured transmitted light and the water saturation measured in X-ray absorption.

3.1. Laboratory Materials and Setup

3.1.1. Materials and preparation of samples

The basic materials used were fine and coarse sand. The sands were sediments and originally come from the river Rhein. The coarse sand consists of a small amount of the fine sand. It was sieved to remove fine particles in order to obtain homogeneous coarse-grained granular sand with a rather uniform grain-size distribution.

The grain sizes and saturated hydraulic conductivity of three types of sand used are listed in Table 3.1.

Material	$K_s \pm$ STD[a] [cm h^{-1}]	Grain size [µm]
Fine sand	12.0±0.7	63-250
Coarse sand	265±8	250-1250
Sieved coarse sand	873±24	630-1250

[a]standard deviation

Table 3.1.: Grain sizes and saturated hydraulic conductivity of sands used in experiments.

3.1.2. Saturated hydraulic conductivity

In a separate experiment the saturated hydraulic conductivity (K_s) of these three types of sand was measured independently using the falling head method (as introduced by Klute and Dirksen (1986)) applying a light transmission system (section 3.2.1). The porous medium were filled in a small Hele-Shaw cell ($30 \times 30 \times 0.3$ cm) to a depth of L. Then the sample was ponded with water which was allowed to drain freely due to gravity. During free drainage the water level $h(t)$ in the cell was monitored by taking sequential images with a good time resolution. Brilliant blue solution was used as a tracer with very low concentration for better visualize the water level. It was observed that when $h(t) > L$, the height of the water level $h(t)$ decreases exponentially with time until it reaches the surface of the sample. With this information the saturated hydraulic conductivity can be calculated using:

$$h(t) = h_0 e^{\frac{-K_s t}{L}} \quad , \tag{3.1}$$

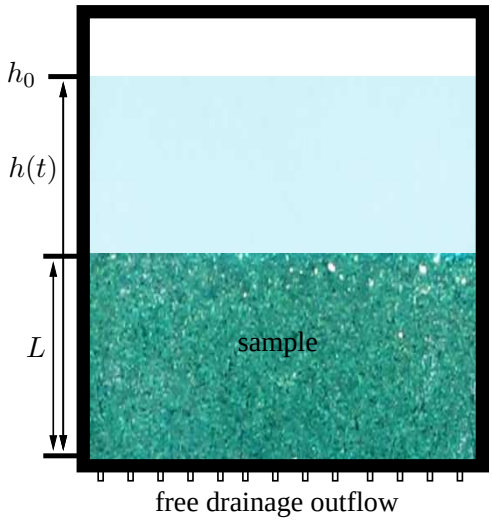

Figure 3.1.: Sketch of falling head method used for determination of saturated hydraulic conductivity.

where t is the duration of drainage, h_0 is the initial height of the water level inside the cell at the time $t = 0$ and L is height of the sample as shown in Figure 3.1.

Then the saturated hydraulic conductivity can be determined from plotting $\log(h(t)/h_0)$ versus time, i.e.,

$$K_\mathrm{s} = -\frac{L}{t} \log\left(\frac{h(t)}{h_0}\right) \ . \tag{3.2}$$

By this method, we obtain the saturated hydraulic conductivity of the fine, coarse (heterogeneous structure) and sieved coarse (homogeneous structure) sand as 12.0±0.7, 265±8 and 873±24 cm h^{-1}, respectively. The measured values are listed in table 3.1.

3.1.3. Hele-Shaw cell

An attractive approach to get a high spatial and temporal resolution of phase saturation is a Hele-Shaw cell. In this research, infiltration experiment was conducted in a 2D Hele-Shaw cell ($160 \times 60 \times 0.3$ cm) which was made of two parallel glass plates (8 mm thick, attached to an aluminum frame) with a small distance apart (0.3 cm) and the porous material was placed inbetween. The

thickness of the cell, i.e. the separation of the glass plates, was small enough to transmit visible light while the lengths of the other two dimensions were only limited by mechanical stability.

In different types of experiments the cell was filled with different layers of dry sand: (1) 5-10 cm fine-textured sand as a distribution layer on top characterized by a relatively low saturated hydraulic conductivity and with grain-size diameter 63-250 µm, (2) the structured layer, with grain-size distribution in the range from 250 to 1250 µm and (3) the coarse-grained granular homogeneous layer, the same material for structured layer but previously sieved for grains larger than 630 µm such as coarse-textured sand characterized with a high saturated hydraulic conductivity. The coarse homogeneous layers were filled into the cell through the top using a funnel-randomizer in order to minimize segregation and make the most possible homogeneous and uniform distribution. The textural interface between different layers was made as flat as possible specially between the fine and the coarse homogeneous layers. In contrast to sands used, the structured layer was more heterogeneous with thin-grained filaments separating coarse-grained regions. The structured layer was filled in a way that grains of different size were allowed to separate during the filling procedure to produce a heterogeneous structure of different textures. This is a consequence of inevitable sorting that results from pouring of granular media with a wide grain-size distribution.

At the top of the cell, water infiltration was applied through 6 hypodermic dripper tubes (3 mm diameter) located near the top sand surface at fixed positions. The flux was adjusted by a pump which sucks water from a reservoir placed on a balance. The weight of water mass was frequently recoded with computer which calculates the flux. The lower end of the cell was closed. A single outlet, the black dot at the lower left corner (Fig. 3.2), allows water and air to escape freely. The vertical boundaries were closed for water flow. Under certain conditions the less conductive fine top layer may constrain the supply of water to the more conductive coarse sublayer.

3.1.4. Light source

The cell was placed in front of a homogeneous illumination, from a bank of high-output fluorescent light with four fluorescent lamps (OSRAM-55W-White). These lamps were installed into a light box, a wooden box of dimensions $165 \times 32 \times 30$ cm, where the cell containing the sand was mounted on it. The light system provides a low-temperature and stable source for lighting the sand pack from the back side. A homogeneous illumination of the entire

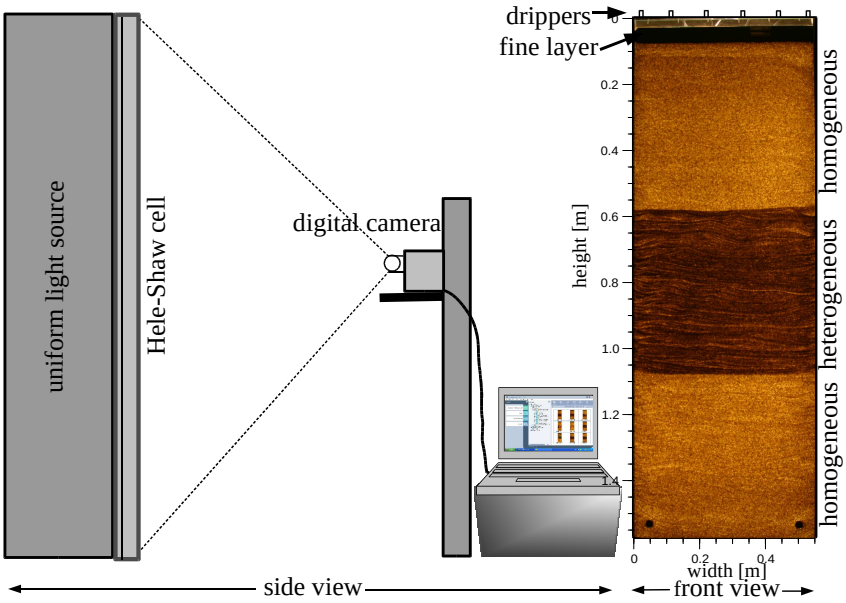

Figure 3.2.: Sketch of the experimental setup (side and front view). A transparent Hele-Shaw cell with four layers of sand was placed in front of a uniform light source. Transmitted light was recorded by a digital camera.

surface of the Hele-Shaw cell was achieved by using a diffusion foil between the lamps and the cell. Variations in the light source intensity occur each time the system is switched on or off. A reasonably constant light source intensity level is also required. In our system, the possible temporal variations in the light intensity was calibrated out during the experiment through a region that remains dry during the infiltrating. This adjustment was required for the light technique to correct for variations in the light source stability (more details in section 4.1).

A schematic representation of the front and side view of the light imaging system used in experimental setup is shown in Figure 3.2.

3.1.5. Camera setting

To monitor the fingered flow and infiltration, images were captured and recorded at predetermined intervals immediately after water application using a Canon

digital camera (Canon EOS 300D, 6 MPixel) with a 18-55 mm equivalent lens. The camera was located approximately 1.5 m in front of the cell and focused on the front of the experimental cell with array size of 691×1929 pixels image with a pixel size of 55 cm×157 cm covering the entire cell. The spatial resolution of the acquired image is defined by the array size of the camera and the size of the test medium which gives 0.6 mm^2 per pixel. The profiles were photographed without any optical filters. Both the camera and the cell were carefully aligned horizontally and fixed. The images were stored in a computer simultaneously. A setup of USB board (hardware) was used to capture the frame by using "ZoomBrowser"(software by Canon). The temporal resolution was 15 seconds when the fingers were quickly traveling downward including an exposure time 2 seconds (aperture F8) and storage of images. All images were taken under identical conditions with manual setting.

3.1.6. Tensiometer construction

The experimental aspect of this study requires rapid point measurements of phase pressure during the passage of fingers. The monitoring of internal dynamics of water pressure change was not possible with optical methods, hence we employed the traditional instruments e.g. pressure sensors installed into access ports. Many mini-tensiometers were installed at different locations in the designated holes over the back wall of the cell according to Selker *et al.* (1992a).

With this method the speed of the spreading pressure front and the actual matric potential, as the difference between water pressure and atmospheric air pressure outside the cell at a specific position, could be measured. The special mini-tensiometer designed for these measurements is sketched in Figure 3.3. This instrument consists of a cylindrical porous ceramic plate (P80), height 4 mm and diameter 8 mm, with a high air entry value less than 10 m. The tip of ceramic plate had to be as flat as the surface of the sample on which it was placed, for maximum contact. The tensiometers were flush with the inside surface of the cell and fixed with a mounting boss. The transducer used to measure the pressure was from the Honeywell 26PC series (www.honeywell.com), which features a sensing technology that utilizes a specialized piezoresistive micro-machined sensing element. The transducer port was threaded and fastened directly to the tensiometer body, which yields the minimal hydraulic path connection.

After installing the tensiometers, water was poured into the plastic tube without entrapping air bubbles in the tube because this air could lead to a loss

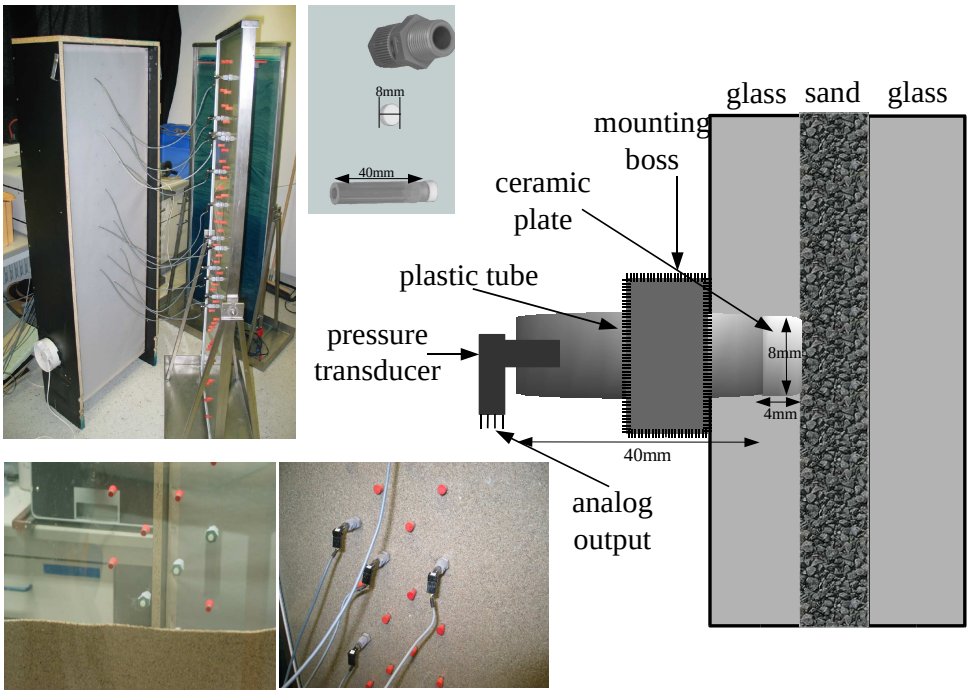

Figure 3.3.: Sketch and Photo of the tensiometer installed over the cell and a Sketched cross section of a mounted tensiometer. The porous ceramic plate (light gray) connects directly to the pressure transducer via a firm plastic tube so that the ceramic plate was in contact with the sand. It was necessary to avoid gaps between the glass and the tube for install the tensiometer in the cell.

of hydraulic contact between the transducer and the sand. The response time of tensiometers was less than 1 ms.

The calibration of tensiometers was carried out by using sequence defined heights of water in a calibration tube. The different pressure values corresponding to different heights were evaluated by a computer. This yields the calibration parameters for each sensor.

3.1.7. Experimental setting

The experimental procedure consists of several steps such as sand preparation, cell cleaning, filling and packing of the cell with sand, injection of water into the

cell and recording light intensity and water pressure. Infiltration experiments were carried out with an initially dry sand in the Hele-Shaw cell under varied conditions for different flow rates. A set of many experiments was attempted with constant and different flow rates.

After reaching stationary water flow to visualize the velocity field inside the cell, additional infiltration experiments were performed by using a dye tracer ($0.5\,\mathrm{g\ l^{-1}}$ Brilliant Blue) which was applied to the almost stationary flow field behind the water infiltration front. All experiments started with water application on dry sand and after the fingered flow field was fully developed and steady state was reached, the irrigation depending on the type of experiment was stopped and dye was infiltrated.

3.2. Methods

In this study, we used the Light Transmission Method (LTM) to measure the vertical redistribution and the dynamics of water content in the Hele-Shaw cell according to Glass *et al.* (1989c), Tidwell and Glass (1994). The light intensity was directly related to water content. Application of the LTM as a visualization technique involves placing a two-dimensional experimental chamber in front of a uniform light source and recording the transmitted light. This technique requires that the image system is transparent to translucent and is based on the fact that the intensity of transmitted light can be used as a proxy for water content.

This thesis describes a moisture content visualization technique which is based on the physical observation of the light transmission through sand. The technique is developed to use in thin but extensive experimental systems. In order to calibrate the light imaging system, we used X-ray absorption technique. In both the X-ray and light technique, electromagnetic energy is passed through the test media and the water saturation distribution integrated over the media's thickness is measured as variations in the transmitted X-ray or light intensity field. The difference between the techniques lies in the frequency of the radiation used and in the physics governing the interaction that gives rise to variations in the transmitted intensity field. When using low energy X-rays, variations in the transmitted intensity field arise from the sensitivity of X-ray absorption (photoelectric absorption) to the density of the media, which is directly related to liquid saturation (i.e., increase in saturation yields a decrease in X-ray transmission). For the light technique an increase in saturation results an increase in light transmission because of the closer matching of the index of

refraction of the matrix and water relative to the matrix and air.

A brief overview of the light transmission and X-ray absorption technique is presented further below.

3.2.1. Light Transmission Method (LTM)

The color can be expressed in different formats and quantification of color difference can be complicated. The color for video cameras, color monitors and computer graphics is defined in terms of a vector with the intensities of the three components of Red, Green and Blue (RGB). Another system to specify the color vector is Hue, Saturation and Intensity (HSI). Hue is the attribute that describes the pure color and is what we are typically referring to when we use the term color. Saturation is the attribute that describes the degree to which the color is diluted with white. Intensity is the attribute which corresponds to the gray level (black and white) of the color image (Darnault *et al.* 1998). The HSI color model owes its usefulness to two principal facts. First, the intensity component, I, is decoupled from the color information in the image and second, the hue and saturation components are intimately related to the way in which human beings perceive color. The advantage of the HSI space is that it treats color roughly the same way that human perceive and interpret color.

Using RGB format was not sufficient to give a unique relationship with water content. The difficulty in using RGB is the interdependence of color saturation with values of the components of the color vector. Thus, even if the eye can see a difference in color, RGB is unable to pick out the colors in a simple predictable manner (Wilson 1988).

These features make the HSI model, an ideal tool for developing image processing algorithms, based on some of the color sensing properties of the human visual system (Gonzales and Woods 1993). Therefore, if the human eye is able to see, these differences can be quantified using the HSI space.

The HSI model can be defined by a transformation of RGB color component as (Gonzales and Woods 1993):

$$\begin{aligned} H &= \cos^{-1}\left\{ \frac{\frac{1}{2}\Big[(R-G)+(R-B)\Big]}{\Big[(R-G)^2+(R-B)(G-B)\Big]^{\frac{1}{2}}} \right\} , \\ S &= 1-\frac{3}{(R+G+B)}\Big[\min(R,G,B)\Big] , \\ I &= \frac{1}{3}(R+G+B) , \end{aligned} \tag{3.3}$$

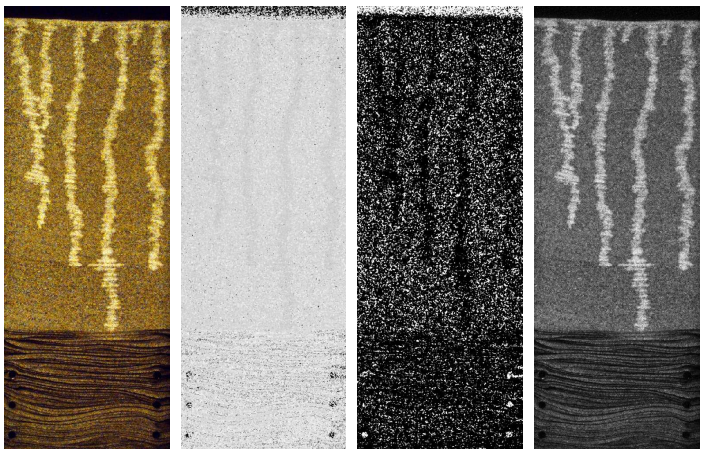

Figure 3.4.: Visualization of flow fingering experiment through initially dry porous Hele-Shaw cell using RGB, Hue, Saturation and Intensity formats calculated according to Eq. 3.3. The intensity image shows the direct relation with highly localized flow paths that originate from the flow instability in uniform media.

where H, S, and I are the hue, saturation and intensity of the output HSI image; and R, G, and B are the red, green, and blue components of the RGB image.

Image processing was done using the $C/C++$ library Quantim written by Vogel (2006). A complete description of processing on images is presented in chapter 4. In image processing recorded images were converted from RGB to HSI format. Figure 3.4 shows RGB and HSI spaces of a sample experiment image. In a dry porous medium the moisture content is immediately visible to the eye from the other side. The recorded color differences are visible between the different formats. In each format, (RGB and HSI), the color is not completely uniform and slight spatial differences exist due to sand and water ganglia formation (Fig. 3.4). The color attributes of pixels in HSI space are compared with water content in RGB space. This comparison exhibits a better direct relation between intensity and water flow fingers.

The moisture visualization technique is based on the principle that the transmitted light intensity measured in a RGB image (Eq. 3.3) increases with an increase in moisture content (i.e. saturation). At any given location in the medium through which light is transmitted, we found that the brighter loca-

tion represents the higher porosity and/or moisture content (Fig. 3.4). This technique also allows a rapid assessment of the homogeneity in the porous cell before the onset of infiltration.

Visible light transmission was first used quantitatively by Hoa *et al.* (1977), Hoa (1981) to measure the saturation within a thin, sand-filled slab chamber using a small movable light transmission sensor. Hoa's method was expanded by Glass *et al.* (1989c) and Bell *et al.* (1991) to visualize moisture content in an entire two-dimensional flow field by supplying a diffuse light source. This method has been successfully used for the study of rapid variations of the water content distribution in thin samples of porous media. We applied directly this development using the relationship between intensity of transmitted light through a Hele-Shaw cell and water content within the context of this study.

Here, before describing the next method (X-ray absorption) that we used for calibration of the measured light intensity in order to get the water saturation, we present a brief overview of the the physical process arisen by light propagation through porous media in an optical system used in this experiment.

Light Propagation through Porous Media: During the propagation of light through a transparent porous medium with densely packed particles, light is deviated from its course. According to the physical nature of light and its behavior at interfaces of different media, the deviation is dependent on the angle of incidence, the wavelength of the light beam and the refractive indices of that medium. In three phase system used in this study (air-water, sand-air, sand-water), for example, light that passes through these phases and media encounters sand, air and water phases. In each of these phases, light is absorbed exponentially. In addition, it can be scattered, reflected, and refracted at the interfaces between the different phases. Through these deviations of light, the scattering usually referred to as a random disturbance of light induced by passage through regions of different refractive indices. As the light is scattered, it becomes anisotropic, and hence, the direction in which it leaves the material is essentially random.

The effect of water saturation on transmittance light, which is depended not only water saturation but also on the spatial arrangement of water and air in the pore space of the scattering medium is also important property of the influence of water content on transmission. Hoa (1981) reported that the transmission is a function of the size distribution of the water-filled pores. A decrease of reflectance is caused either by a decrease in scattering leading to an increase of light propagation into forward direction or by light absorption in

water. The last cause is pronounced in the absorption bands of water.

Tidwell and Glass (1994), Niemet and Selker (2001) and Niemet *et al.* (2002) discussed the influence of water content on transmission. They describe light absorption with Lambert-Beer's law. In these studies the scattering medium was assumed to be homogeneous, i.e. the arrangement of water in the pore space was not considered. To calculate transmittance, the authors used the following refractive indices: sand $n_s = 1.6$, water $n_w = 1.33$, and air $n_a = 1.0$. The model presumes normal incidence and homogeneous distribution of water and solid phase. The experiments were designed in such a way that the samples were sufficiently translucent, yielding a quantifiable amount of transmitted light through a medium of significant thickness.

Bänninger (2004), Bänninger *et al.* (2005) considered that the properties which influence the reflectance and transmittance, and degree of the scattering is highly dependent upon the media thickness, size of the particles, the optical properties of the phases, porosity, wavelength, and the surrounding materials. They studied the principles of optics for inferring textural attributes of media surfaces from light scattering and developed a radiative transfer model to describe the physical processes of light propagation e.g., the geometry of multilayered film particles, orientation of light transfer, changing transmitted light configuration with water content, and the actual light paths through porous media.

A crucial issue in the porous Hele-Shaw cell is multi-light-scattering which reduces spatial resolution of transmitted light and also affects water saturation measurements. The qualitative behavior of a light beam passing through a sand-filled Hele-Shaw cell is illustrated in Fig 3.5 showing that light can be transmitted, reflected, scattered, or attenuated due to multiple reflection from the particles.

In all previous applications of the LTM only the transmitted light intensity is considered without any correction for light scattering (Tidwell and Glass 1994). However, multiple light scattering reduces the contrast between zones of different water contents and hence it affects one of the most important aspects which we intend to correct it in our experiments. Therefore a correction of the images is advisable. In this study, an image processing algorithm has been developed that exploits the multiple light scattering in observed image. This technique is the deconvolution using an experimentally measured response function (point spread function). We will describe this process in image processing chapter (4).

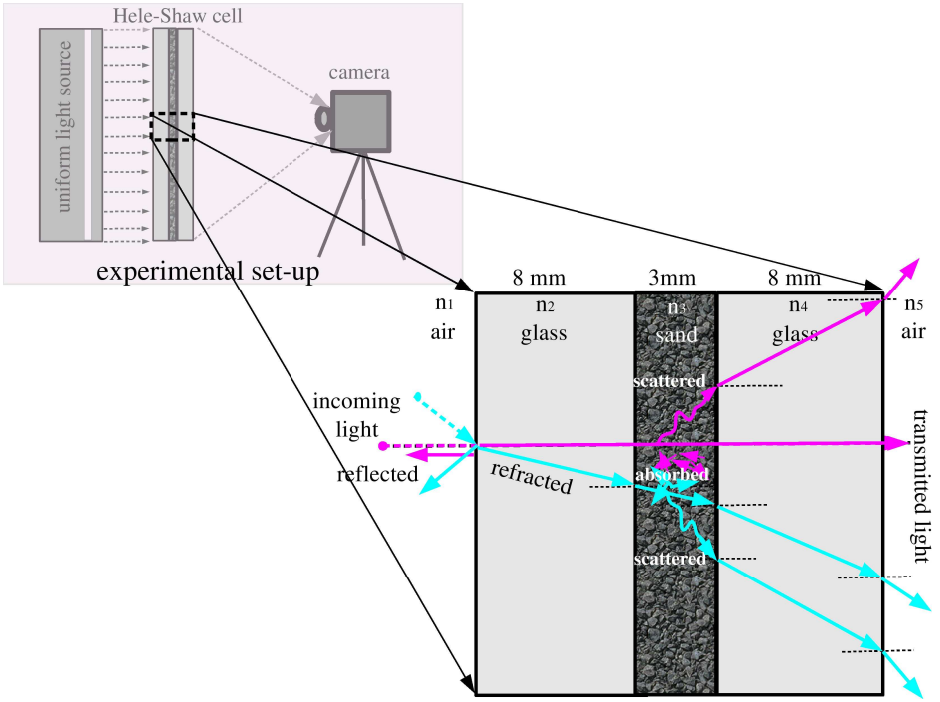

Figure 3.5.: Sketch of the optical paths of a light beam through a porous Hele-Shaw cell filled with sand. The possible events for light propagation are shown for a small section of the cell: light can be absorbed within each phase and scattered, reflected, and refracted at the interfaces between the different phases and the sand particles.

3.2.2. X-ray absorption

During the experiments simultaneous measurements of water saturation inside the cell were done by monitoring X-ray absorption. For the X-ray measurements, unlike LTM, there is a fundamental relationship between the attenuation of X-rays and moisture content. The X-ray consists of a polychromatic medical X-ray tube operated at 141 KV and 5 mA together with a 12 bit CCD line detector with 1280 pixel of 0.4 mm side length. Tube and detector were mounted at a distance of ∼2 m and can be moved synchronously in vertical direction from the bottom to the top of the cell.

The cell was placed between the X-ray tube and the detector. The images were acquired by directing a beam of X-rays to the face of the test media while

recording the transmitted intensity field with the detector behind the cell. To monitor the vertical distribution of water within a sample, the line sensor and the focus of the X-ray tube were placed in the same vertical position, at the bottom of the cell. Then both were moved synchronously from the bottom to the top of the sample. During the movement the intensity on the detector was measured at several positions. The positions and the velocity of the movement were adjusted to useful values. Measured X-ray intensities of each pixel $I(d)$ after passage of the thickness of the cell were related to the emitted intensities I_0 which were measured without the cell. The intensities for each pixel was corrected for the dark current of the respective detector pixel. This dark current was determined in an independent measurement. The absorption coefficient, μ, can be calculated as the product of the effective absorption coefficient, μ^*, and the pass length d of path of the photons through the material by the following relation:

$$\mu = \mu^*(x)\, d = \ln(\frac{I_0}{I(d)}) \ . \tag{3.4}$$

In Eq. 3.4, the effective absorption coefficient, $\mu^*(x)$, at sample height x is the sum of the length-fraction weighted absorption coefficients of the different components, hence:

$$\mu(x) = \mu^*(x)d = (1-\phi)d\mu_{\text{sand}} + d_{\text{glass}}\mu_{\text{glass}} + \theta(x)d\mu_{H_2O} + (\phi - \theta(x))d\mu_{\text{air}} \ , \tag{3.5}$$

where μ_{sand}, μ_{glass}, μ_{H_2O} and μ_{air} are the absorption coefficient of sand, the glass plates of the cell, water and air, respectively. Where d and d_{glass} are thicknesses of the cell and its glass, respectively, ϕ is the porosity and $\theta(x)$ is the distribution of the volumetric water content. Neglecting absorption of air, whose absorption coefficient is two orders of magnitude lower than that of the other present materials, the last term in Eq. 3.5 disappears. After measurements of the dry and the fully water saturated sample the water saturation, $S(x)$, can be calculated from:

$$S(x) = \frac{\mu(x) - \mu_{\text{dry}}}{\mu_{\text{sat}} - \mu_{\text{dry}}} \ , \tag{3.6}$$

where μ_{dry} is the calculated value using Eq 3.4 of the dry and μ_{sat} of the completely saturated sample (Bayer *et al.* 2004, Bayer 2005).

3.2.3. Limitations of techniques

Measurements of saturation with either technique require achievement of suitable image contrast. Contrast is defined here as the difference between the

intensity field transmitted through the test media and the transmitted through the dry test media.

For the X-ray technique, difficulties arise because of the low density of water relative to that of the minerals composing the porous media. Hence a large change in saturation produces only a small decrease in transmitted X-ray intensity. For the light transmitting technique, image contrast is governed by differences in the refractive indices of the air-sand and water-sand interfaces. In the air-water-sand systems contrast is exceptional without modification. The main disadvantage of the LTM in comparison to X-ray, is that the measurements depend on the translucence of the porous medium. Therefore the use of silica sands or glass beads and the thickness of the test media is limited on the order of a centimeter for most cases. Since this drawback can not easily be solved, three dimensional transient fluid observations will still have to wait a while. The principle advantage of this method is that it does not involve radiation and it enables us to visualize fluid content changes over the whole flow field with high spatial and temporal resolution. The X-ray measurements can also be performed with high spatial resolution but only at one location at one time. The high temporal measurement of the light transmission makes it especially suitable for transient flow experiments and compensates for that limitation.

3.3. Water Content Calibration

The motivation for calibrating the measured light intensity and water content is the physical processes of light propagation through porous media e.g., the geometry and orientations of multilayered film particles, changing transmitted light configuration with water content within the medium, and the actual light paths. The calibration of the LTM in order to get the water saturation was done by simultaneous measurements of X-ray absorption and light transmission. For this purpose we filled the homogeneous coarse sand into a smaller calibration cell with dimensions 30× 30× 0.3 cm. The water table within this small cell was adjusted with an inlet at the bottom of the cell. The cell was placed between the X-ray source and the detector with the glass plates perpendicular to the center ray. Simultaneous X-ray (vertical scan) and light transmission images were taken for three different situations: completely dry, water saturated and at hydrostatic equilibrium stage with several heights of the water table at the lower boundary. X-ray and LTM profiles were recorded for each water table through parallel measurements. The completely dry image as first reference was

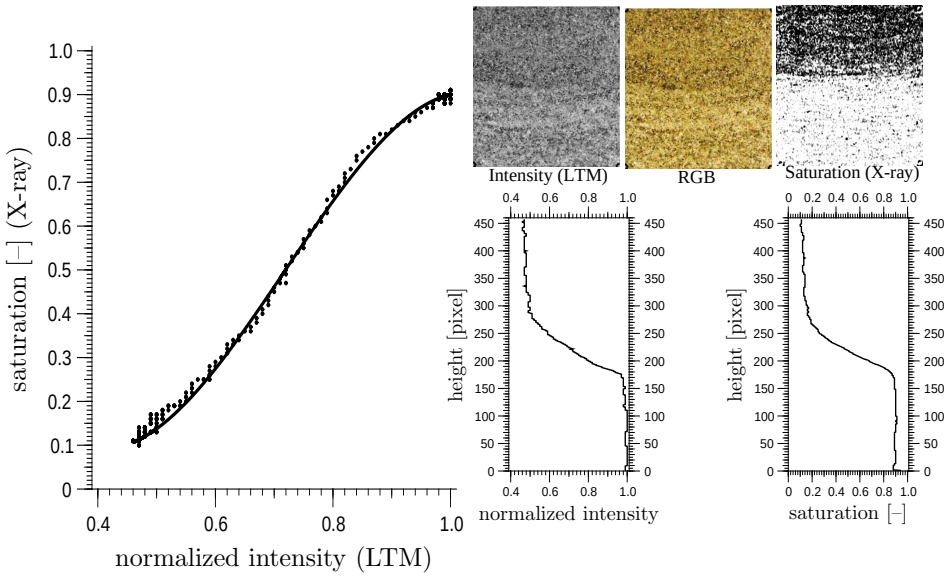

Figure 3.6.: Correlation between measured water saturation by relative X-ray absorption and the normalized intensities by LTM. Although the relation between transmission and saturation is nonlinear, the transmitted light is still a good proxy for water saturation.

taken before the sample came in touch with water and the image at saturation as second reference was measured at the end of the experiment, after the cell had been saturated by stepwise imbibition (to minimize air entrapments) of water through the bottom to the top of the cell. After fully saturating of the cell, the water table was decreased again in several steps and profile data recorded.

The vertical profile measurements of relative X-ray absorption and normalized light intensity as a function of cell height were compared with each other and agreement between two profiles of these two independence techniques was very close (Fig. 3.6). To decrease the signal to noise ratio the vertical homogeneity was improved and saturation and intensity were calculated by averaging of 400 pixels along a centered horizontal line. Since neither measurement technique gives the true value, we can only compare statistically how well both

methods agree. A regression analysis between the water saturation measurements by the relative X-ray absorption and by the normalized light intensities of the LTM indicates a relation by fitting a third order polynomial to the data with a correlation coefficient of 0.999 and a standard deviation of 0.010. We obtained:

$$S = 1.7 - 9I_{\mathrm{LTM}} + 15.3I_{\mathrm{LTM}}^2 - 7.1I_{\mathrm{LTM}}^3 \ , \tag{3.7}$$

where S is the distribution of water saturation calculated from the relative X-ray absorption coefficient using Eq. 3.6 and $I_{\mathbf{LTM}}$ is the normalized intensity with two reference measurements which can be expressed as:

$$I_{\mathrm{LTM}} = \frac{I - I_{\mathrm{dry}}}{I_{\mathrm{sat}} - I_{\mathrm{dry}}} \ , \tag{3.8}$$

where $I, I_{\mathrm{dry}}, I_{\mathrm{sat}}$ are the light intensities of the transmitted light for the partially saturated, dry and saturated sample, respectively. Equation 3.7 is valid only when the normalized intensity is between 0.47 and 1.00. The resulting S, I_{LTM} and calibration curves are shown in Figure 3.6. More details of image analysis to produce the intensity and normalized intensity images data are presented in chapter 4.

Obviously, the general shape of this fitted curve is non-linear. It starts with an initial non-linear shape in the range of low transmitted intensity and saturation, then in the range between 0.6 and 0.85 of intensity values looks linear and in the range of high values of intensity and saturation, it has the non-linear shape. The calibration curve has the only significant deviations, from the ideal data, in the range of non-linear shapes. This is because of comparison of these two independent techniques in the part of heterogeneity structure of sand. Fine-textured sands show higher saturation by X-ray measurements and lower transmitted intensity by LTM, and also in the range of high values, it could be resulted by pore spaces between the grains which shows much higher transmitted intensity in comparison with the real saturation measured by X-ray. By this correlation, the light intensity can be used as a proxy variable of water saturation. This calibration was used for all experiments in this study.

For sand the intensity of transmitted light increases with grain size. Notice that the constant values in Eq. 3.7 are valid only for the specific type of sand used in this project. The system needs to be calibrated each time a different camera or sand are used. This is the disadvantage of this calibration that holds only for exactly the material used. Other materials with different transmission properties have to be measured again with the procedure described above. Each

accurate determination of saturation from light intensities requires a careful calibration depending on the materials.

3.3.1. Calibration error

Errors that influence the results of the saturation calibration can originate from the comparison experiments of the X-ray and light transmission. The error due to the comparison experiment stem from the need to move the experiment between two facilities (X-ray and LTM). Slight cell movement can be translocated during the transport of the experiment carried about $\sim$2 m distance between the facilities. For each method the experiment also had to be aligned properly with respect to the source and detector. We adjusted all positions for X-ray and LTM measurements to examine exactly the same location of the cell and this was done using marked points on the aluminum frame of the cell as reference. A perfect alignment was impossible. A misalignment of above $1 - 2\,\mathrm{mm}$ can arise each time the cell was moved. Such misalignment can cause errors of few percent of saturation where moisture conditions are rapidly varying. Although, each of the X-ray and light images was adjusted and scaled for their geometric distortion by image processing applications on images.

Another source of error is given by technical differences between measurements techniques. There was a time lag of $20 - 30\,\mathrm{min}$ between X-ray and light transmission imaging, so the two distributions do not completely coincide.

4. Image Processing

In the present study, determination of water saturation from a sand profile was done by digital image analysis. The image adjustment, intensity conversion, inhomogeneous illumination correction, subtraction from background, and finally deconvolution were the processes of images analysis. An image processing code was written to analyze the images in order to transfer the optical proxy information (intensity) in each pixel/cell to the quantity of interest (phase saturation) using independently determined calibration functions. The purpose of this chapter is to provide an accurate and complete presentation of the image processing that leads to the results in next chapter. In the first section, we describe the procedures of pre-processing of an image. These procedures are: (i) image adjustment using space references, (ii) filtering, (iii) converting each pixel of image based on red, green, and blue value to intensity format, (iv) correcting inhomogeneous illumination and (v) subtracting from background (dry) image. In section 4.2, we will demonstrate how we correct the images from light scattering effect occurring during the light transmission through porous material by deconvolution.

4.1. Pre-processing of Images

This section describes the pre-processing of the acquired data, i.e. the digital images. The aim of this process is to transform the captured light intensity information into a corresponding set of intensity values which is then the basis for further evaluations. The value assigned to each pixel in the digital image which has been captured as a RGB format is generally coded on 24 bits per pixel. The pre-processing steps are presented below.

1- Noise Reduction: Digital sequence images exhibits temporal variability (i.e., noise) at each pixel as well as spatial variability. Because the spatial variability is constant in time, it influences measurements only if there is a camera shift relative to the fractured cell, whereas noise leads to an uncertainty in measurements at each pixel in every image. In the first step of pre-processing,

an adjustment of images is required to correct variations in the space. They are referenced to assure that the images from the experimental period could be compared. First, the serial images were adjusted for geometrical distortion using the spatial coordinates of the edges which are identified by marked points on the fixed aluminum frame of the cell as reference. By this adjustment, all images were corrected to represent exactly the same locations within the cell as well as for orthogonal directions and non-rotation of images. It was required because of slight movements of the imaging devices during the experiment, which produce noise on images. These corrections were done by cross-correlation analysis on images. After this procedure, the intensity values across the image are smoothed in order to eliminate noise. A common method for image smoothing and to remove noise effects is the median low pass filtering, which replaces each pixel value with the median gray scale value of its immediate neighbors. For our data evaluation, we applied a 5×5 median filter on each image.

2- Image Conversion: As we described in section 3.2, a pixel's color can be described by a RGB (Red, Green, Blue) vector or by an HSI (Hue, Saturation, Intensity) vector. In the RGB color model, the value of each pixel corresponds to the intensity of three primary color components. Each of these colors in original captured images were saved in a separate plane with 256 gray values. The direct application of the RGB color space is not suitable because this operation produces color shifts, which alter the image. A possible approach is a conversion of the RGB image into the HSI color space. Transforming a RGB image to an HSI format image was performed as a second step of image pre-processing using Eq. 3.3. Figure 4.1 shows an example of conversion for a partially wet sample. The best correlation to water saturation was found for the intensity component ($I = \frac{1}{3}(R + G + B)$) of the HSI system, hereafter referred to color saturation. The variable I shows the brightness of a pixel and higher brightness represents the higher saturation in the cell.

3- Dark Intensity Correction: Dark intensity contributions (image taken with a closed camera shutter: the so-called "dark image") were removed from all images for subsequent processing. This was done by subtracting the intensities of "dark image" from an original captured image with an equal exposure time. Measurements of the dark intensity have shown that it is fairly uniform in space and time with an intensity value between 0 and 4. Once the image of the experiment is corrected for any dark intensity, a flat-field correction can be

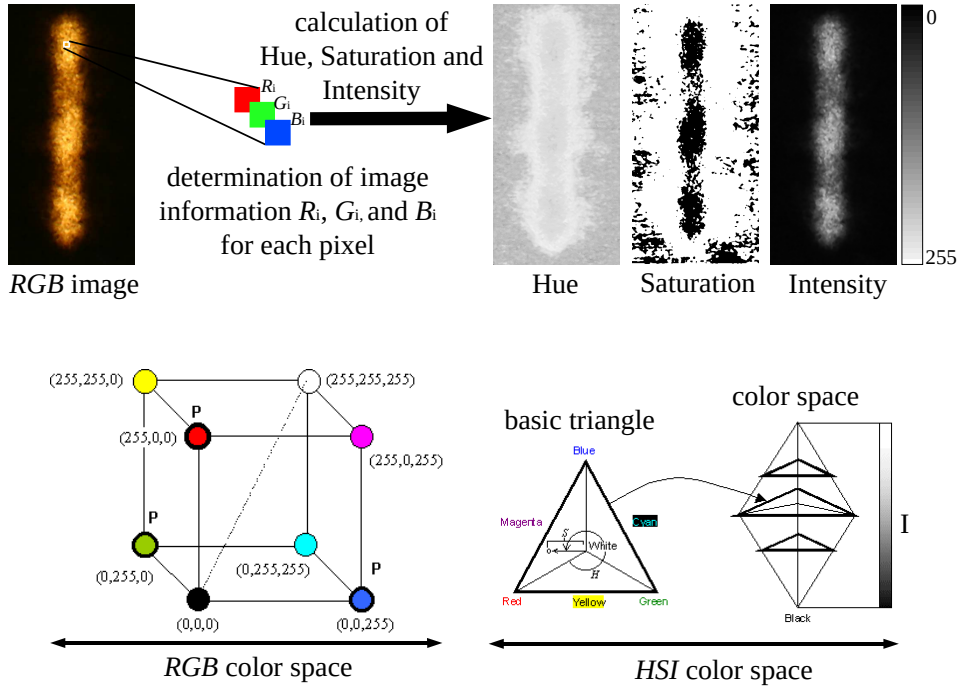

Figure 4.1.: Converting *RGB* image (**top left**) to *HSI* color space (**top right**) using Eq. 3.3 for a partially wet sample. **Bottom left:** the *RGB* color model has three basic primary colors (shown with **P** in cube): red, green, and blue. All other colors are obtained by combining them. **Bottom right:** in the *HSI* model, H (Hue) is the angle of the vector over the basic triangle, S (Saturation) is the proportional size of the module of the projection of the vector over the basic triangle and I (Intensity) is the distance from the end of the vector to the basic triangle. The intensity image (**top right**) shows better proxy for water saturation.

done.

4- Flat-field Correction: The visible light sources used for the transmission experiments should possess the qualities of diffusivity and spatial uniformity. But even under the best imaging conditions, the illumination across a field of cells is not quite uniform. This is due to imperfections contributed to each optical element within light source. Therefore a correction or rather

a compensation for inhomogeneous illumination was necessary. Flat-field correction was used to overcome the uneven illumination. The starting point for determining the flat-field illumination is having a background illumination emitted intensity which should be homogeneous throughout the view field at all pixels. Therefore, the background emitted intensities were measured for each experiment, separately. It was taken at a position where no sample was between light source and camera using the identical exposure times and acquisition settings. Any image $I(x, y)$ can be corrected, on a pixel-per-pixel basis, for inhomogeneous lighting by dividing it by a flat-field image $I_0(x, y)$ relative to the dark image $I_d(x, y)$ and rescaling as

$$I_F(x, y) = \frac{I(x, y) - I_d(x, y)}{I_0(x, y) - I_d(x, y)} \times 255 \ , \tag{4.1}$$

where $I_F(x, y)$ is the corrected image for inhomogeneous illumination by flat-field correction. Figure 4.2 illustrates the intensity image of a porous material sample before and after the flat-field correction.

5- Background Subtraction: A background image (dry) of the cell before the onset of infiltration was subtracted from the digitized image to yield an image that shows only the moisture content in the cell. Hence, the images are displayed according to light intensity at each location which allows the visualization of the relative moisture content. This was performed by an image processing procedure where a large portion of the original image was removed in the pictures by pixelwise subtraction the original image values by the corresponding background values. This process often is called "background subtraction". The processed images provide a pixel-by-pixel spatial distribution of the changes in water saturation which we call normalized. Then, the images were filtered again using a 5 by 5 median filter to produce the final normalized image.

We applied these pre-processing steps to each of the captured images. Figure 4.3 presents these pre-processing steps for two images captured from a dry and a partially wet sample.

4.2. Deconvolution Processes

As we described in chapter 3 (subsec. 3.2.1), during light propagation through porous media it leads to a specific spreading because of multiple light scattering. Deconvolution is being increasingly utilized for improving the contrast and

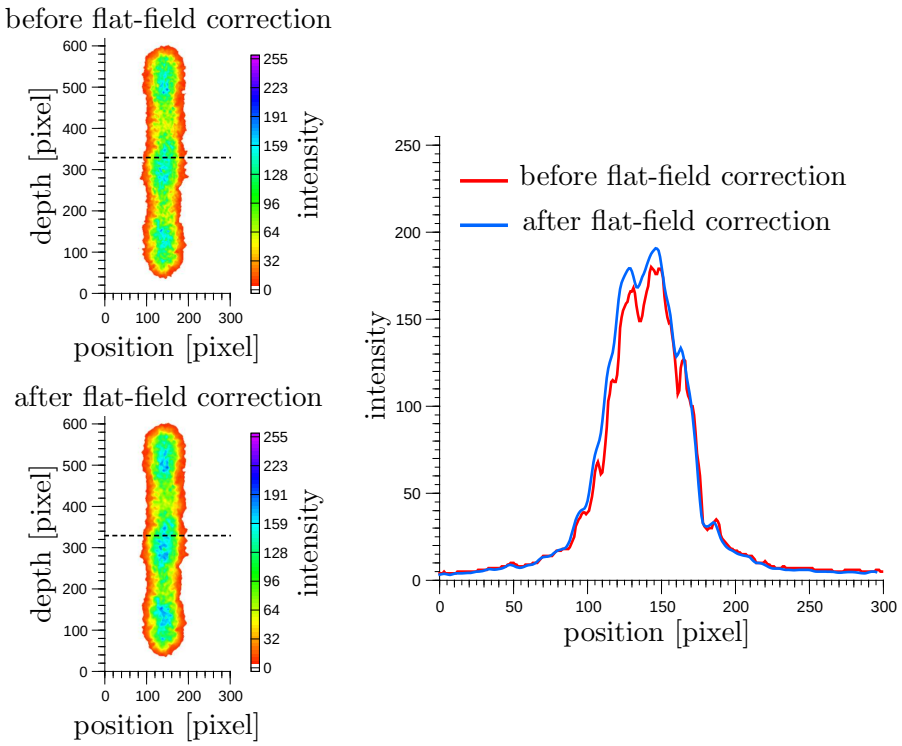

Figure 4.2.: Intensity image of a porous material sample before and after the flat-field correction for inhomogeneous illumination. The graph on the right shows the comparison of intensity values for a cross section at fixed pixel depth 330 before and after the flat-field correction. It results that illuminated flat-field image improves image uniformity.

correct the distortion of digital images to demand a true representative of the original image in presence of a determined Point Spread Function (PSF). Deconvolution is both a mathematical concept and an important operation used in digital image processing to recover an object from an image that is degraded by physical process of the optical system. This operation is an inverse filtering and its task consists in despreading the observed image in order to recover the original shape of the object. Deconvolution is a computationally intensive image correction and it is inherently unstable and highly sensitive to the effective measurement noise. It is capable of: removing noise, increasing contrast, and increasing resolution.

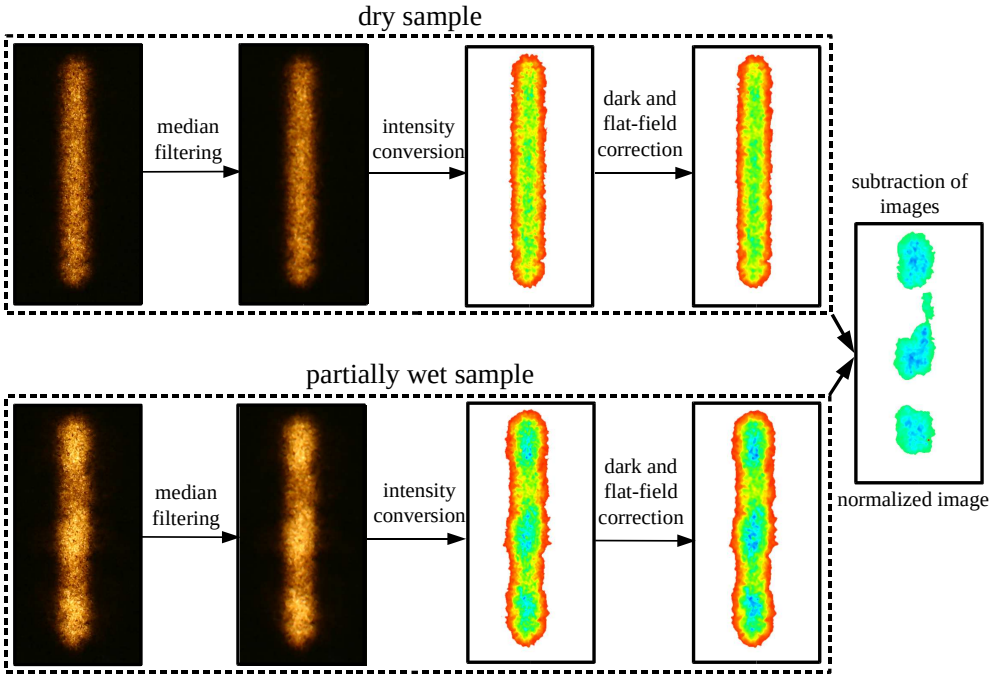

Figure 4.3.: Sequential steps of the image pre-processing for two-dimensional distribution from two images captured from a dry and a partially wet sample. The more water in the sand, the brighter location, allows to quantify the water saturation. The intensity of subtracted (normalized) image is rescaled to better visualization.

4.2.1. Point Spread Function (PSF)

The PSF plays an important role in the image formation and it is of fundamental importance to deconvolution and should be clearly understood in order to avoid imaging artifacts. Consequently, the image of transmitted light is convoluted by a PSF which is expected to be constant for homogeneous porous media and a fixed thickness of the transmitted layer.

We start with mathematical description for PSF. The one-dimensional PSF process can be mathematically described by a convolution equation. Let us assume that during an image acquisition stage, the original image is blurred by a PSF. Then, an observed light distribution f may usually be mathematically expressed as a convolution of the original (real) light distribution h and the

point spread function w as:

$$f(x) = \int_{-\infty}^{+\infty} h(x^{'})\, w(x - x^{'})\, dx^{'} \ . \tag{4.2}$$

In the first step to determine the PSF, we want to obtain w from observed f. The easiest way would be to use a very small slit, where the real image would be expected as the Dirac delta function $\delta(x)$. Experimentally, that is not realizable. Although, a very small slit would lead to additional diffractions of the slit itself. Therefore, a slit with a width much larger than the used wavelength must be used, where the real image can be mathematically expected as

$$h(x) = u(x - x_1) - u(x - x_2) \tag{4.3}$$
$$\text{with} \quad u(x) = \begin{cases} 0 & \text{for} \quad x < 0 \\ 1 & \text{for} \quad x \geqslant 0 \end{cases} \qquad \text{and} \quad x_1 < x_2 \ .$$

Hence, the PSF can be determined using first derivative of $f(x)$, which yields:

$$\begin{aligned} \partial_x f(x) &= \int_{-\infty}^{+\infty} h(x^{'})\, \frac{\partial}{\partial x}\, w(x - x^{'})\, dx^{'} \\ &= -\int_{-\infty}^{+\infty} h(x^{'})\, \frac{\partial}{\partial x^{'}}\, w(x - x^{'})\, dx^{'} \\ &= \int_{-\infty}^{+\infty} \Big[\frac{\partial}{\partial x^{'}}\, h(x^{'})\Big]\, w(x - x^{'})\, dx^{'} \ , \end{aligned} \tag{4.4}$$

assuming

$$\lim_{x' \to \pm\infty} h(x')\, w(x - x') = 0 \ , \qquad \forall x \tag{4.5}$$

$$\begin{aligned} \partial_x h(x) &= \partial_x (u(x - x_1) - u(x - x_2)) \\ &= \delta(x - x_1) - \delta(x - x_2) \ , \end{aligned} \tag{4.6}$$

herewith,

$$\partial_x f(x) = w(x - x_1) - w(x - x_2) \ , \tag{4.7}$$

where $w(x)$ is the PSF. Figure 4.4 shows the process graphically.

In our application, the specific PSF was measured experimentally using narrow slit with dimension 1×13 cm. To obtain more accurate PSF, we used 8 slits

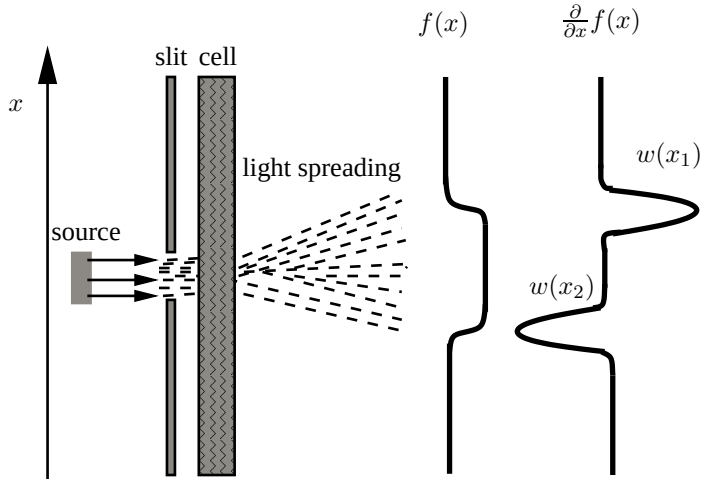

Figure 4.4.: Schematic representation of the method for measurement of PSF. The observed light distribution due to passage of light through a narrow slit leads that the light diffracts outwardly in all directions. $f(x)$ is the measured light intensity outside the slit, $\frac{\partial}{\partial x}f(x)$ is the differential form of $f(x)$ and $w(x_1)$ and $w(x_2)$ are the PSFs.

installed over on the back glass of the Hele-Shaw cell not only to the vertical but also to the horizontal directions at different locations. We installed 5 slits in vertical and 3 slits in horizontal direction. A photograph of the installed slits and porous medium into the cell corresponding to this situation, is shown in Fig 4.5(a_1-a_3).

We identified 3 lines along each slit through both horizontal and vertical directions. All derivative curves of the measured decreasing light intensities outside the slits, obtained by derivation of the cross-section transmittance data, were fitted using a Gaussian fitting procedure (Fig. 4.5(b-e)). According to mean Gaussian fit determined for both one-dimensional x and y direction, the two-dimensional Gaussian PSF can be determined as below:

$$\overline{w(x,y)} = \overline{w(x)} \times \overline{w(y)} \ , \tag{4.8}$$

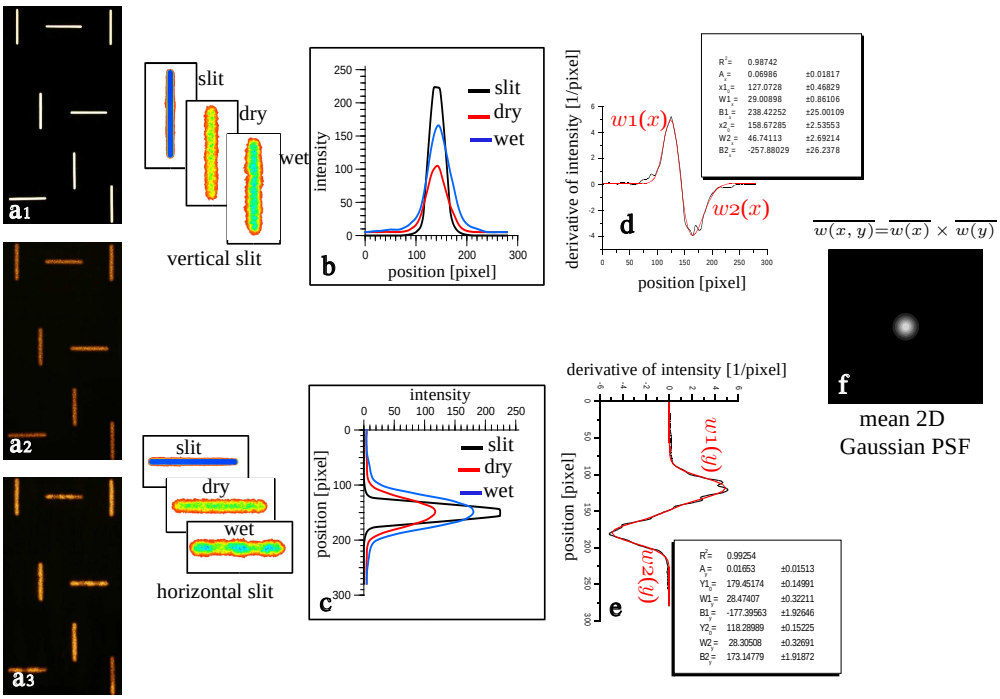

Figure 4.5.: The process procedure to measure the PSF. $\mathbf{a_1}$) Eight slits installed over the cell. $\mathbf{a_2}$) Dry porous material+slits. $\mathbf{a_3}$) Partially wet porous material after water infiltration from top of the cell+slits. **b,c**) Cross-section transmittance curves for an example of vertical and horizontal slit. **d,e**) A Gaussian fitted (red line) to the derivative curve of cross-section transmitted data (black line) measured for a vertical and horizontal slit. **f**) The mean 2D Gaussian PSF image obtained by combination of x and y direction fitted Gaussian distributions.

with Gaussian functions of the form

$$\overline{w(x)} := \overline{A_x} + \frac{\overline{B_x}}{\sqrt{2\pi\overline{W_x}^2}} \exp\left\{\frac{-(x-\overline{x_0})^2}{2\,\overline{W_x}^2}\right\} ,$$
$$\overline{w(y)} := \overline{A_y} + \frac{\overline{B_y}}{\sqrt{2\pi\overline{W_y}^2}} \exp\left\{\frac{-(y-\overline{y_0})^2}{2\,\overline{W_y}^2}\right\} , \tag{4.9}$$

where $\overline{w(x,y)}$ is the mean 2D Gaussian PSF, $\overline{w(x)}$ is the average of 15 Gaussian

functions obtained by 3 lines cross-section measurement through each of the vertical slits, and $\overline{w(y)}$ is the average of 9 Gaussian functions obtained by 3 lines cross-section measurement through each of the horizontal slits. These two functions, $\overline{w(x)}$ and $\overline{w(y)}$, are averaged over all fitted Gaussian parameters of both x and y direction where the mean parameters $\overline{\mathbf{p}_x}$ and $\overline{\mathbf{p}_y}$ can be defined as:

$$\overline{w(x)} = w(x; \overline{\mathbf{p}_x}) \ , \qquad \overline{\mathbf{p}_x} = \frac{1}{5 \times 3} \sum_{i=1}^{5} \sum_{j=1}^{3} \mathbf{p}_{x,ij} \ ,$$

$$\mathbf{p}_{x,ij} = (A_{x,ij}, B_{x,ij}, W_{x,ij}, x_0) \quad \text{with} \quad i = 1...5 \ , \quad j = 1...3 \ , \tag{4.10}$$

$$\overline{w(y)} = w(y; \overline{\mathbf{p}_y}) \ , \qquad \overline{\mathbf{p}_y} = \frac{1}{3 \times 3} \sum_{k=1}^{3} \sum_{j=1}^{3} \mathbf{p}_{y,kj} \ ,$$

$$\mathbf{p}_{y,kj} = (A_{y,kj}, B_{y,kj}, W_{y,kj}, y_0) \quad \text{with} \quad k = 1...5 \ , \quad j = 1...3 \ , \tag{4.11}$$

where the Gaussian parameter A is the baseline offset, B is the total area under the curve from the baseline, W is the width of the peak at half height, x_0 and y_0 are the center of the peak.

Finally, to remove the noise, the baseline offset A of the Gaussian was set to zero and using obtained two-dimensional Gaussian PSF, we generated an image that is called the PSF image for further deconvolution analysis (Fig. 4.5(f)). Note that the quality of the PSF is critical to the performance of a deconvolution algorithm and should be come under a very close scrutiny. A noisy PSF will have a disproportionate effect on the results of deconvolution and substantial noise will appear in the deconvolved image.

4.2.2. 2D deconvolved image

The two-dimensional image $f(x, y)$ can be represented by a convolution of the real image $h(x', y')$ with the point spread function $w(x', y')$ as the following double integral:

$$f(x, y) = \int_{-\infty}^{+\infty} \int_{-\infty}^{+\infty} h(x', y') \, w(x - x', y - y') \, dx' \, dy' \ . \tag{4.12}$$

The aim of deconvolution may be stated in the following way: given the image (f) and the point spread function (w), recover the original light distribution (h). The Fourier transform of this convolution from the spatial domain x, y to the frequency domain u, v is given by $F(u, v)$, where:

$$F(u, v) = H(u, v) \times W(u, v) \ . \tag{4.13}$$

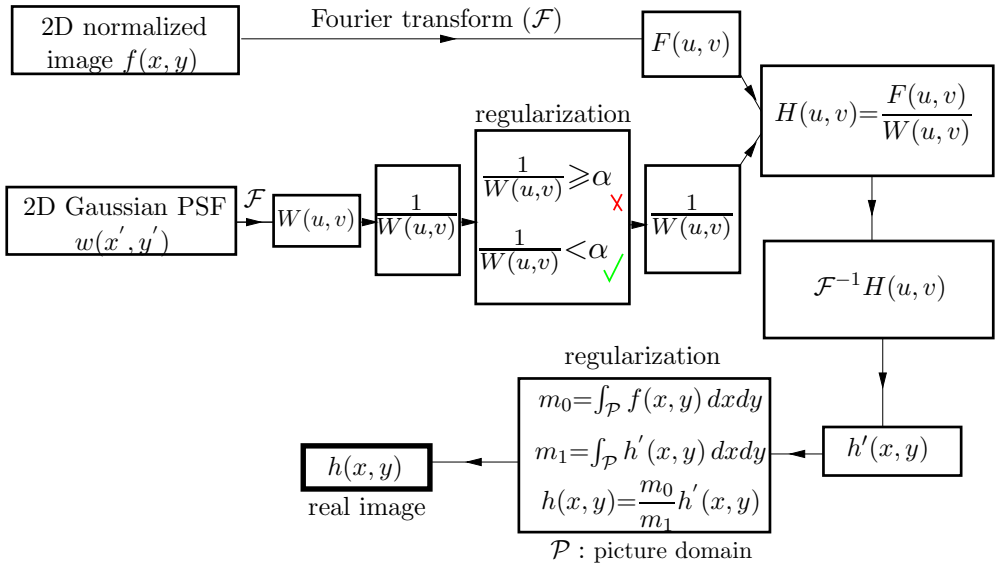

Figure 4.6.: Flowchart to illustrate the procedure of the image deconvolution. A deconvolved image generates from a input image and a PSF.

Herewith, the inverse of the PSF $(1/W)$ was obtained so that it can be multiplied by the image F image to get the real image H in frequency domain,

$$H(u,v) = F(u,v) \times \frac{1}{W(u,v)} \ . \tag{4.14}$$

After an inverse Fourier transform of the $H(u,v)$ we get the deconvolved image $h(x,y)$. During the deconvolution process, we used low pass filters for regularization in the frequency domain to reduce noise in which the higher frequencies are only partially lost. A more extensive description of the deconvolution theory and applications can be found in several textbooks and literatures, e.g. (Banham and Katsaggelos 1997, Biemond and Mersereau 1990, Kundur and Hatzinakos 1996, Bones *et al.* 1992, Press *et al.* 1992, Jähne 2002). All images were deconvoluted using the same PSF. Figure 4.6 illustrates the procedure flowchart of deconvolution on an image using PSF. This figure should hopefully make this process a bit more clear. Figure 4.7 shows the correction of multiple light scattering in an observed image for a porous material sample by deconvolution process. In this figure, the result of deconvolution before and after the process is compared with the slit. Figure 4.8 illustrates the sequen-

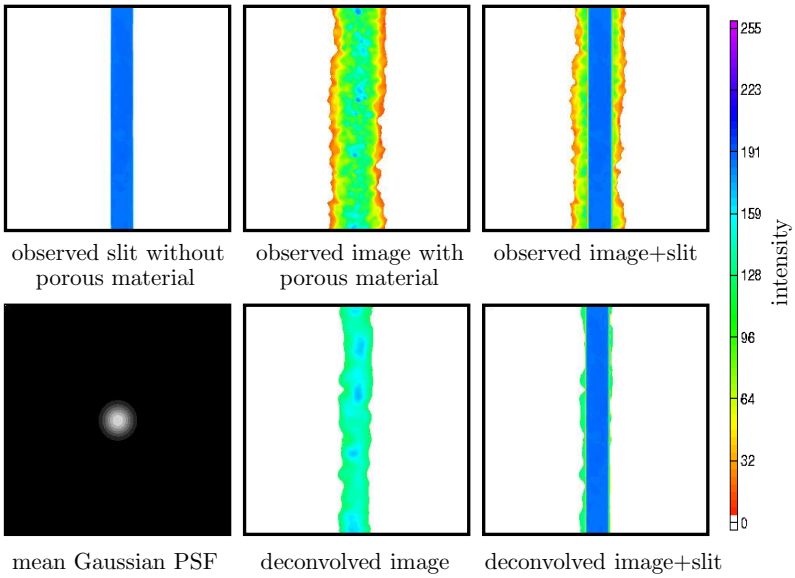

Figure 4.7.: Example of deconvolution results for an observed image with porous material using the Gaussian point spread function obtained from averaging eight horizontal and vertical slits distributed over the cell.

tial image processing for an example image of fingering flow experiment. The image after deconvolution process (real image) shows the despreading of the observed image in order to recover the original (real) shape of the flow pattern image.

In a separate experiment, we compared the width of finger using light and X-ray transmission measurements. In this experiment, for X-ray measurements, the cell was placed between the X-ray source and detector which both moved vertically. First image was taken by X-ray transmission, then the light source was moved to behind the cell for light transmission measurement. The results are presented in Fig. 4.9 that show the water contents along a cross-section through two fingers as measured with X-ray, LTM with deconvolution, and LTM without deconvolution. Clearly, the observed width of the fingers is reduced through deconvolution which better reflects reality. This is supported by the X-ray results in which, due to the less scattering effect of X-ray transmission through porous material in comparison with visible light. A perfect match between X-ray measurements and the deconvolved LTM image cannot be expected because of the technical reasons. As measurements were done first

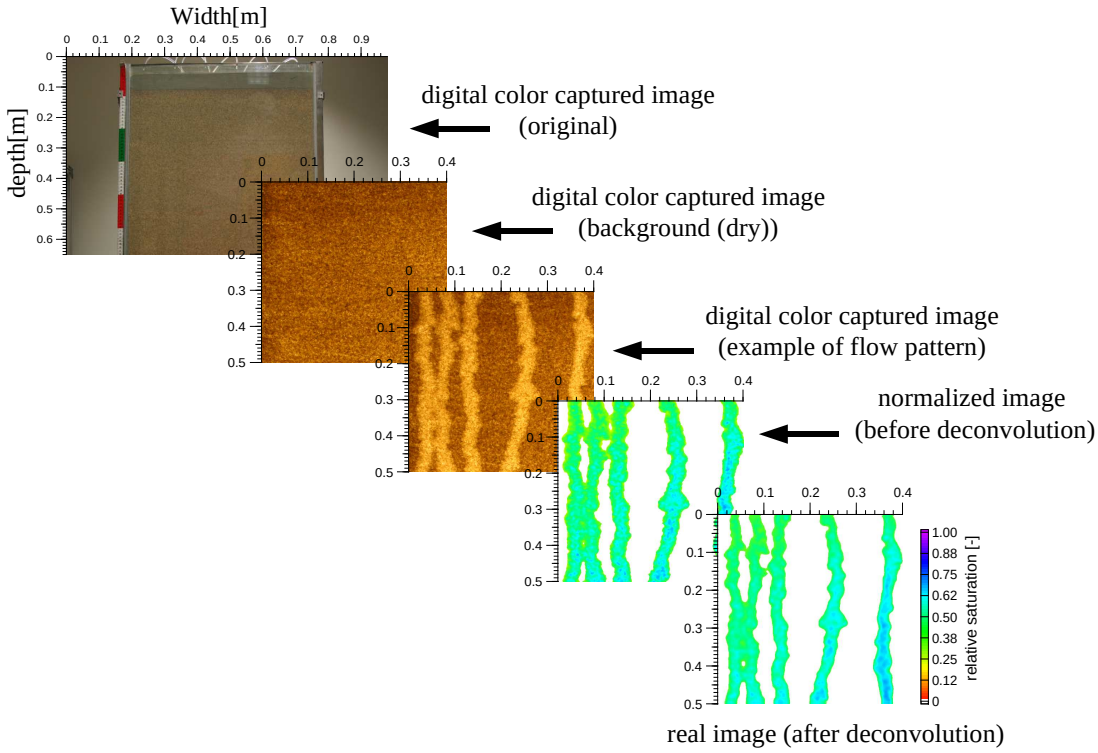

Figure 4.8.: Sequence of the image processing steps. The digital color background and example of flow pattern images are after geometrical correction from original captured image. The normalized image is the same flow pattern image but referenced to the dry image to visualize the water saturation. The real image achieved after deconvolution using the PSF.

by X-ray and then LTM, there was a time lag of 20 minutes between these two techniques when we moved the light source to behind the cell for the LTM measurements and hence, the two distributions do not completely coincide.

Finally, the images are prepared to proceed to the next step, quantification that will greatly depends upon the application. The digitized intensity level values are converted to water saturation through application of non-linear calibration curve (Eq. 3.7).

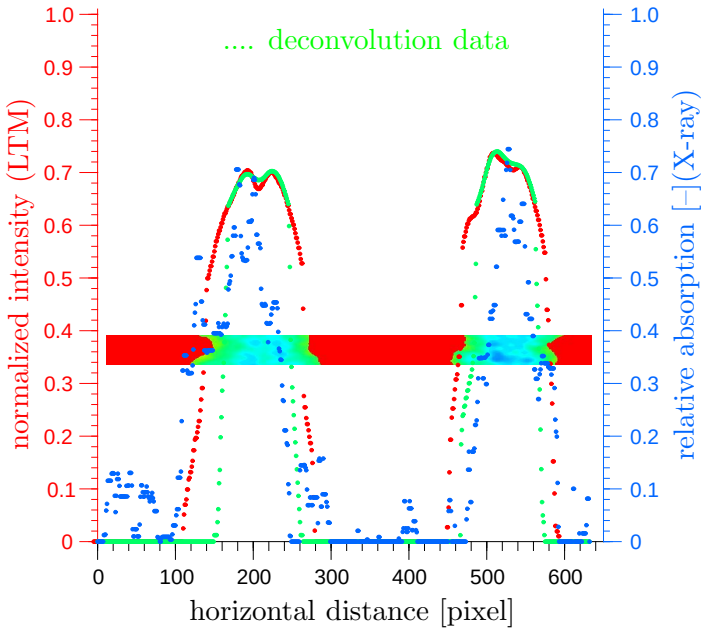

Figure 4.9.: Comparison of X-ray saturation (blue dots) and light intensity without deconvolution (red dots) and with deconvolution (green dots) for a horizontal cross-section through two fingers. There was a time lag of 20 min between X-ray imaging and light intensity measurements so the two distributions do not completely coincide.

5. Results and Discussion

Using the experimental setup described in the chapter 3, several experiments were performed with the aim to illuminate and analyze, qualitatively and quantitatively, the fingering flow in sand-air-water systems. Qualitative data, such as observation of the phenomena and quantitative data, such as the dimensions, velocity and water content dynamics of the fingers are of primary importance to understand the type of flow patterns which are presented in this chapter. The experimental evidences demonstrating gravity-driven instability in porous Hele-Shaw cell and development of the finger structure are considered in the first section, following with qualitative descriptions of saturation overshoot and physical explanation of the finger initiation and spatial path of the fingers. After the qualitative description, quantitative analysis of measurements of the finger behavior, including dynamics of water saturation and pressure in flow fingers, dynamics and stabilization of the fingers, finger width, and finger tip velocity following with further experiments under different conditions are presented.

5.1. Experimental Evidences

Laboratory experiments have shown that the redistribution process following the infiltration in homogeneous coarse sand is unstable, producing a series of the fingers. The flow instability is easily observed in a porous Hele-Shaw cell where a fine textured layer overlies a coarse layer. Fingering occurs when the infiltrated water meets, during its vertical movement, an interface of great variation of hydraulic conductivity and the flux is less than the saturated hydraulic conductivity of layers (Fig. 2.9). A capillary barrier effect exists between these two-layer structure where an inclined coarse layer is overlaid by a fine layer which the coarse layer tend to impede the flow from fine layer. In this study, $2 - 5\,\mathrm{cm}$ of water (depending to used flow rate) was ponded on the surface of the fine layer and redistribution of the fingers began at about $10 - 15\,\mathrm{min}$ (depending on the interface shape between the fine and the coarse layer) after starting of infiltration. Qualitative observations imply that finger development

is strongly correlated to the structure of the imbibition front at the onset of flow redistribution.

5.1.1. Observations

In all experiments, the onset of a stable wetting front in the upper fine-textured layer characterized by a relatively low saturated hydraulic conductivity was observed which supplies uniformly water to the underlying coarse-textured layer characterized by a high value of saturated hydraulic conductivity. At the textural interface between the fine and the coarse layer the water moves in preferred paths or "**fingers**" at many discrete points induced by infiltrating flow. After visualization of the stable infiltration fronts and subsequent transition to instability in homogeneous coarse layer, the flow fingers disturbed within the underlying heterogeneous layer. Figure 5.1 shows a qualitative record of the advance of the downward growing fingers through an initially dry porous Hele-Shaw cell by time-lapse images during an experiment with constant flux of $1.2\,\mathrm{mm\,min^{-1}}$. The elapsed time is indexed from $t = 3\,\mathrm{min}$, defined as the moment when water is uniformly infiltrating downward with a nearly horizontal wetting front in the depth of 5 cm of the fine layer indicating that the flow process was stable. When the wetting front reached the critical depth (interface between the fine and the coarse layer shown in Fig. 5.2), the downward movement of the wetting front was observed to slow down and a pause for few minutes ($t = 12\,\mathrm{min}$). During the pause suction gradients at the interface will continue to diminish until the water pressure of the bottom layer is archived. Once the water pressure is archived, the wetting front crosses the interface into the coarse-grained sublayer and the front becomes unstable and fingering forms at several locations and penetrated deeper into the coarse layer (more details of the finger initiation are described in section 5.2). These fingers grew and propagated in depth interval between 0.07 m and 0.58 m with different velocity, width and spacing and encountered to middle heterogeneous layer. Obviously, the increased capillary forces within the fine textured areas of the heterogeneous middle-layer (depth interval between 0.58 m and 1.07 m) were sufficient to disturb the flow fingers. In this layer finger movement in the vertical direction was significantly reduced and became horizon gradually. Generally, the overall effect of heterogeneous media is to make the finger less regular. However, as soon as the fine textured heterogeneities disappeared, the conditions again became favorable for flow fingers and they reappear in the homogeneous layer below and moved downwards to the cell bottom.

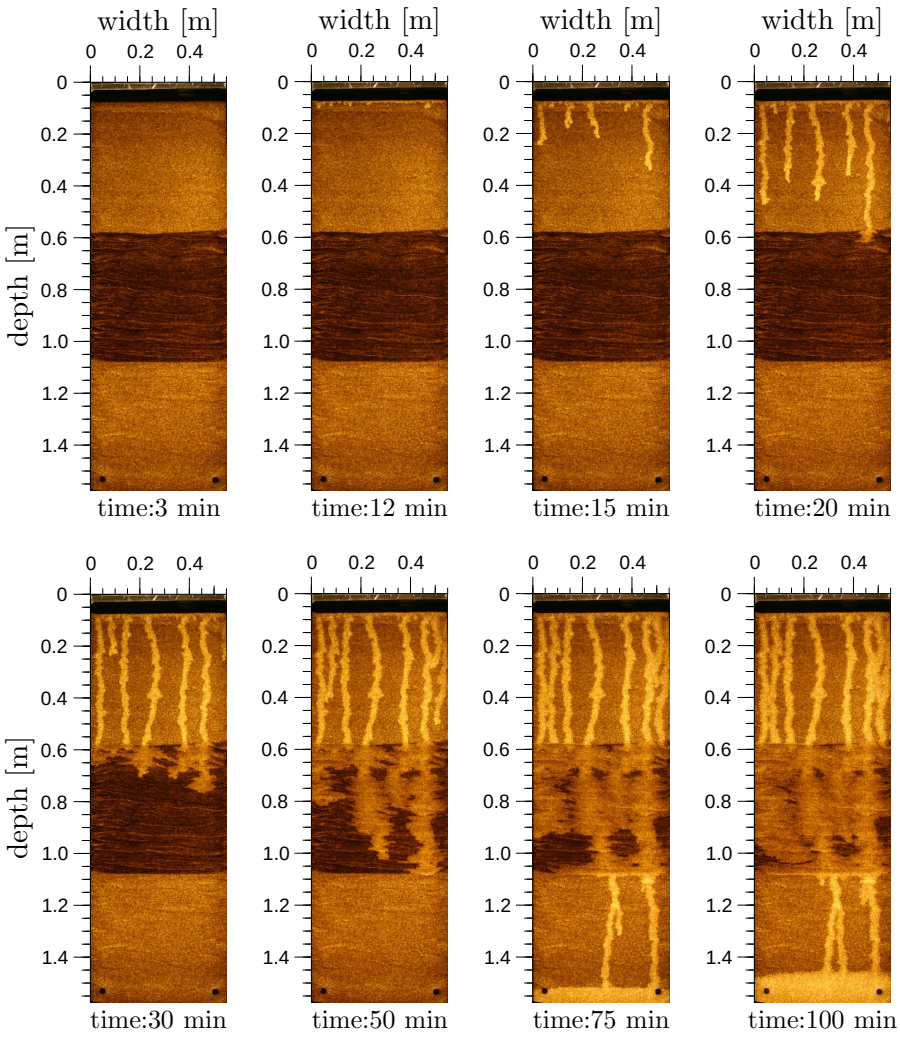

Figure 5.1.: Photographic sequence of images showing the downward growth of water fingering observed by light transmission into dry Hele-Shaw cell at eight different times. Water infiltration with constant water flux of $1.2\,\mathrm{mm\,min^{-1}}$ into the uniform medium leads to infiltrating fingers due to a flow instability. Flow instability is induced at the transition from the fine-textured sand (dark top layer) to the coarse-textured sand. The fingers are disturbed within the heterogeneous middle-layer and reappear in the uniform layer below. Fingers in homogeneous coarse layer sand, show several instances of the fingers merging, as well as a case of splitting. (see more pictures of this experiment in appendix A.1)

.

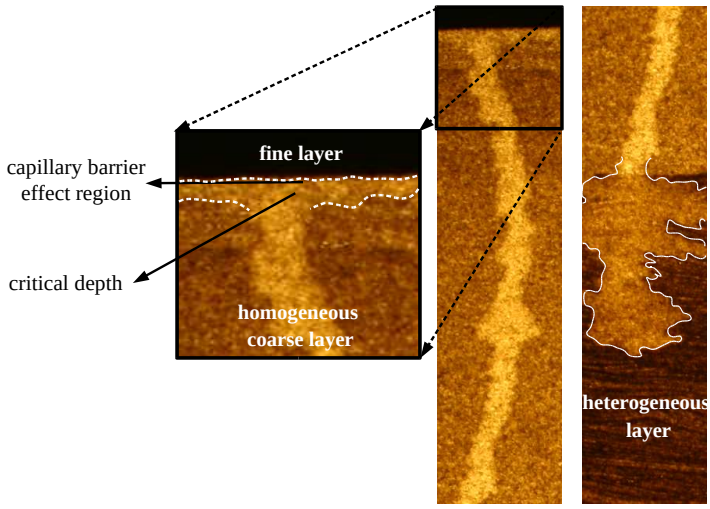

Figure 5.2.: Redistribution of uniformly applied water through fine and coarse sand. In the left picture, dashed line shows the critical depth of infiltration during redistribution in a fine sand and extended to a coarse sand. Unstable flow develops when a wetting front in the coarse sand exceed the critical depth of wetting. Right picture shows the destruction of the finger flow channel when it encounters heterogeneous structured layer.

Observation of the fingering process have repeatedly shown that some fingers do not carry enough water to keep downward growing downwards, and the number of the fingers decreases with increasing depth. In sand that is not completely homogeneous, the fingers deviate from a strictly vertical path, and merged to form larger and faster moving fingers which continued to move downward. When this happens, they come together like the arms of a Y (Fig. 5.1). These merging and splitting created by small media heterogeneity show the convergence and divergence structure of flow fingers. After a merger, the continuing finger carries considerably more water than either of the contributors and the extra water increases its conductivity and, in accordance with the conservation of mass, its speed grows.

5.1.2. Flow field structure using tracer experiment

After fingers had fully developed, a dye tracer (Brilliant Blue) was added to visualize local flow velocities. It demonstrates the high separation of a mobile

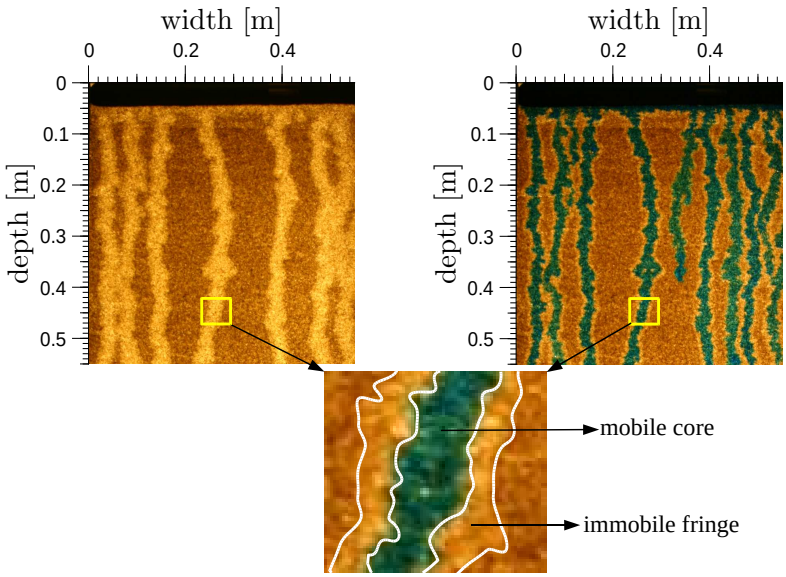

Figure 5.3.: Infiltration of dye tracer into stabilized water fingers highlights the separation of the water phase into a mobile component (core) and an immobile one (fringe).

and an immobile component of water within flow pathways of the fingers which has implications for solute transport. This shows the high velocity in the center and stagnant water at the periphery of the fingers. Here it could be hypothesized as separation of a portion inside the finger (from here on called the "finger **core**") with convective gravity driven flow and a portion at the boundaries of the finger (from here on called the "finger **fringe**") with slow and diffusive flow (Fig. 5.3).

Figure 5.4 shows photographs of the dye wetting front patterns taken at different times during the second cycle of infiltration into previous water fingers of the experiment shown in Fig. 5.1 with the same flow rate. The redistribution time is indexed from $t = 110\,\text{min}$, defined as the moment when dye was penetrating into top fine-textured layer. As soon as the dye reached to the fine-coarse interface, at $t = 115\,\text{min}$, dye started flow into the old fingers paths. Two additional fingers were emerged in the coarse layer between the previously generated fingers, one in the middle and the other at the third position from the right side. Dye fingers gradually diffused into the heterogeneous layer and found the previous finger pathways at the bottom of the cell.

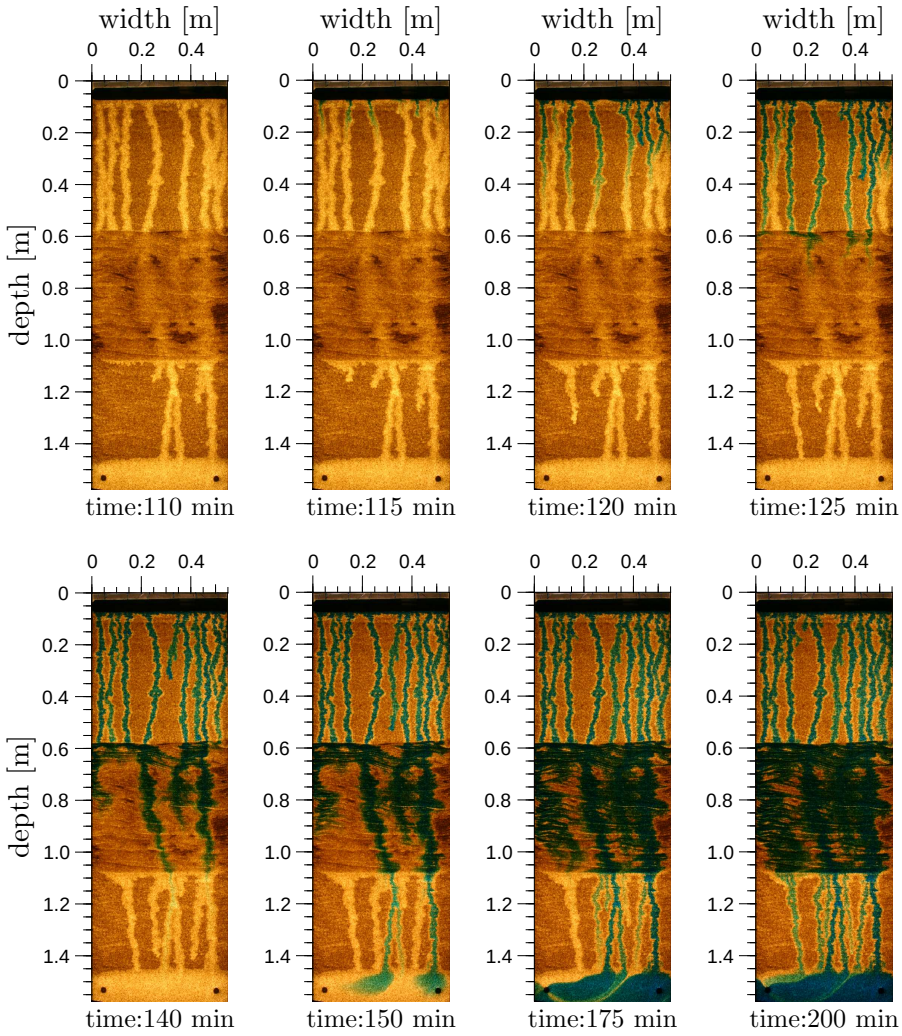

Figure 5.4.: Development of the dye fingers in the experiment with Brilliant Blue tracer infiltration with constant flux of $1.2\,\mathrm{mm\,min^{-1}}$. The dye flows only through the core and follows the same paths as the water. The locations of the core region as highlighted by the blue dye tracers were almost the same as in the water infiltration experiment. It shows the persistence of dye fingers into previously established path by water fingers. (see more pictures of this experiment in appendix A.2)

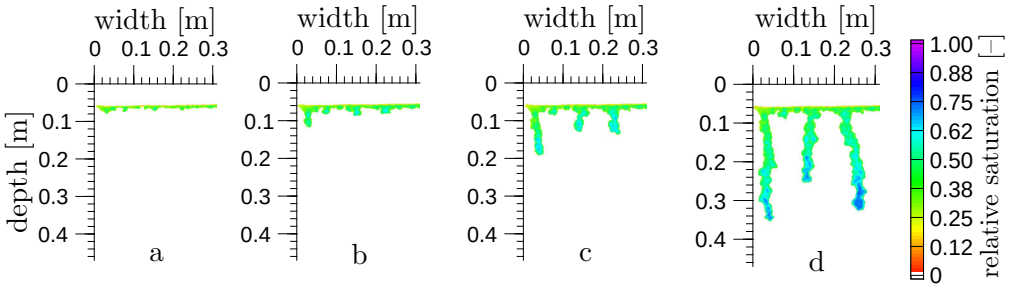

Figure 5.5.: Sequence illustrating the development of instability in an initially dry sand. a) advancement of stable front ($t = 11.5\,\text{min}$), b) onset of instability ($t = 12.5\,\text{min}$), c) development of the fingers ($t = 13.5\,\text{min}$), and d) developed fingers ($t = 17\,\text{min}$). The times refer to the time after starting of water infiltration.

5.1.3. Finger development in initially dry sand

To generalize the description of the finger flow field structure, an illustrative example of the transition to instability and subsequent development of the fingers is shown in Figure 5.5. The initial wetting front begins from many separate points that rapidly influences into a stable front (Fig.5.5a). Behavior of the stable wetting front changes entirely with continuous slug of infiltration and redistribution begins and the onset of instability is observed (Fig.5.5b). The front shown in Figure 5.5b exhibits four growing fingers that have developed from stable front. The second finger from the left-hand has the smallest length of the three fingers and it shows less competition to develop. After the onset of instability, individual fingers begin to rapidly develop, grow and forming distinct fingers (Fig.5.5c). The developed fingers are more likely separated fingers with very fast vertical movement and a downward growing tip consist of fully water spanning that will be referred to as the finger tip. Finger tips are essentially short, locally saturated water that partially drain along their trailing edge as they propagate downward. This phenomenon is called "**saturation overshoot**".

5.1.4. Saturation overshoot

As a finger grows downwards from the textural interface, there is a narrow zone of about $5 - 7\,\text{cm}$ (depends on the applied flux) at the finger tip where the water saturation increases rapidly. These maximum values are required to

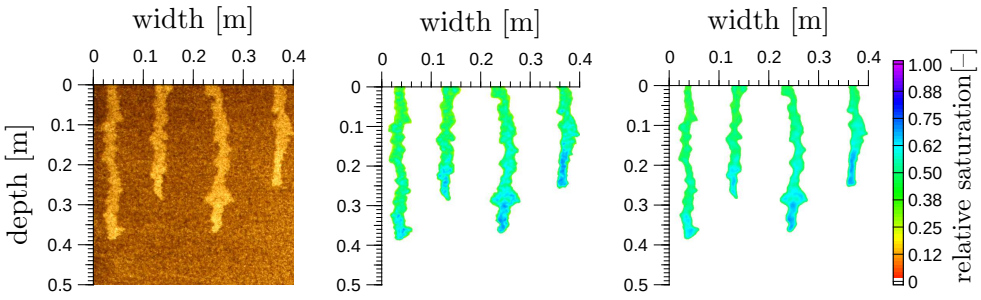

Figure 5.6.: Fingered flow in a homogeneous initially dry sand as observed with transmitted light (left). The same image but referenced to the dry image as normalized image to visualize the water saturation (middle) and image after deconvolution using the PSF (right) shows the highly localized flow paths that originate from the flow instability in the uniform part of the medium. Note the saturation overshoot in the tips.

advance the water front into the dry porous medium. This pattern consists of a region directly behind the wetting front with a high water saturation called finger tip, followed by another region with a lower water saturation called finger tail. The water saturation in the tip of the finger is close to saturation (~ 0.8) and drops at a short distance behind the advancing tip to ~ 0.5 (these values are for the experiment with flux $j_w = 1.2\,\mathrm{mm\,min^{-1}}$ and depend on the applied flux). An example of the downward growth of the fingers in an initially dry porous medium and typical finger moisture content structure during the water infiltration after 20 min infiltration is shown in Figure 5.6. This figure shows the typical finger moisture content structure during the rapid growth stage with saturation overshoot in the tip. The bluest color at the tip indicates the highest water saturation.

5.2. Physical Explanation of the Finger Initiation

The current understanding is that fingers develop in coarse-textured media if the driving force, typically gravity, dominates the capillary force. The relative weight of these two forces is given by the bond number, $\mathrm{Bo} = \rho g r^2/\sigma$, described in section 2.2. The characteristic length scale r which is related to the size of the pores, indicates that fingers occur only in coarse-textured porous media having

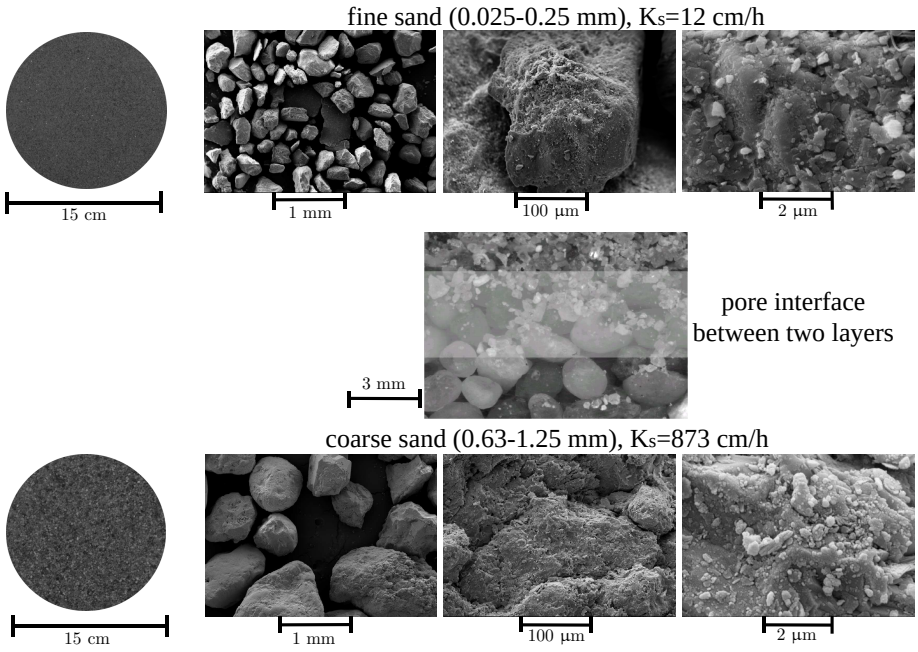

Figure 5.7.: Photographs of the grain size distribution and particle shapes for the fine (top) and the coarse (bottom) sands used in the experiment. The pore interface acts as a water flow gate between two less permeable fine toplayer and more permeable coarse sublayer. The length scale for images are given below of images.

pores above a critical size. In experiments the fingering phenomenon is actually found in granular media with a mean grain size above $0.5-1.0\,\mathrm{mm}$ in diameter (Diment and Watson 1985, Glass *et al.* 1989b). A developed conceptual model of Jury *et al.* (2003) for predicting the development of unstable flow during redistribution predicts that all soils are unstable during redistribution, but shows that only coarse-textured soils and sediments will form fingers capable of moving appreciable distances. It was shown by Flekkøy *et al.* (2002) that the width of the fingers increases with decreasing Bo. A microscopic view of the grain size distribution as well as particle shapes of the fine and coarse sands used in the experiment is presented in Fig. 5.7.

The dynamics of water pressure may be the most important in the finger initiation and formation process because of its role in determining the boundary condition at the wetting front. Wang *et al.* (2000) measured the water-

entry pressure with a water ponding method for water-repellent soil and with a tension-pressure infiltrometer method for both water-repellent and wettable soils. Using the concept of dynamic capillary pressure, DiCarlo and Blunt (2000) obtained a self-similar solution to a moving finger with a curved interface, where the capillary pressure depends on the velocity of the moving interface.

A physical argument can be used to illustrate why the process of water infiltration into a vertical profile of two-layer sand (fine-over-coarse) initiates unstable fingered flow. We consider the wetting front propagation into a two-layer system consist of a fine overlies a coarse sand, separately for each layer. In our applied set-up, the dynamics of water saturation inside the fine toplayer that is important to understand the finger propagation was not possible to measure using LTM, because light could not pass through the very fine sand particles. For this purpose, we measured the water pressure (p_w) inside the fine toplayer using three pressure sensors installed at different locations over the 20 cm depth of the fine toplayer, indicated by red, green, and blue circles in Fig. 5.8 (top right).

5.2.1. Distribution of flow in the fine-textured toplayer

Continuous water infiltration creates a ponded water over the fine layer surface ($z = 0$). A wetting front forms within the initially dry toplayer and advances downward continously, in response to the combined matric and gravitional potential gradients. The results of water pressure measurements into the fine toplayer show that when the wetting front reaches the interlayer interface ($z = z_2$), it pauses at that interface (**1** in Fig. 5.8, top right and bottom left). During that pause, potential gradients in the toplayer continue to induce flow toward the interface. This process acts as a capillary barrier system. Under this condition, when the pores in the fine layer above the interface are water filled, while the coarse sand is nearly dry, the hydraulic conductivity of the fine sand can be several orders of magnitude larger than in the coarse sand. The wetting front that builds up above the interface flows up within the toplayer. In this state a quasi-hydrostatic pressure distribution in the fine layer is established while in the coarse-textured layer matric potential is very negative. Due to continuous infiltration in the vertical direction, at a certain distance the toplayer is sufficiently saturated as well as its hydraulic conductivity increased, that capillary forces in coarse layer pull forward the moisture from fine into the coarse layer.

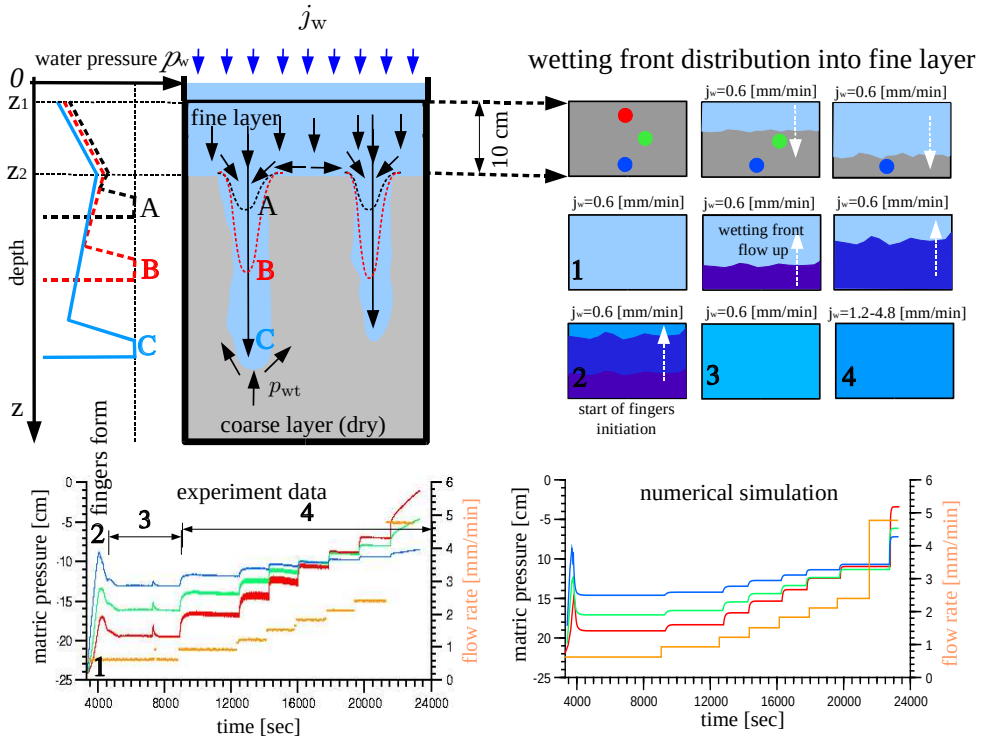

Figure 5.8.: Evaluation of wetting front development into a vertical profile consisting of two-layer sand. **Top left:** Formation and propagation of the finger during redistribution, when the pressure decreases toward the surface. The dry region below the wetting front must have a threshold water pressure (p_{wt}), which allows water to enter the dry region. **Top right:** Sketch of wetting front distribution in the overlying fine-textured layer during infiltration starting with constant flux $0.6\,\mathrm{mm\,min^{-1}}$ and additional infiltration with multi-step changing of flux in the range $1.2 - 4.8\,\mathrm{mm\,min^{-1}}$. **Bottom left:** The real measured water pressure using three pressure sensors installed at three locations inside the fine toplayer indicated by red, green, and blue circles in top right sketch. In the overlying fine layer, pressure drops upon initialization of new fingers. In the case of both developing and initiating of the fingers, the water pressure inside the fine layer decreases slightly. **Bottom right:** One-dimensional numerical simulation modeled data of wetting front distribution into the fine toplayer obtained with the HYDRUS model. The time refers to the time after starting of water infiltration.

This break down of the interface happens in the crossing of the hydraulic conductivity function between the fine and the coarse textured sands is shown in Fig. 2.3a. With entering the moisture into the coarse layer, pressure in the overlying fine-textured layer drops upon initialization of a new finger (**2** in Fig. 5.8, bottom left).

A simple one-dimensional numerical simulation using a hydraulic model of van Genuchten-Mualem parameterization showed the same results as found in the experiment measurements. The simulation results obtained with the HYDRUS model of Ŝimûnek *et al.* (2005) using a profile consisting of two layers and with the upper fine sand layer having a depth of 20 cm and the lower coarse sand layer having a depth of 130 cm. The hydraulic parameters values of the used sand were adapted from Cheng (2004). Two graphs in Figure 5.8 (bottom left and right) show the observed and modeled pressure head in the fine layer. The numbers indicate the wetting front distribution in the fine layer in comparison with the numbers indicated in top left sketched figures. This simulation shows that Richards' equation can explain the stable wetting front distribution into fine toplayer. We found that in the case of both developing and initiating of the fingers, the water pressure in the fine layer decreases (see the slight pressure decreasing after drops in Fig. 5.8, bottom left).

5.2.2. Initiation of the finger in the coarse-textured sublayer

With percolating of the infiltrating water from fine into the coarse layer the suction at the interface falls below a threshold of water pressure (p_{wt}) into the pores in the sublayer, and the wetting front then begins to move into the sublayer. Because of inevitable spatial variability, what typically happens below the interface is that water first penetrates the sublayer at distinct randomly distributed locations, rather than uniformly over the entire area of the interface. Such locations may not immediately admit the full flux deliverable by the toplayer; hence the suction at the interface may continue to decrease. The water pressure at the interface between wet and dry zones of developed wetting front is at a threshold water pressure, which allows water to enter the dry region. Because so much of the void space suddenly fills as this threshold is reached, the conductivity of the medium changes from negligible to high. Hence, the wetting front advances into coarse-textured sublayer and the water pressure behind it is lower than the pressure near the wetting front.

The downward advance of the wetting front within the sublayer becomes "unstable" with a spatially rapid movement and the front will grow into commonly called fingers. The system described is illustrated in Fig. 5.8 (top left).

This figure shows the formation and propagation of two fingers during redistribution. Three wetting front positions during passage of the finger have been indicated by A, B, and C. The graph in the left side of this figure shows that during finger advancement, the water pressure behind the wetting front is lower than the pressure near the wetting front and the lateral flow behind the wetting front decreases slightly the matric potential of the sand adjacent to the finger. For example, in position C of the wetting front, the pressure near wetting front is higher than behind the wetting front (point B), then the lateral flow at point B occurs and finger develops more.

5.3. Why does the Saturation Overshoot Occur?

Several experimental observations by Glass *et al.* (1989c), Selker *et al.* (1992b), Liu *et al.* (1994a), Geiger and Durnford (2000), DiCarlo (2004) have shown that gravity-driven fingers exhibit saturation overshoot. From these observations, it has been proposed that saturation overshoot is a necessary and sufficient prerequisite for gravity-driven fingering, i.e., gravity-driven fingering will occur if and only if saturation overshoot occurs. Thus a correct understanding of the physics controlling saturation overshoot is necessary for understanding the larger question of gravity-driven fingers (Eliassi and Glass 2001; 2002, DiCarlo 2004). Figure 5.9 (left) shows sketch of a fingering flow path and the associated saturation along flow fingers with saturation overshoot in the tip. Selker *et al.* (1992b) have shown that saturation overshoot is associated with an overshoot in water potential which decreases from the tip to tail of the fingers. Geiger and Durnford (2000) found pressure overshoot for initially dry coarse sands at large range of flow rates, and for initially dry fine sands at moderate flow rates, but with no pressure overshoot for initially wet sands or for the fine sands and low flow rates. Note that saturation overshoot occurs only during the unsaturated infiltration, causing unstable flow. It has been found that saturation and pressure overshoot are eliminated with increasing initial water content (Glass and Nicholl 1996, Bauters *et al.* 2000).

DiCarlo (2004) summarized the newer developments which focus on the nature of the saturation overshoot in the finger tip. He worked with light-transmission in a narrow column that corresponds to a one-dimensional system and showed that saturation overshoot is strongest for intermediate fluxes. He found that saturation overshoot ceases below a certain minimum and above a certain maximum infiltrating flux. This limit flux depends greatly on the grain smoothness and initial water content of the media and slightly on the mean

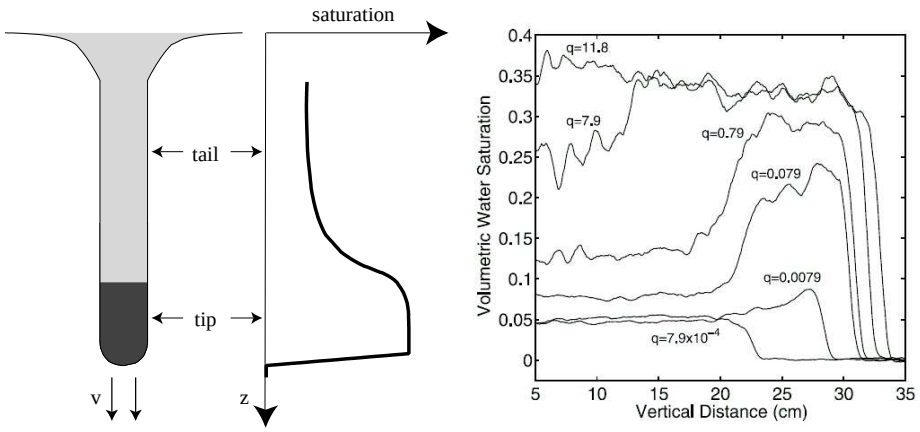

Figure 5.9.: **Left:** Sketch of a fingering flow path and the associated saturation within the flow path. Saturation overshoot occurs when the tip saturation is greater than the tail saturation. **Right:** Saturation profile versus depth for six different applied fluxes in initially dry porous column measured using light transmission. At the highest ($11.8\,\mathrm{cm\,min^{-1}}$) and lowest ($7.9 \times 10^{-4}\,\mathrm{cm\,min^{-1}}$) fluxes the profiles are monotonic with distance and no saturation overshoot is observed, while all of the intermediate fluxes exhibit saturation overshoot. (Figure 1 and 5 from DiCarlo (2004))

grain size. He measured the saturation overshoot as a function of infiltrating flux, mean grain size, grain sphericity, and initial water content. The observations of DiCarlo (2004) can be readily understood: (1) At very low flow rates (in one-dimensional) the wetting of the solid surface is fast compared to the speed of the advancing front. Therefore, the pressure overshoot is smaller and hence, no overshoot is generated. Conversely, for very high fluxes the porous medium is already completely saturated also behind the tip, so no overshoot can occur even if the matric potential is positive (Fig. 5.9, right). (2) Saturation overshoot decreases quickly with increasing initial water content. (3) Saturation overshoot is much less for angular sand grains than for spherical sand grains.

A crucial question for understanding fingering flow is: On a physical level, why does the saturation overshoot occur (i.e., why is the tip saturation greater than the tail?) To answer this, we consider two quasi-equilibrium and rapid infiltration regimes from the microscopic perspective of water-interface illus-

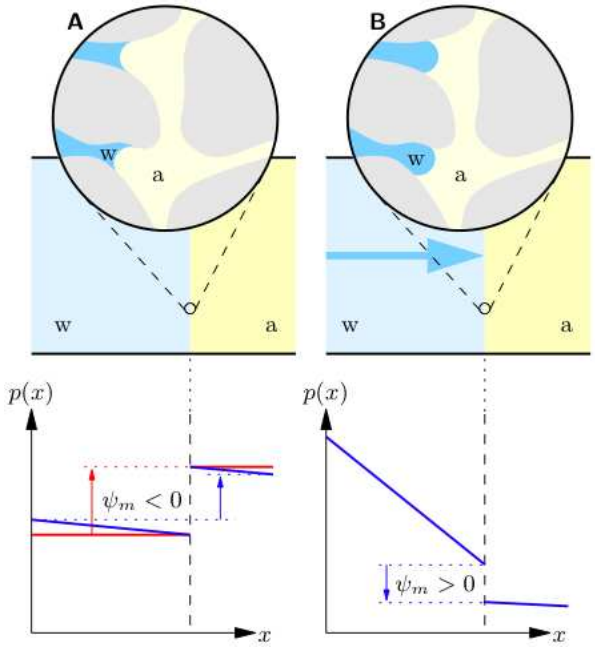

Figure 5.10.: Microscopic view of water-air interface (upper row) and pressure (lower row) for infiltration into an initially dry, water-wet medium with different fluxes: (left) static equilibrium (red lines) and low flux (blue lines) and (right) very high flux. Notice that the slope of $p(x)$ is related to the flux and to the viscosity of the fluid. Hence it is steeper for water than for air. (Figure 5.36 from Roth (2006))

trated in Figure 5.10. The below description is adapted from Roth (2006) (chapter 5).

"First consider the regime sketched in frame **A** of Figure 5.10. In static equilibrium, with the fluids at rest, the pressure is constant within both phases and discontinuous at their interfaces. The pressure jump, the matric potential $\psi_\mathrm{m} = p_\mathrm{w} - p_\mathrm{a}$ is determined by the mean curvature as described by the Young-Laplace equation (2.15). Slowly increasing the pressure gradient in the situation shown in Figure 5.10, at first only leads to a readjustment of the interface but not to a water flux: the interface is pinned. Further increase leads to a sudden jump of one of the interfaces across the large void and the subsequent rapid invasion of smaller pores ahead until the accumulated pressure is released.

With the gradient sufficiently high, many temporally overlapping jumps occur at different locations and give rise to a continuous flux. Increasing the gradient further will lead to a proportional increase of the flux as described by the Buckingham-Darcy law (Eq. 2.8).

Next, consider frame **B** of Figure 5.10 which represents a much higher water flux. The velocity here is so high that the water-air interface moves faster than the water-solid interface, despite the fact that water is the wetting fluid. As a consequence, the mean curvature of the water-air interface becomes positive. Hence, the very small value of the capillary number, pressure builds up in the water phase such that the matric potential ψ_m becomes positive. Notice that this is another instance where ψ_m does not reflect pore size and wettability alone, as is the case for static equilibrium, but that it contains a dynamic component. Notice that these two cases are fundamentally independent of each other. A common feature of all situations where a dynamic component of ψ_m becomes significant is that the relation between θ and ψ_m, as it is given by the soil-water characteristic, breaks down because the latter is a relation for static equilibrium. As a consequence, also Richards' equation breaks down since it is based on quasi-static equilibrium states".

We use this description to explain the saturation overshoot in flow fingers when water is rapidly infiltrated into a coarse dry sand. At the given velocity of water, capillary suction is too weak and the hydraulic conductivity in dry coarse textured sand is too low to remove the invading water. It piles up in the tip, thereby increasing the pressure gradient, until the sum of capillary and pressure gradient forces balance the invading force. At the invading front the mean curvature of the air-water interface may even become positive and hence, also ψ_m becomes positive. Despite the high velocity of water ($\approx 1\,\mathrm{mm\,s^{-1}}$) the capillary number of the air-water system, $\mathrm{Ca} = \eta v/\sigma$, is very low ($\approx 10^{-5}$) meaning that capillary forces still dominate viscous forces. The increased pressure leads to a higher water saturation, and consequently to the observed saturation overshoot in the finger tip.

Weitz *et al.* (1987) performed an ingenious experiment to reveal the dependence of ψ_m on velocity. They found that when an immiscible wetting fluid displaces an immiscible non-wetting fluid in a long tube of a porous medium through forced flow, the wetting angle is dependent on the forced velocity of the interface. They measured the dynamic pressure versus the local interface velocity for large range of velocities. They found that, depending on the flow velocity, the pressure jump across the interface, i.e., the matric potential ψ_m, was positive, zero, or negative, in accordance with the sketch in Figure 5.11.

Many approaches have been undertaken to explain saturation overshoot.

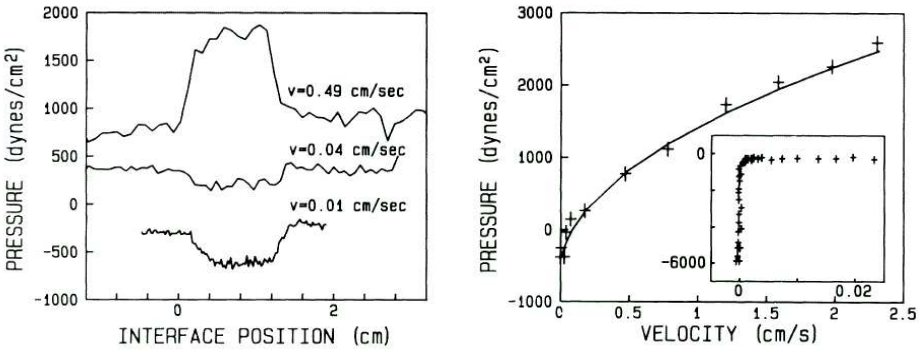

Figure 5.11.: **Left:** Measured pressure drop across the porous medium as a function of interface position for three different velocities. The pressure jumps as the interface moves through the porous medium, and reflects the magnitude of the pressure. **Right:** Pressure as a function of velocity. At low velocity, reflecting the fact that wetting properties cause the water to imbibe into the porous medium. However, at high velocity an additional driving pressure forces the interface through the porous medium. The dyne is the unit of force in the cgs system and equals 10^{-5} N. (Figure 1 and 2 from Weitz *et al.* (1987))

It has been shown that the overshoot cannot be described by the conventional Richards' equation. Recently, Eliassi and Glass (2001) have argued that Richards' equation with standard non-monotonic pressure saturation and relative permeability curves cannot produce solutions with saturation overshoot. Nevertheless, Eliassi and Glass (2002) considered three possible additional continuum terms to be added to the Richards' equation and from numerical simulations using one of them (Eliassi and Glass 2003) produced saturation patterns which qualitatively matched up with those seen in gravity. Glass and Yarrington (2003) considered a mechanistic approach based on forms of modified invasion percolation to simulate gravity-driven fingers using pore-scale modeling. DiCarlo (2004) also discussed how the measured saturation overshoot is inconsistent with a continuum description of porous media but qualitatively matches well observations and predictions from discrete pore-filling mechanisms.

The next question then arises: Why does the saturation, and presumably also the matric potential, decrease behind the tip? The additional pressure is

required to overcome the "entrance resistance" posed by the slow wetting of the wetting. Behind the tip, no such resistance is present anymore, the medium is already wet. The tip saturation is basically the minimum saturation available for a certain wetting front velocity and media. If this saturation is less than the tail saturation, the saturation increase will be continuous, but if it is greater than tail saturation, saturation overshoot will take place.

5.4. Dynamics of Water Saturation and Pressure

In this section we describe simultaneous measurements of the water saturation and water potential within fingers during the redistribution.

The dynamics of water saturation within the finger was analyzed at different locations during the passage through the cell. Figure 5.12 shows the temporal dynamics of water saturation for a small area inside the finger core at four fixed locations during the passage of the finger the tip at a temporal resolution of 2 minutes. Two distinct zones within the vertically elongated core area can be distinguished. At the tip, there is a zone with a water content near saturation (~ 0.8), followed by a drier zone, where the water saturation of the finger core decreased to ~ 0.5. We observed a minimum of water saturation within the finger core immediately behind the tip which would not be predicted by classical theory. With increasing from distance to the tip, the water content increases slightly to arrive at a steady state (the difference in water saturation is by the spatial heterogeneity of the small area selected inside the finger core at different depths). This clear experimental finding was not reported in previous works, however, it can be explained using standard theory. Behind the tip there is an lateral gradient which induces horizontal flow. This could be measured by monitoring a horizontal transect of water saturation at a fixed location during the passage of a finger (see Fig. 5.16). With increasing from distance to the tip this lateral flux decreases as will be discussed further in section 5.5. Since the water flux into the finger is constant the additional lateral flux component behind the tip reduces the vertical flow component and leads to a reduced water content according to the law of Buckingham-Darcy. The graph on top right in Fig. 5.12 shows the vertical water profiles produced from water distribution inside a finger at four different depths. Again, finger has a wet tip and drier tail during its traveling downward. Figure 5.13 shows the water saturation versus time for three small areas within a finger during the passage through the cell. The water saturation in area **1**, which exists inside the finger core, changes as described above with a saturated tip, a minimum

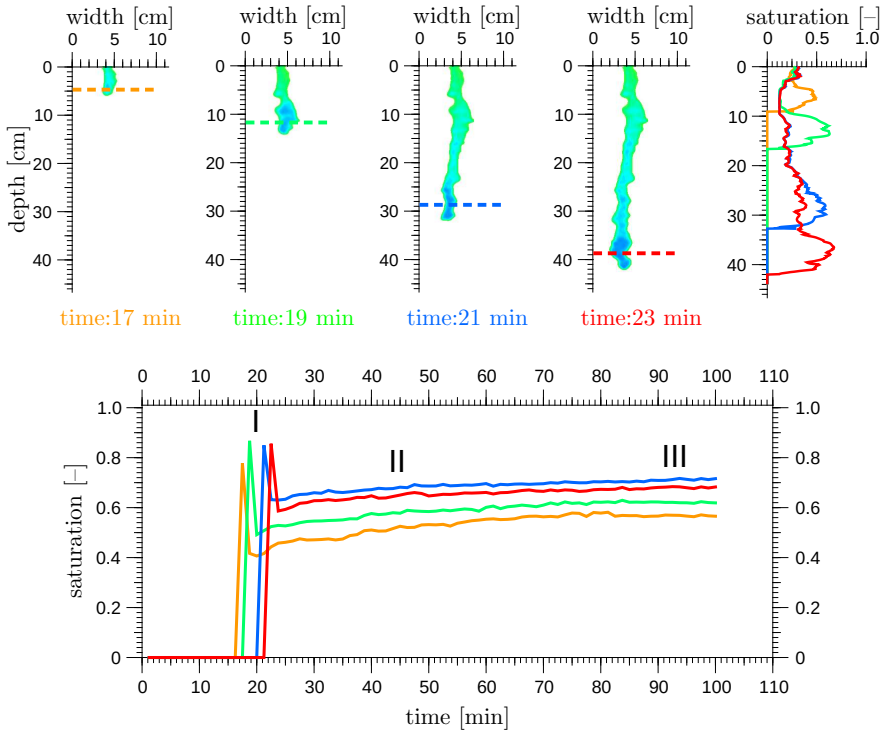

Figure 5.12.: The temporal dynamics of water saturation inside the finger core during the passage of a finger at four fixed depths at a temporal resolution of 2 minutes. In bottom graph, region **I** represents the period of rapid passage of the finger tip with a water content near saturation; region **II** is the finger tail portion with onset of a minimum value behind the tip followed by a slightly increasing; and region **III** represents the period in which water saturation becomes to a quasi-stable state. The depth profiles of the water saturation distribution in progressing finger at four different depths are shown on the graph top right. The difference in water saturation is by the spatial heterogeneity within the finger.

behind the tip and a slightly increase again towards a constant value at large distance from the tip. The area **2** exists inbetween the core and the fringe. Its saturation starts to change before stabilization of the finger core. After an increase in saturation, it decreases during lateral movement of moisture from the core to the fringe until finger is developed. The saturation in area **3**, which

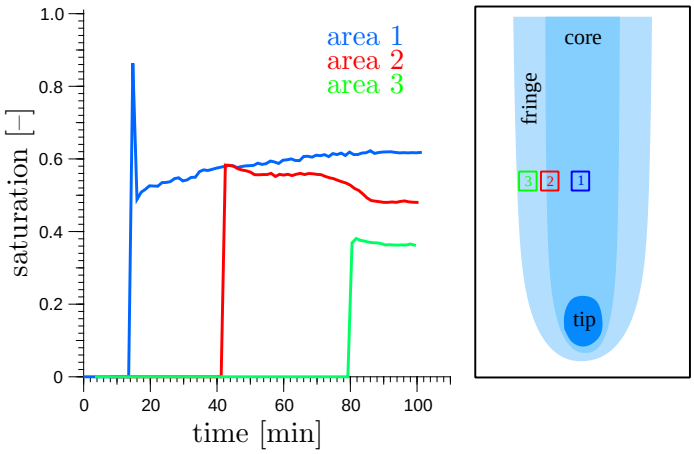

Figure 5.13.: Water saturation versus time within three small areas: 1) inside the core, 2) inbetween the core and the fringe, and 3) inside the fringe, at depth 10 cm for the finger shown in Fig. 5.12 during the passage through the cell.

exists inside the fringe region, changes when the moisture hits to this area. During lateral expansion of finger that is by suppling water from the core to the fringe zones of developed finger, the saturation inside this area does not change as this area plays as a gate between the core and fringes with uniform moisture content.

Many experimental runs were attempted to measure the water pressure using tensiometers. We measured the water potentials along many positions within the cell, but only few resulted in accurate tensiometer readings (no bubbles or leaks from any tensiometers). The largest problem for these measurements was that the finger trajectory was impossible to control and hence, the hitting of the fingers with tensiometers was uncertain. In our experiments, we measured water pressure behind the finger tip. Because of two reasons, we could not measure the water pressure in finger tip with saturation overshoot. First, with water pouring into the plastic tube of tensiometer, the dry sands, in front of sensor, would suck the moisture into the cell and the area around the sensor is wetted and herewith the saturation overshoot does not occur in pre-wetted sand. Second is that the suction head for water in initially dry sand is relatively high and hence, the finger tends to travel, to dry regions of sand and thus, the trajectory of the finger changes. Therefore, tensiometers were saturated when

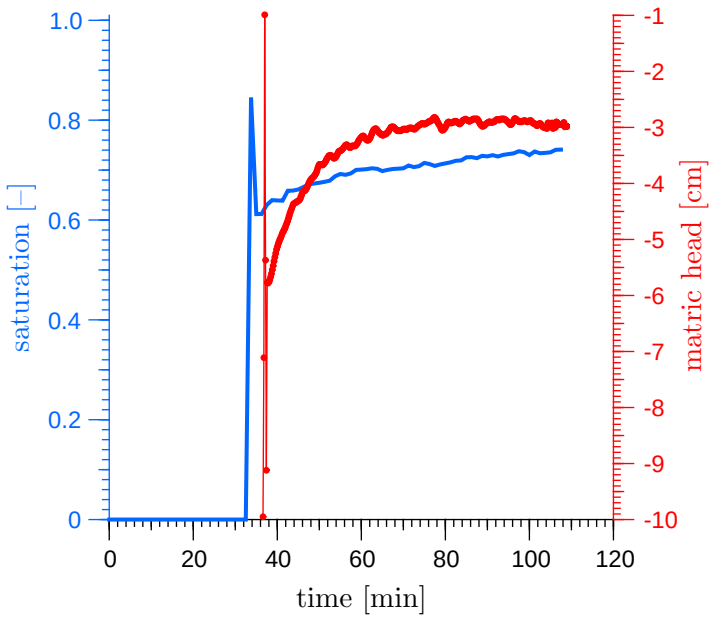

Figure 5.14.: Plot of a simultaneous measurement of water saturation inside a finger core from initial finger tip and water potential inside the core after the initial finger tip passed through the tensiometer position at 50 cm depth below the sand surface. The jump in the pressure results at the start of measurements for a short time, which is the reaction time of the tensiometer, was for tensiometer reading reached equilibrium.

the finger tip passed from the position that tensiometers were placed.

Figure 5.14 gives the results of water saturation versus time inside a finger core from initial finger tip and a simultaneous measurement of matric head (h)[a] inside the core after the initial finger tip passed through the tensiometer position. Upon hitting the tensiometer with the water finger with inserting the transducer into the tensiometer tube, after the passage of the finger tip, the tensiometers momentarily came up from the extreme negative matric head value of the air dry sand (we measured over -50 cm) to a value of approximately ~ -6 cm. This jump was during a short time which is the reaction time of

[a]In soil physics, often the matric potential is expressed in terms of "matric head" ($h = \psi_m/\rho g$). The idea is that h can be interpreted as equivalent height of a water column; negative values correspond to a hanging column.

the tensiometer where the pressure quickly increases to about -1 cm and after ~ 1 minute (reaction time), the tensiometer reading reached equilibrium. After this increase, the matric head slightly increased due to the horizontal widening of the finger and at the same time, water saturation was increasing slightly. At a large distance behind the tip, the matric head came to an equilibrium state of $-3\,\mathrm{cm}$ (at time about 90 minutes). These differences in moisture content inside the tip, core, and fringe zones can be explained simply in terms of hysteresis in the pressure-saturation curve, as the finger cores are on the drying branch of the pressure-saturation curve and thus hold much more water at equal pressure than outside the fingers, where the sand is on the wetting branch. Our experimental data offer a good opportunity to examine this further. This is detailed in below section.

5.4.1. Dynamics and stabilization of the fingers

One of the crucial ingredients for understanding the mechanism of fingered flow is the hydraulic state $(\theta, \psi_\mathrm{m})$ during the passage of the finger tip governed by the hysteretic soil-water characteristic as sketched in Fig. 5.15. This figure shows the hysteretic behaviors of moisture conditions in the finger core and the surrounding finger-fringe zone. We consider three locations: x_0 on the centerline of the core, x_1 at the outer limit of the core, and x_2 at the outer limit of the fringe. Initially, the sand is dry hence ψ_m is strongly negative and θ very small. As the finger moves downward and with the tip approaching x_0, both θ and ψ_m increase rapidly and move below the static wetting branch state of the soil-water characteristic until they reach the maximal values θ^tip and $\psi_\mathrm{m}^\mathrm{tip}$, respectively, with the center of the tip passing over x_0. This is a non-equilibrium process. Note, that during this highly dynamic process ψ_m in the finger tip does not reflect the pore-size or the contact angle and the values of θ^tip and $\psi_\mathrm{m}^\mathrm{tip}$ are not located on the static soil-water characteristic (as implied by Fig. 5.15 for simplification). This is also the reason why the observed overshoot cannot be reproduced by Richards' equation which relies on a static $\theta(\psi)$ relation.

After the passage of the finger tip, the water content drops immediately behind the tip to a minimum value for a very short time and brings the hydraulic state on a point above the static curve $(\theta{<}\theta^\mathrm{core}, \psi_\mathrm{m}^{\mathrm{core}'})$. As it cannot stay outside the static state, it has to back to an equilibrium state. Hence, the water content increases at x_0 which brings the hydraulic state on the desorption branch of the soil-water characteristic. After the tip passes, the material is wet and no additional force for pushing the phase boundary through the porous

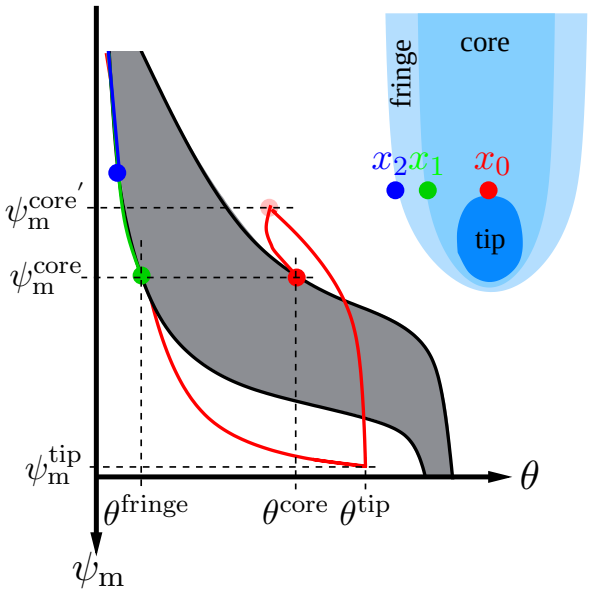

Figure 5.15.: Sketch of the evolution of hydraulic states during the passage of a finger: at location x_0, where the center of the tip passes through, (θ, ψ_m) moves from the initial very dry state to the maximum $(\theta^{tip}, \psi_m^{tip})$ along the wetting branch of the water characteristic and then, behind the tip, towards $(\theta^{core}, \psi_m^{core})$ along the drying branch with an immediately drop to a minimum value for a very short time. During the same time, the state at x_1 evolves monotonically towards $(\theta^{fringe}, \psi_m^{core})$. As the states at x_0 and x_1 approach the same potential ψ_m^{core} on different hysteresis loops, the radial water flux ceases even though the water contents are quite different. This prevents further rapid radial growth of the finger and stabilizes it. The gradient between x_1 and x_2 causes only minor water flux because of the low hydraulic conductivity and by the limited supply of water. The gray area represents the main wetting and drying boundaries at equilibrium state of the soil-water characteristic curve.

medium is required anymore. At this point, water infiltrates radially, driven by the large hydraulic gradient. Thereby, (θ, ψ_m) approaches the metastable state $(\theta^{core}, \psi_m^{core})$, whose time-scale for change is very much longer than the one for reaching it. During the same time of approaching to the metastable

state, the state at location x_1 evolves monotonically along the wetting branch towards $(\theta^{\text{fringe}}, \psi_{\text{m}}^{\text{core}})$. With the matric potential at x_0 and x_1 approaching the same value, $\psi_{\text{m}}^{\text{core}}$, the radial gradient decreases and with it the corresponding flux, and hence, the finger becomes stabilized.

On a time-scale that is much longer than that of the finger's creation, it continues to expand. This is caused by the large radial gradient in the fringe of the finger, between x_1 and x_2. However, with the water content already low at x_1 and further decreasing in the fringe, hydraulic conductivity decreases very rapidly and with it the radial flux.

This hysteretic behavior on the soil-water characteristic curve describes the mechanism of the development of a saturated finger tip, and the subsequent drainage behind the tip. Since the finger core is initially wetter than the fringe region, its hydraulic conductivity is higher than the fringe zone. Thus, tip, core and fringe regions having essentially different water characteristic curves. The tip and the fringes of the finger are on a wetting curve, while the remaining core of the finger is on a drying branch.

5.5. Finger Width

Based on Hele-Shaw cell experiments, many scientists have studied the theory of wetting front instability to describe and predict the finger width in homogeneous soils (e.g., Raats (1973), Philip (1975a;b), Parlange and Hill (1976a), Diment *et al.* (1982), Hillel and Baker (1988), Glass *et al.* (1989a;c)) and verified their predictions experimentally (e.g., Baker and Hillel (1990), Liu *et al.* (1994b), Bauters *et al.* (1998)). A long-term lateral spreading of the fingers emplaced in dry media has also been widely observed. Glass *et al.* (1989c), Glass and Nicholl (1996) and DiCarlo *et al.* (1999), for example, showed that water flow continuing for tens or hundreds of hours results in large lateral expansion of the fingers. DiCarlo *et al.* (1999) noted that the lateral expansion of the fingers was linearly related to the square root of time. They suggested that the lateral spreading was mainly due to vapor diffusion, and presented an analysis which appeared to show a correspondence between the lateral growth of water wetted area, and the expected rate of vapor transport between a saturated to dry division.

In our experiments, as expected in the initially dry sand, the finger pattern began to widen immediately after infiltration. We observed that during downward movement of a finger under continuous infiltration, the width increases with time. We found a gradual change in the water saturation across

boundaries between the finger core and the finger-fringe zone. According to the core and fringe regions development having essentially different moisture characteristic curves, the finger width growths can be classified into two lateral expansion stages:

Stage I: **Core Stabilization:** A fast expansion of the finger width to stabilization of the finger core that conducts most of the flow by effects of infiltrating forces on a short time scale. In this stage, water infiltrates radially driven by the large hydraulic gradient between the center of the finger core and the outer limit of the core. The radial gradient decreases over time and with it the corresponding flux, approaching the center and the outer limit of the finger core to the same pressure. This stage of the development can be described by hysteretic behavior on soil-water characteristic curve where the tip is on a wetting branch and the core behind the tip on a drying branch. The radial water flux ceases when core and the outer limit of the core approach the same potential on different hysteresis loops, and hence, the finger core becomes stabilized.

Stage II: **Fringe Expansion:** A slow expansion associated with growth by effects of capillary forces and hydraulic gradient between the outer limit of the core and fringe zone on a time scale much longer than core stabilization. This low hydraulic gradient decreases the hydraulic conductivity very rapidly and with it the radial flux. In this stage, water flows vertically in the stabilized core and laterally in the fringe zone which means that wetting fronts leave the fingers and move laterally into the dry sand on either side of the finger core areas. Over time, slow lateral movement of moisture from finger core regions creates a less saturated surrounding fringe region and the finger continues to expand.

A time series of intensity measurements of a lateral cross-section at a fixed location during the passage of a finger is shown in Fig. 5.16 (**a**), which shows a maximum in the center of the finger (core areas) and slow water lateral movement from core regions to the less saturated surrounding resulting in significant lateral expansion. This plot illustrates the dynamics of water saturation within a finger from the initially saturated finger tip to a quasi-stable state. The width of the finger is stabilized after some 75 minutes (stage I). This corresponds to the time to arrive at approximately constant water contents within the finger core as shown in (Fig. 5.16, blue curve in the plot **c**).

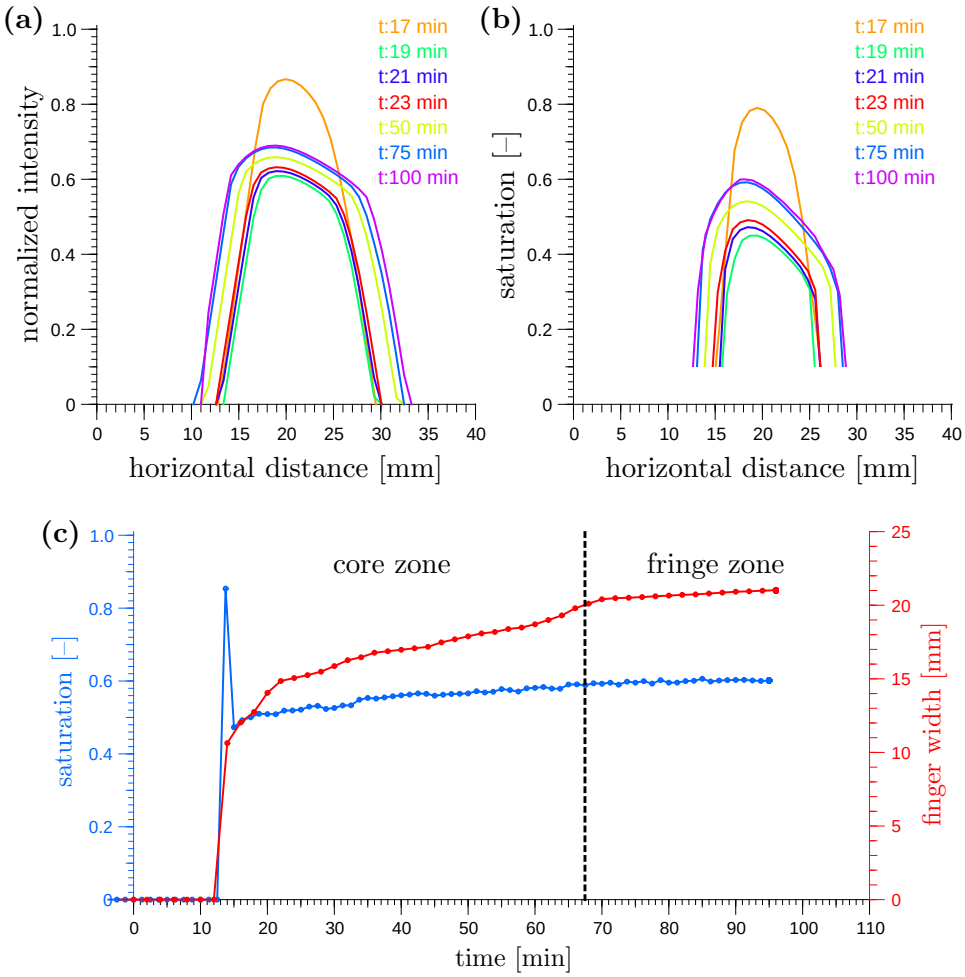

Figure 5.16.: **a)** Horizontal transverse intensity profiles at a fixed location for different times during the passage of a finger in an experiment with constant flux infiltration of $1.2\,\mathrm{mm\,min^{-1}}$ showing the dynamics of water saturation within a finger from the initial finger tip to a quasi-stable state. **b)** The same horizontal transverse profiles for water saturation calculated by the calibration equation (Eq. 3.7) between normalized intensity and water saturation. As described in section 3.3, due to the fundamental problems, the calibration is valid only when the normalized intensity is between 0.47 and 1.0 with water saturation between 0.1 and 1.0. **c)** Water saturation changes inside the finger core (blue dots) and measured optical width for a finger (red dots) using horizontal transverse intensity profiles as a function of time during the passage of a finger at the same fixed location of top plots. The time numbers refer to the time after starting of water infiltration.

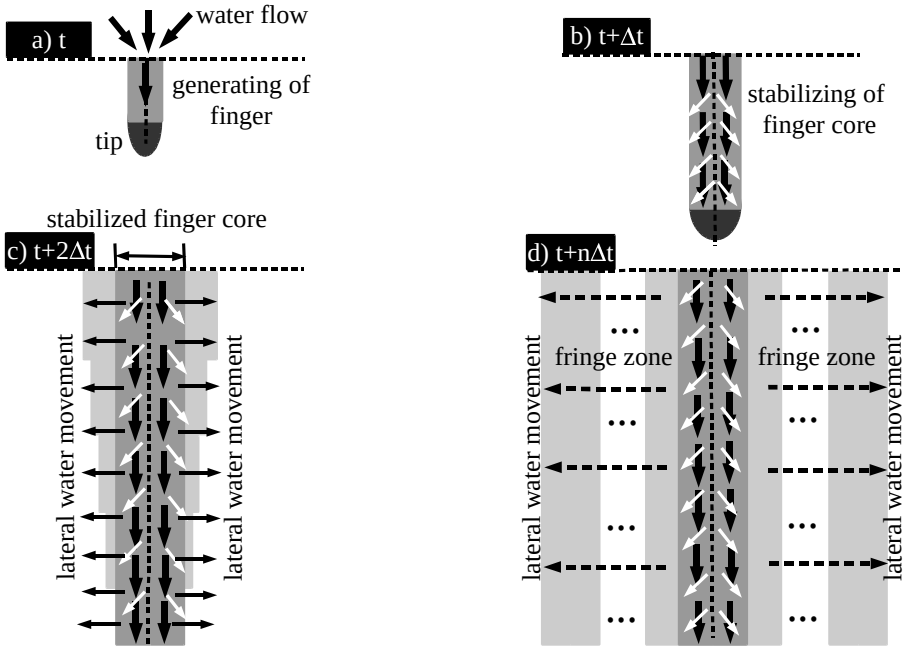

Figure 5.17.: Schematic diagrams of core and fringe development of a single finger during downward growth with lateral water movement from the core to the fringe zone. After the passage of the finger tip and the stabilization of the finger core (stage I), the finger starts to grow radially (stage II).

Figure 5.16 (**b**) shows the same horizontal transverse profiles for water saturation calculated by the calibration equation (Eq. 3.7) between normalized intensity and water saturation. As described in section 3.3, due to the fundamental problems, the calibration is valid only when the normalized intensity is between 0.47 and 1.0.

We measured the optical width of a finger by calculating the difference between points corresponding to half the maximum intensity of the horizontal transverse intensity profiles (Fig. 5.16, red curve in the plot **c**). These measurements show that the finger width increases from 11 mm after the passage of the finger tip to 21 mm after 100 min of continuous constant infiltration. The measurements of the finger width using the horizontal transverse saturation profiles lead to narrower widths in comparison with intensity profiles.

Figure 5.17 is a schematic drawing of the finger development showing the

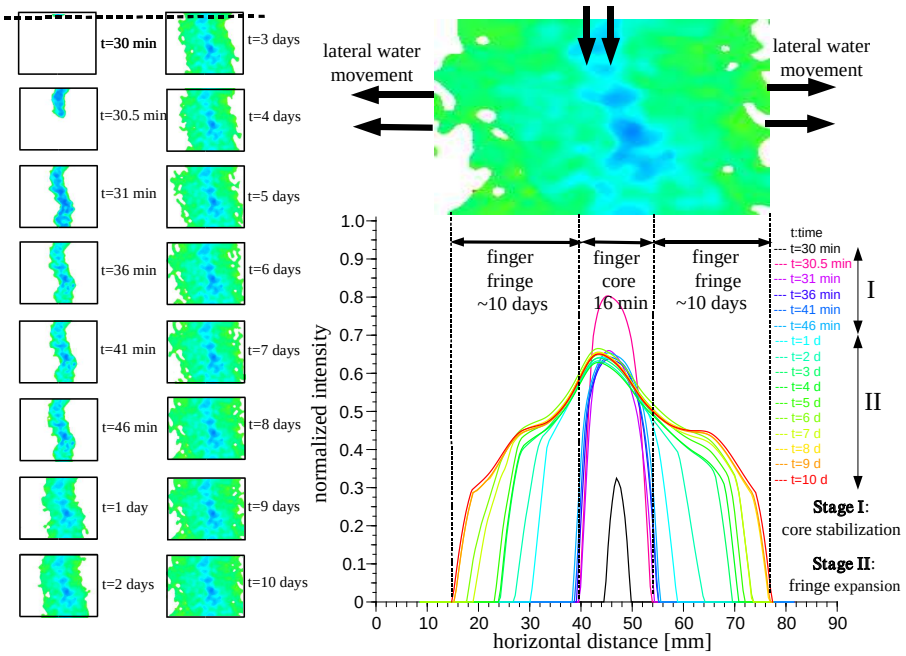

Figure 5.18.: Sixteen different times series visualizing the finger core and fringe areas development and the lateral cross-section intensity profiles of a finger at a fixed location (indicated by black dash line in images top left) during the passage for the duration of 10 days continuous infiltration. Over time, slow lateral movement of moisture from finger core regions creates a less saturated surrounding fringe region and finger continues to expand. The width of the fingers increases from 11 mm after the passage of tip to 60 mm after 10 days continuous infiltration.

downward growth followed by two stages I and II of lateral growth into the core and fringe areas, respectively. Progressive growth of a finger can be divided into following steps: In step 1, a finger is generated (Fig. 5.17a). In step 2, it moves downward and the finger core is stabilizing (Fig. 5.17b). In step 3, water flows vertically in the stabilized core and laterally in the fringe zone (Fig. 5.17c). After several steps, the finger grows with lateral expansion for a long time (Fig. 5.17d).

If the water flow continues for a long period of time, lateral water movement leads to significant lateral expansion of the fingers. Fig. 5.18 illustrates the

development of the finger core and fringe areas in time, for an experiment with the duration of the 10 days of continuous infiltration with a constant flux of $1.2\,\mathrm{mm\,min^{-1}}$. These intensity measurements show that the finger core stabilized 16 minutes after the tip wetting front passed (stage I) and the lateral movement in the fringe zones continues to expand for a long time after stabilization of the core (stage II). As long as there is a radial hydraulic gradient between the outer limit of core and fringe zones, it continues to expand. This is an example showing that the growth of the fingers is a very slow process. Hence, the wetting and drying to equilibrium inside the finger core took place in less than an hour, while the wetting to equilibrium outside the fingers took place over several days.

5.6. Finger Tip Velocity

In a quantitative analysis, the finger tip velocity was defined as the rate of change in position of the leading edge of the tip. Finger tip velocity is expected to be a function of the gravity gradient, capillary gradient, media heterogeneity, applied flux, initial moisture content and number of the fingers. As the finger tip advances, the small-scale heterogeneity in the sand layers acts to continuously alter the shape of the wetting front. These fluctuations in wetting front structure are affected by dynamic variation in the capillary gradient, and result in velocity variations. On the other hand, when a new finger is initiated the flux in the existing fingers decrease and the loss of flow is expected to slow the fingers. The fingers, during flowing in the Hele-Shaw cell, have very sensitive distribution and their movement is not continuous. Because the change of the wetting front shape and loss of fluid are coupled dynamic processes the actual behavior is quite complex.

The images shown in Figure 5.19a are the finger advancements of an experiment with constant flux infiltration of $j_\mathrm{w} = 1.2\,\mathrm{mm\,min^{-1}}$. In this experiment, the cell was filled without heterogeneous layer to calculate the tip velocity during the passage of the fingers for a long depth (150 cm) through the cell. The dynamic change of the local finger tip velocity of these four fingers is shown in Figure 5.19b. The velocity of the fingers shows a large local variation at early times and a more smoothly gradual trend toward deceleration over the time. These large variations at early times arise from initiation of new fingers in the interface between the fine and the coarse layer, during that time with constant infiltration and uniform suppling of water from top fine layer. Both deceleration and local tip velocity fluctuations are apparent in Figure 5.19b.

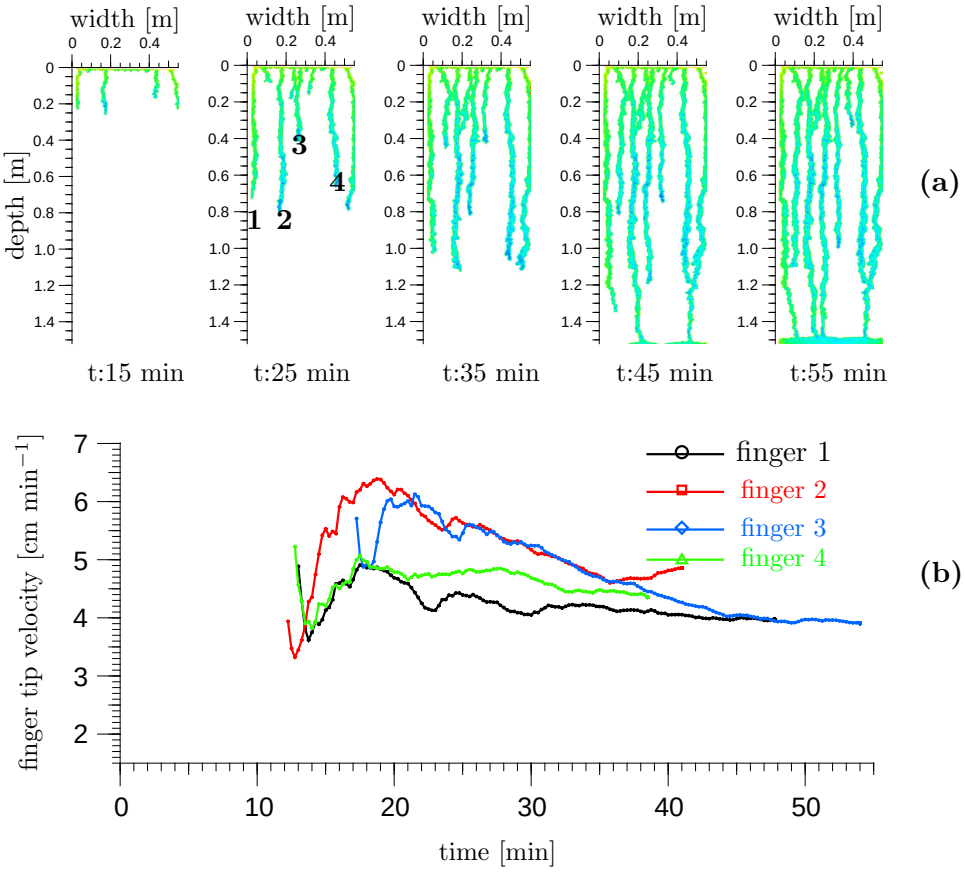

Figure 5.19.: **a**) Images illustrating the advancement of the fingers into the cell for an experiment with constant infiltration of $j_w = 1.2\,\mathrm{mm\,min^{-1}}$. The indexed time below the images is the real time after starting of infiltration. **b**) Finger tip velocity variation as a function of time for four fingers.

The velocity measurements collected from the two significant fingers of an experiment with constant flux of $j_w = 1.2\,\mathrm{mm\,min^{-1}}$ are presented in Fig 5.20. For two major fingers, the velocity of their tips are in general not constant and they are anti-correlated. The dashed line labeled finger 1 corresponds to the right-hand finger and the solid line labeled finger 2 to the left-hand finger. The temporal distribution of the images corresponds to the time scale along the bottom of the images. Measurements made at early times ($t < 12\,\mathrm{min}$) show

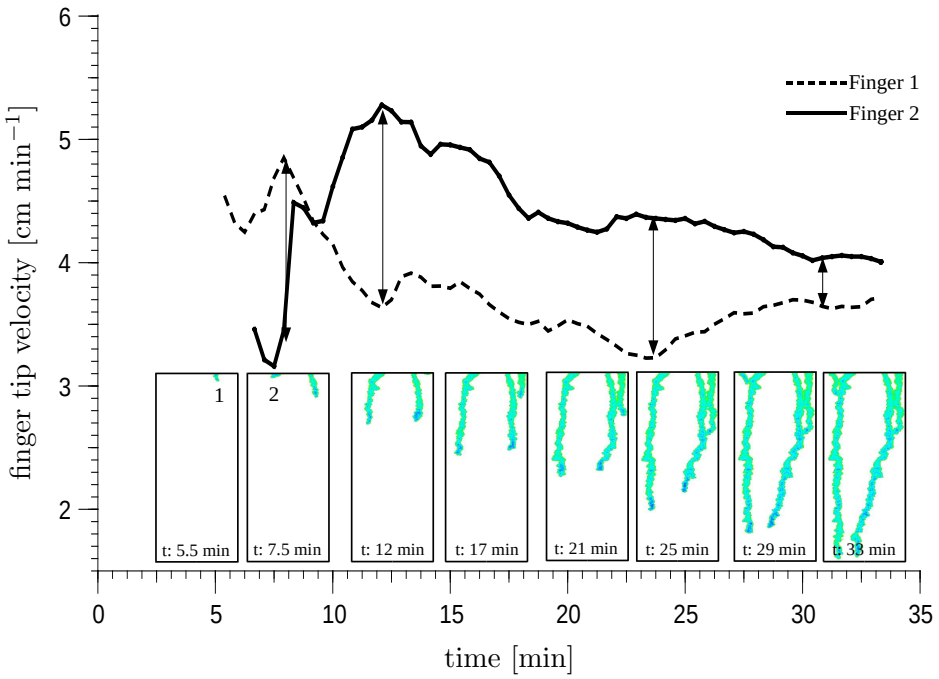

Figure 5.20.: Finger tip velocity for two major fingers as a function of time for an experiment with constant flow rate infiltration $j_w = 1.2\,\mathrm{mm\,min^{-1}}$. The velocities of their tips are anti-correlated and the two fingers remained in hydraulic communication during the passage of the fingers.

a high degree of variability and on average when finger 1 accelerates, finger 2 decelerates. These two fingers are in hydraulic communication and gradient changes in one finger will affect the other. At approximately $t = 12\,\mathrm{min}$, hydraulic communication between the fingers is broken, and a second flow regime begins when a third finger initiates into the cell. In this case, the velocity profile appears to be much smoother, showing some variation of a distinct trend toward deceleration. At $t = 23\,\mathrm{min}$, the velocity of finger 1 increases, because at that time this finger is merged with a new finger generated in the left side of the cell.

5.7. Fingering Flow under Different Flux Rate Infiltration

A series of water infiltration experiments was conducted in six separate Hele-Shaw cells filled with initially dry sand using six different fluxes through upper boundary thus varying from 0.6 to 19.2 mm min^{-1}. All experiments were run for 5 hours and images were recorded with an interval time of 1 minute. The purpose of these experiments were to quantify the effects of infiltration rate on flow instability and to compare the redistribution of flow fingers for different infiltration rates. Based on the experimental results, we present the effect of the flow rate on the behavior of the finger width development, velocity, water content, and number of the fingers that form. Figure A.3 illustrates sequence of digital images for these experiments. All infiltration flow rates between 0.6 and 19.2 mm min^{-1} produced wetting front instabilities that generated many fingers during redistribution through the cell.

Table 5.1 presents the results of final number of the fingers, average width, average tip velocity, average saturation inside the core, and the percent total area of the cell occupied by fingers for these series of experiments.

Applied flow rate [mm min^{-1}]	Final number of fingers			Average width±STD[a] [cm]	% of cell occupied by fingers	Average velocity ±STD [cm min^{-1}]	Average saturation ±STD [–]
	T[b]	M[c]	B[d]				
0.6	4	4	4	2.15±0.15	35±2.05	3.09±0.68	0.60 ±0.05
1.2	4	4	3	2.75±0.21	44±2.14	5.41±0.95	0.65±0.05
2.4	4	5	4	3.56±0.41	49±2.16	8.12±1.16	0.73±0.06
4.8	8	8	8	3.81±0.49	70±2.62	10.83±1.23	0.78±0.06
9.6	12	11	11	4.05±0.50	88±3.13	13.12±1.86	0.82±0.07
19.2	16	15	15	4.27±0.68	91±3.21	16.25±2.04	0.87±0.07

[a] Standard deviation
[b] Top cross-section
[c] Middle cross-section
[d] Bottom cross-section

Table 5.1.: The final number of the fingers, average fingers width, average fingers tip velocity, average saturation inside the core and percent total area of the cell occupied by fingers for a series of experiments with different flow rates.

Figure 5.21 illustrates the number of the fingers as a function of flow rate through upper boundary for three different times during passage from three cross-sections (top, middle, bottom) of the cell. From a qualitative point of view, from these plots and from sequence images presented in Fig. A.3, the total

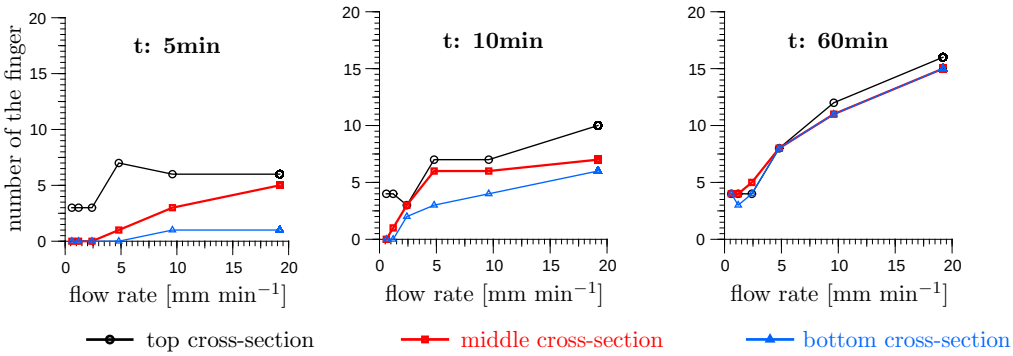

Figure 5.21.: The number of the fingers as a function of flow rate for three different times (5, 10, and 60 minutes) after initiation of the fingers during water infiltration through the cell. The number of the fingers was counted in three different cross-sections at depths of 0.3, 0.8, and 1.3 m of the cell.

number of the fingers increases as flux increases. For all applied fluxes, counted number of the fingers decreased following passage of the fingers over depth during downward movement from three cross-sections as shown in Fig. 5.21. This is because some fingers do not carry enough water to keep downward growing and they merge together for further movement and thus the number of the fingers reduces with depth. For an individual flux, the total number of the fingers increases over the time. The amount of water flux applied through the system is constant through the top layer which controls the infiltrating flow. The total flux at z component ($q_{\mathrm{w,z}}$) is divided into N number of the fingers, hence

$$q_{\mathrm{w,z}} = \sum_{i=1}^{n} N_i \, j^i_{\mathrm{w,z}} \tag{5.1}$$

where $j^i_{\mathrm{w,z}}$ is the water flux within the generated finger i. We observed that when the initial fingers reached to bottom of the cell, some new fingers start to initiate. When the wetting fronts find ways to penetrate interface between the fine and the coarse layer, the flux into other fingers decreases and according to Eq. 5.1, the number of the fingers has to increase to sustain the constant flux $q_{\mathrm{w,z}}$. Figure 5.22, presents the plots of measured values for average finger width, tip velocity, saturation inside the core and total area occupied by fingers as a function of flow rate. Top left plot, shows that percentage of cell occupied by fingers increases linearly with flux. This linear relation between the occupied

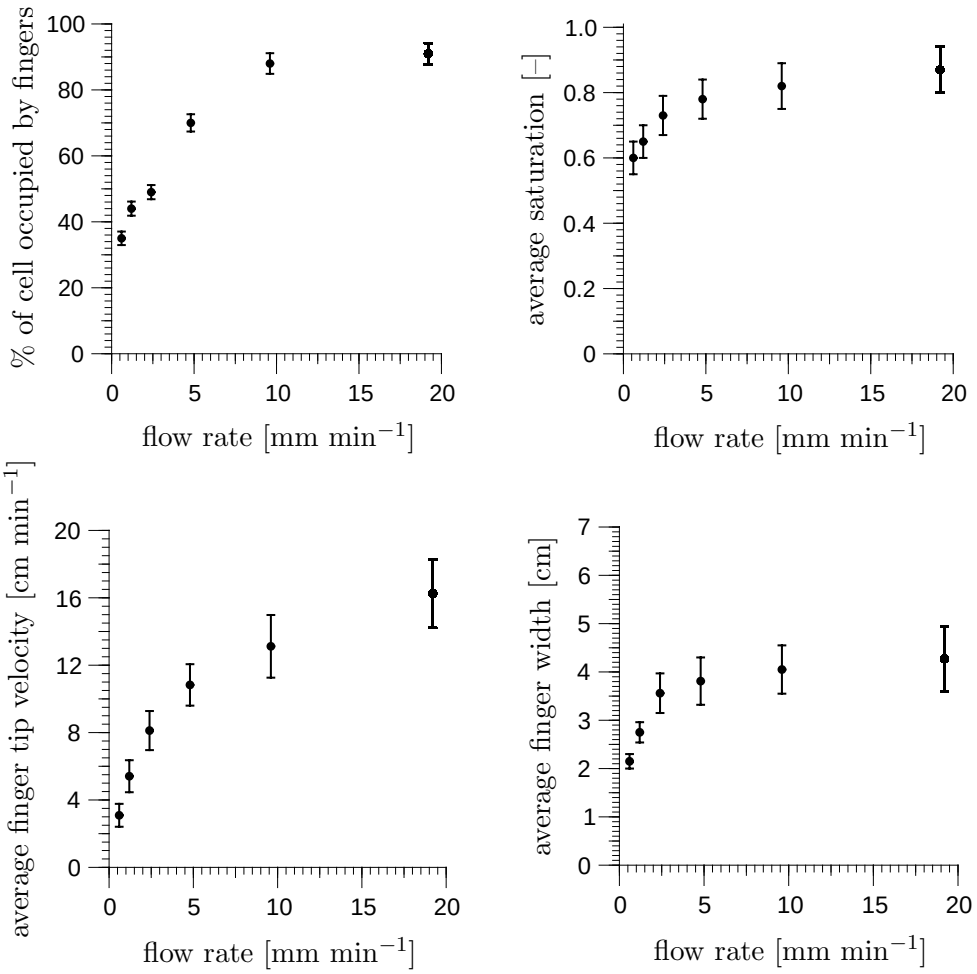

Figure 5.22.: Plots of average finger width, average tip velocity, average saturation inside the core, and percent of cells occupied by fingers as a function of flow rate through upper boundary.

area and the flow through the system, suggests that an increase in flow rate through the system increases the fraction of the cell occupied by fingers. The non-linearity shape at high flux (19.2 mm min^{-1}) is because there was no more space to development of the fingers in the cell. The average saturation inside the core shown in Fig. 5.22, top right, increases rapidly at low flux, the slope off and approach to near saturation, which shows to be near the porosity, at high

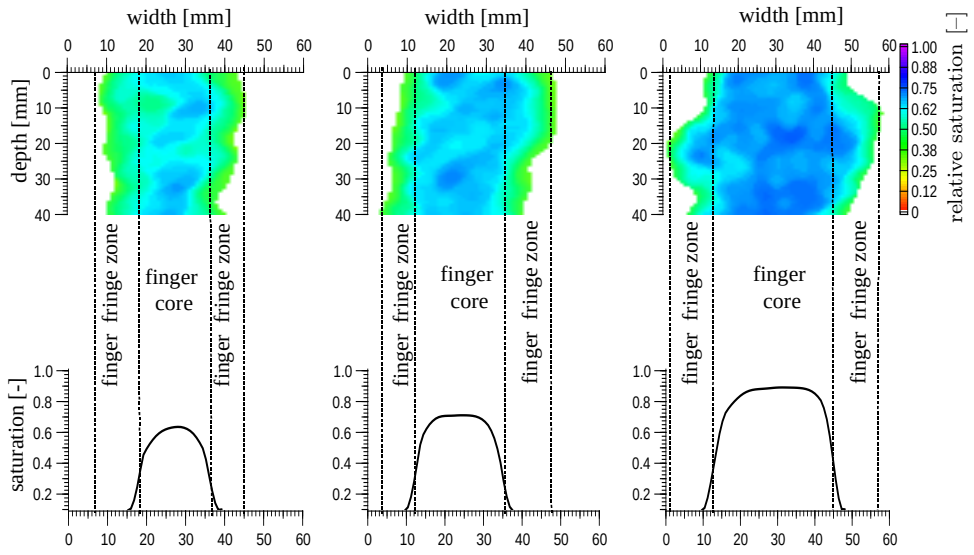

j_w=0.6 mm min^{-1} j_w=4.8 mm min^{-1} j_w=19.2 mm min^{-1}

Figure 5.23.: Typical example of three horizontal water profiles for three fingers generated at three different flow rates infiltration. Higher flux shows the wider core with more saturation within the fingers.

flow rate. The experimental results indicate that finger velocity at low flow rate was slow and very fast at high flow rates. The slope of the finger velocity versus flux steadily decreases with increasing flux as shown in Fig. 5.22, bottom left. The average width versus flux is shown in Fig. 5.22, bottom right. Generally, the slope of the measured width as a function of flow rate becomes less as the applied flux increases.

Water saturation measured within the finger core was found to be an increasing function of applied flux. Figure 5.23 is a plot showing the structure of the finger width and horizontal transverse saturation profile for three fingers at three fluxes (low, intermediate, and high) at the end of the experiment. These cross-section profiles of water saturation measurements clearly show the non-uniform saturation profiles within the fingers and illustrates that the saturation in the finger tail is controlled by the applied flux, where the finger width and saturation inside the finger core are higher when the flux is higher.

The width growing of six arbitrary fingers obtained from horizontal transverse saturation profiles for six different forcing flow rates are presented in

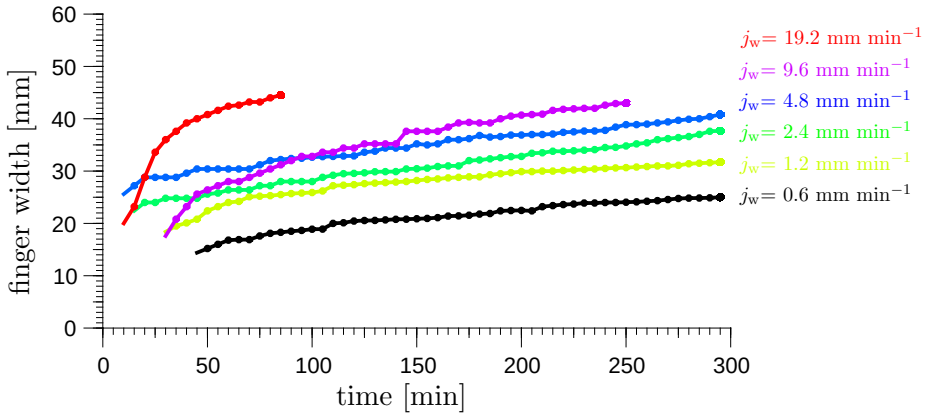

Figure 5.24.: The width of six growing fingers as a function of time, for six different forcing flow rates measured using the horizontal transverse saturation profile.

Fig. 5.24. It shows that the finger width tends to increase with time and increasing the flux influences on width expansion and under all applied flux it continues to increase slowly for a long time. Because of large number of the fingers at high flow rate infiltration, the width of the fingers was possible to measure only before filling the cell by water moistures.

Thus, unstable phenomena are very sensitive to initial and boundary conditions and the flow rate appears to play an important role in width, velocity, saturation and number of the fingers and referring to these results, the increasing of flow rates leads to increasing finger width, number, velocity and the saturation inside the core.

5.8. Finger Persistence

Glass *et al.* (1989c) studied the finger persistence over a long periods of time. They showed the persistence of fingered flow structure upon a subsequent infiltration event after the full development of the two regions core-fringe flow field. Wang *et al.* (2003) have shown in their experiments that the porous medium retained a memory of the fingers formed in the first experiment, so fingers formed in subsequent redistribution cycles followed the old finger paths, even after 28 days had elapsed.

In this study, another experiment was performed to determine the persistence of fingered flow paths and structure of core and fringe for infiltration after an extensive period of time. Experiment was conducted with onset of a constant water infiltration ($1.2\,\mathrm{mm\,min^{-1}}$) and when the fingers reached the bottom of the cell, the infiltration was stopped. Five days after, it was restarted using dye tracer infiltration at the same flow rate.

Figure 5.25 shows the illustration of the growth and persistence of fingered flow paths. At the start of the experiment, fingers formed and reached the bottom of the cell during the first water application period. Following the cessation of water application, the water profile inside the cell changed much more slowly and fingers were drained. Five days after the water flow in the experiment was stopped, the fingers had steadily grown to fill the entire cell and the initial moisture content field appeared almost uniform to the eye. During the five days cessation of infiltration, water in the finger domains gradually expanded into the surrounding profile by the mechanism described in section 5.4.1. However, upon reinfiltration using dye, the flow still tended to flow preferentially down along the previously formed finger pathways and core structure in the fingers again reappeared. The locations of the core regions as highlighted by the blue pulses were almost the same as in the first water infiltration cycle.

The question then arises: Why does the persistence in flow fingers occur? By analyzing the horizontal distribution of water saturation within and around the fingers, we found the water content in center of the finger is higher than fringe area even after 5 days of no inflow (Fig. 5.25, bottom graph). After stopping the infiltration, the water content within the core decreased slowly. The horizontal saturation profiles did not reach to a steady state after 5 days. In the first day after cessation of water infiltration, the saturation distribution area in the fringes (lateral movement) was more than expected according to decreased amount of water in core. This can be explained by the fact that the distribution of water in the fine toplayer and cores were very slow to reach a quasi-equilibrium state. After first day, the decreased amount of water within the core was consistent with distribution area in fringes. Thus, core and fringe regions have essentially different moisture characteristic curves. The core area is preserved as a relatively wetter zone than fringe areas and until the water potential at the fringe is approximately smaller than the core, lateral expansion will continue.

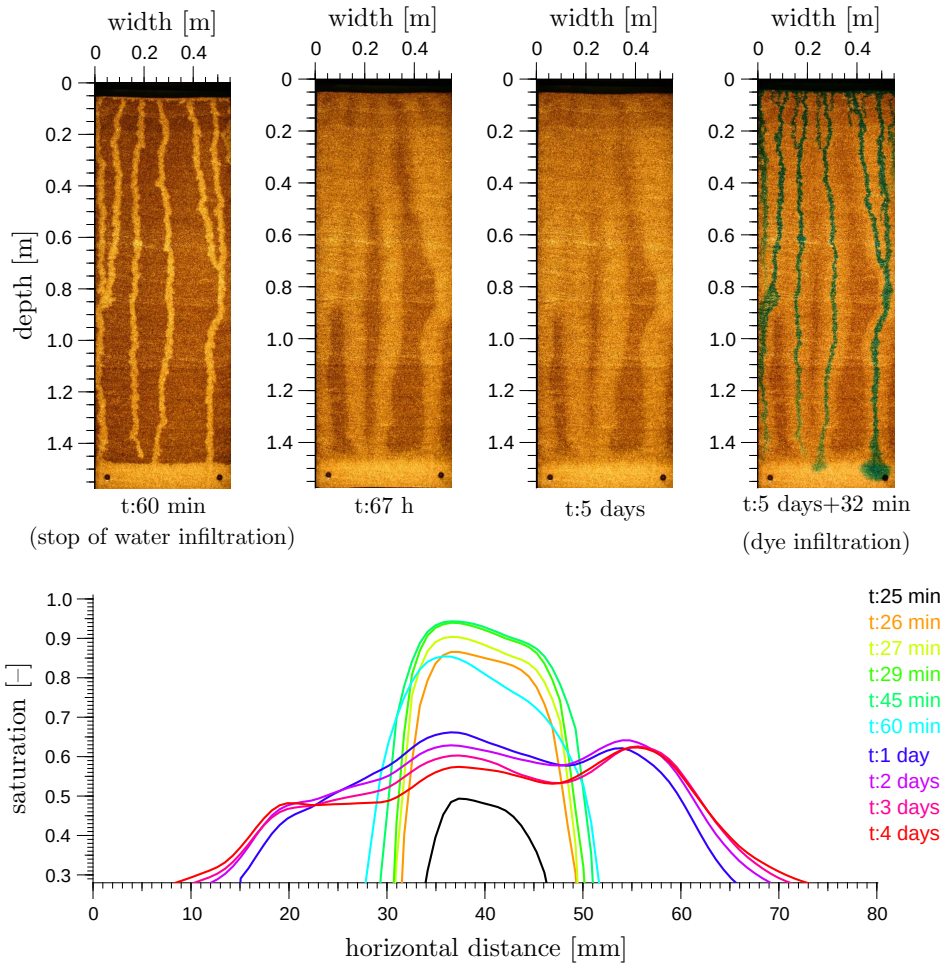

Figure 5.25.: A sequence of photographs of an experiment demonstrating finger persistence. It represents the distribution of water content in the Hele-Shaw cell during an event in which water was applied for 60 min, then stopped for 5 days, and then dye tracer applied for 32 min. The image of the moisture content field before second cycle ($t = 5$ days) showed that the variation in initial moisture content was very small and uniform. The subsequent dye infiltration events demonstrates the persistence of the core-fringe region structure during the rapid growth of dye fingers. The bottom graph shows the horizontal transverse saturation distribution at a fixed location for different times during passage of a finger and after cessation of infiltrating water. When infiltration is stopped, the amount of water within the cores is distributed into the fringes. The time numbers refer to the time after starting of water infiltration.

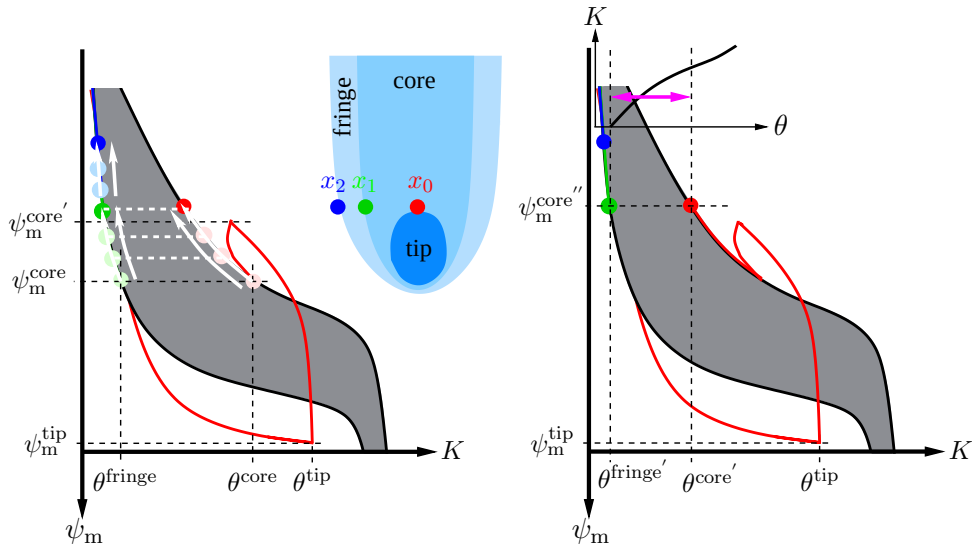

Figure 5.26.: Finger persistence demonstration using the evolution of hydraulic states of a finger described in Fig. 5.15. After cessation of the infiltrating water to the finger, the water content and matric potential at location x_0 move from $(\theta^{core}, \psi_m^{core})$ to $(\theta^{core'}, \psi_m^{core''})$ along the main or adjacent drying branch because of the slow draining process following the interruption of flow. During the same time, the state at x_1, evolves towards $(\theta^{fringe'}, \psi_m^{core''})$. The state at x_2 also decreases with limited supply of water from the core. At these new states after stopping inflow, the core area is wetter than in the surrounding area and hence, the hydraulic conductivity is higher than fringe zones.

Following the cessation of water supply and subsequent drainage to the finger, the water content in the finger core, the outer limit of the core, and fringe areas will drain to new states on the soil-water characteristic curve with different drainage curves as shown in Fig. 5.26. The dye infiltration clearly show that the non-uniform saturation profile observed after fingering exists for long periods of time and that the locations of the original core areas were slightly wetter than in the surrounding fringe areas. Since the finger core is initially wetter than the fringe region, its hydraulic conductivity is higher than the fringe zone at the same suction. The persistence of fingering is a direct consequence of the hydraulic conductivity of the core area and hence, the subsequent infil-

tration enters through the finger core areas established previously. Therefore, fingers have a water phase memory formed in the first experiment, so fingers formed in subsequent redistribution cycles followed the same flow paths that had been produced by the fingers in the previous cycle, even after 5 days had elapsed.

5.9. Effects of High Initial Water Content

Only a limited number of experiments exists on the effects of initial moisture content on gravity-driven instability, most likely due to the difficulty of measuring and controlling initial moisture fields. However, the limited available evidence does imply that initial moisture content has a fundamental impact on finger behavior, and as such, warrants additional investigation. Experiments in porous media suggest that the occurrence of wetting front instability in uniform moisture field is a function of the initial moisture content. The effects of uniform initial moisture content on finger development were explored in a series of experiments by Diment and Watson (1985) where they found that as the uniformly distributed initial moisture content increased, gravity fingering became less distinct. They noted that wetting front is stabilized and eliminated the instability during redistribution when the initial moisture content was raised above a few percent. Recent experiments by Wang *et al.* (2003), however, show the fingers generated under initial moisture condition and the observed fingers were significantly slower and wider than when the soil was dry.

We designed an experiment to see the effects of initial water moisture on wetting front instability and if fingering in initially and uniformly quite wet sand would occur. In this experiment, we started with water infiltration through initially dry sand and observed the flow fingers. Then the cell was saturated with water from below of the cell to depth 0.3 m step by step (to minimize the air entrapments). After saturation, the cell was allowed to slowly drain for 24 hours to obtain of the hydrostatic pre-wetted system. The moisture content field at the end of the drainage cycle formed the initial moisture field for the second infiltration experiment in pre-wetted sand. A uniform moisture saturation of about 0.5 in the pre-wetted layer resulted and was more or less constant with depth. For the second infiltration cycle we added water in the cell but the wetting front was not visible in pre-wetted sand. To this end in the subsequent infiltration, we used dye tracer to better visualization of flow through the cell (Fig. 5.27). Both applied water and dye were at flow rate of

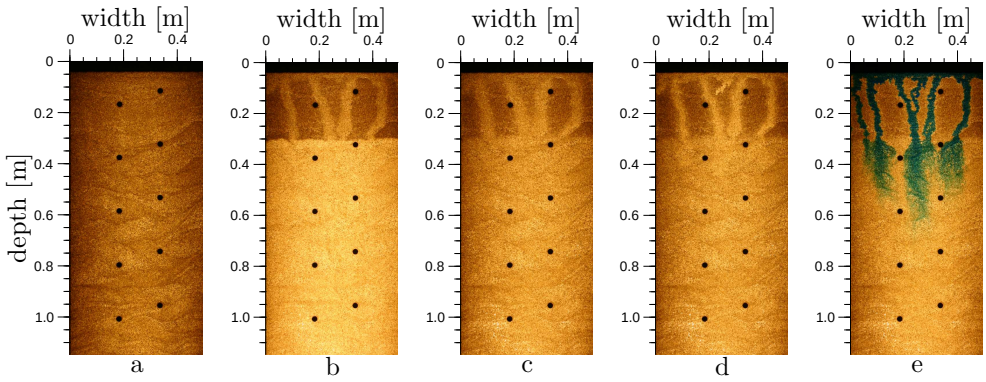

Figure 5.27.: Photographs of the experiment for effects of uniform initial water content on flow fingers. Images **a,b** and **c** are dry, saturated and desaturated (uniform pre-wetted) cell, respectively. Images **d** and **e** are the second cycle of water and dye infiltration where dye tracer redistribution shows the transverse dispersion and diffused flow in pre-wetted region. Black points distributed over the cell are the clips that we used to avoid any bending of the glass plates due to the hydrostatic pressure during the imbibition to saturation of the cell.

$1.2\,\mathrm{mm\,min^{-1}}$.

The dye flow redistribution was stable in fine layer and then at the top dye followed the water fingers path established during the first cycle in the initially dry sand. When the fingers penetrate the pre-wetted sand, a much stronger lateral diffusion than in the dry sand emerges (Fig. 5.27). Thus, we observed that the dye flow was non-uniform and transported with a small transverse dispersion and more diffuse in the pre-wetted sand.

The behavior of the flow in uniform pre-wetted condition in this experiment directly corroborated the results observed by Diment and Watson (1985), however, realizing at a higher initial moisture saturation (0.5) than their experiments.

The common description of flow saturation in initially dry sand cannot be used in the sand with non-uniform (as formed by full development of the two-region core and fringe flow by fingering in initially dry sand) initially moisture content. The finger flow features that form initially non-uniform moisture content do not exhibit a saturated tip with drainage behind, as is seen under initially dry conditions (Glass and Nicholl 1996).

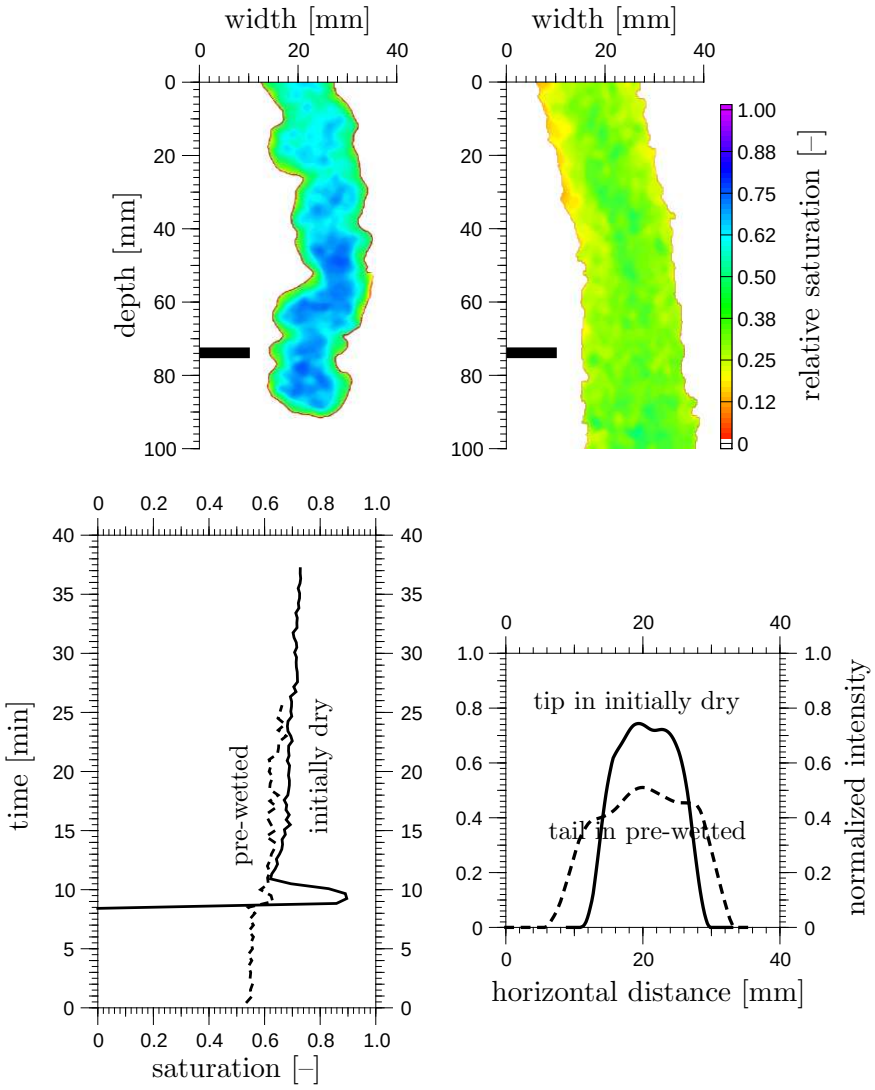

Figure 5.28.: The longitudinal and transverse dynamics of water saturation through one finger in initially dry and non-uniform pre-wetted sand. The longitudinal saturation measurements were done at the small area inside the finger tip and the transverse saturation was taken at 74 cm depth. Note that the maximum displayed saturation is ∼0.8 which is measured in initially dry condition. The small difference in saturation for finger tail between initially dry and pre-wetted condition (bottom right) cab be explained by entrapped air from the initial moisture content within the initial water finger.

Figure 5.28 compares the longitudinal and transverse saturation through one finger at a fixed location (indicated by black line) in initially dry and non-uniform initial pre-wetted condition. In the longitudinal temporal dynamics of water saturation inside the finger core at a fixed location, the large difference in saturation at the finger tip between these two conditions can be clearly seen. Thus saturated zone at the finger tip, which is characteristic for dry sand, did not occur in the pre-wetted sand. Comparison of the water saturation inside the finger core between these two conditions shows that the water saturation along the finger in the pre-wetted sand remained approximately the same as dry sand. The horizontal transect of the water saturation through flow finger shows the water saturation inside the finger core reduces in pre-wetted sand in comparison with dry sand, i.e, there is no more finger tip in pre-wetted sand. The cross-sectional area of the finger in the pre-wetted sand is larger than in the dry sand.

6. Summary and Conclusions

This thesis is a new look on unstable fingering flow generated from ponded infiltration into an initially dry two-layered sand, where a fine-textured layer overlies a coarse-textured layer. For multi-layered systems, the fingers disappear when they encounter heterogeneous layer and reappear as the flow enters a homogeneous coarse region.

We developed a unique, high resolution, 2D transmitted light imaging system to use for quantitative imaging of transient and steady state flows in porous media. The Light Transmission Method (LTM) is a nondestructive and simple tool that permits visualization and measurement of water saturation in Hele-Shaw cells with a high spatial (millimeters) and temporal (seconds) resolution. This technique also opens promising perspectives for investigation of multiphase phenomenon. We further improved the LTM to measure the dynamics of water in Hele-Shaw cells. This was achieved by adding a deconvolution procedure to correct the measurements for light scattering. This technique was used to visualize and analyze, qualitatively and quantitatively, fingering phenomena. The transmitted light intensity was calibrated to absolute water content values calculated from X-ray attenuation data. Thereby, we used intensity of transmitted light as a proxy for water content and hence, the changing water content within flow fingers could be measured in great detail.

After the water fingers fully developed, we used dye tracer to visualize the velocity field within the flow fingers. Infiltration of dye tracer into stabilized water fingers highlights the separation of the water phase into a mobile component (core) and an immobile one (fringe).

The experiments to investigate the structure of the fingering flow were examined in different conditions. Individual fingers initiated from interface between the fine and the coarse layer are typically observed to separate into two regions, a saturated tip that advances downward and a partially drained region behind the finger tip. The longitudinal saturation dynamics profile shows that it decreases immediately behind the tip and slightly increases again towards

longer distance from the tip and then becomes steady over time in finger core. The transverse saturation profile shows a maximum in the center of the fingers and slow lateral movement of the moisture from finger core regions creates less saturated surrounding finger. Hence, the fully developed fingers consist of a high saturated tip, a core with mobile water and a hull with immobile water fringe and once a finger is developed, the saturation profile along its core is invariant as the tip progresses.

The simultaneous measurements of pressure and saturation definitively show the nonuniform moisture profiles in flow paths created by fingered flow. In the evaluation of hydraulic states to describe the dynamics and stabilization of fingers, we demonstrated that the water content and matric potential at the wetting front of unstable fingered flow are on the wetting curve and behind the front are on the drying curve of the soil-water characteristic curve.

Based on the experimental results, we propose two stages of lateral expansion for fingers: a fast expansion in a short time to core stabilization and a slow and steadily expansion for long time to fringe lateral growth. The finger core stabilization well expressed by the interface between the finger core and the fringe zone approaching to the same potential on different hysteresis loop of soil-water characteristic curve, even through the water contents are quite different. A large fringe lateral expansion, however, is expressed by a hydraulic conductivity and water pressure gradient between the outer limit of the core and the fringe region of finger. This is severely hindered by the low conductivity in this dryer range and by the limited supply of water and as long as the matric potential in finger core is smaller than the surrounding zone, finger grows. Hence, within the core of the fingers, the fast convective flow is driven by gravity while at the boundaries (fringes), flow is slow and diffusive.

The fingered flow are highly dependent on the porous medium properties, infiltration fluxes, and the initial and boundary conditions. The dependence of the finger moisture content, width, velocity, and occupied area by fingers as a function of the flux was examined through experiments under different flow rates infiltration. High flow rate produces wider, faster, and more fingers. The finger merging is stated to be an important process, increasing the velocity and width of continuing finger and reducing the number of fingers with depth.

Fingers can persist in the same location for a long time. It is shown that the water content at the finger core and the position of the hydraulic states of

the wetting curve relative to the drying curve are key factors in the persistence of the fingers. Therefore, fingers have a water phase memory formed in the first cycle of infiltration and the subsequent infiltration events persists into the core-fringe region structure followed on the previous finger paths, even after 5 days had elapsed.

The instability of the wetting fronts is eliminated and does not exhibit a saturated tip during redistribution when the initial moisture content of medium raises above a few percent.

In outlook of this work, we note a few main findings:

- Flow fingers in coarse textured sand are destroyed by finer textured inhomogeneities, but they reappear as the flow enters a uniform region.
- We improved the light transmission method to get the real visualization of fingers through deconvolution using point spread function.
- Through parallel measurements of X-ray absorption and light transmission method, we found a good agreement between these two techniques.
- Our experiments confirm the frequently observed overshoot in water saturation within the tip of flow fingers.
- As a new observation, the water saturation in the core of the finger has a minimum immediately behind the tip and increases again towards a constant value at larger distance from the tip.
- The width of flow fingers increases initially and reaches a quasi-stable state at the same time when the water saturation within the core becomes quasi-stable.
- The water within the finger is sharply separated into a core and a fringe with fast convective flow in the core and slow diffusive flow in the fringe.
- When two fingers are present, they are in hydraulic communication and in general the velocities of their tips are not constant and are anti-correlated.
- In the overlying fine-textured layer, pressure drops upon initialization of a new finger.

- Once the finger is formed, its core is preserved as a wet zone for persistence and the fingers formed in subsequent redistribution cycles followed the same flow paths that had been produced by the fingers in the previous cycle.
- As the uniformly distributed initial moisture content increased, gravity fingering becomes border and less distinct.

All observed phenomena, with the exception of saturation overshoot, could be consistently explained based on the hysteretic behavior of the soil-water characteristic. This research was an effort of laboratory experiment to investigate the unstable flow in unsaturated porous media and to identify the processes and mechanism of fingered flow.

Bibliography

Baker, R. S. and Hillel, D., 1990. Laboratory tests of a theory of fingering during infiltration into layered soils, *Soil Sci. Soc. Am. J.* **54**:20–30.

Banham, M. R. and Katsaggelos, A. K., 1997. Digital image restoration, *IEEE Signal Processing Magazine.* **14, issue 2**:24–41.

Bänninger, D. 2004. *Remote soil texture recognition*, Phd thesis, ETH Zürich, Nr. 15465.

Bänninger, D., Lehmann, P. and Flühler, H., 2005. Modelling the effect of particle size, shape and orientation of light transfer through porous media, *Europ. J. Soil Sci.* S. doi: 10.1111/j.1365–2389.2005.00787.x.

Bauters, T. W. J., DiCarlo, D. A., Steenhuis, T. S. and Parlange, J.-Y., 1998. Preferential flow in water-repellent sands, *Soil Sci. Soc. Am. J.* **62**:1185–1190.

Bauters, T. W. J., DiCarlo, D. A., Steenhuis, T. S. and Parlange, J.-Y., 2000. Soil water dependent wetting front characteristics in sands, *J. Hydrol.* **231-232**:244–254.

Bayer, A. 2005. *X-ray attenuation techniques to explore the dynamics of water in porous media*, Phd thesis, University of Heidelberg.

Bayer, A., Vogel, H.-J. and Roth, K., 2004. Direct measurement of the soil water retention curve using x-ray absorption, *Hydrol. Earth Syst. Scienc.* **8**:2–7.

Bear, J. 1972. *Dynamics of fluids in porous media*, Elsevier, New York.

Bell, J., Selker, J. S., Steenhuis, T. S. and Glass, R. J., 1991. Rapid moisture measurement in thin sand slabs, *Presentation at the international winter meeting of ASAE. Chicago,IL.Paper.* **90**:26–35.

Beven, K. and Germann, P., 1982. Macropores and water flow in soils, *Water Resour. Res.* **18**:1311–1325.

Biemond, R. L. L. and Mersereau, A. R. M., 1990. Iterative methods for image deblurring, *Proc IEEE.* **78(5)**:856–883.

Bones, P. J., Satherley, B. L. and Watson, R. W., 1992. Direct deconvolution of noisy blurred images blind image deconvolution, *Image Processing and its Applications, International Conference on.* S. 353–356.

Bowman, B. T., Brunke, R. R., Reynolds, W. D. and Wall, G. J., 1994. Rainfall simulator-grid lysimeter system for solute transport studies using, large, intact soil blocks, *J. Environ. Qual.* **23**:815–822.

Brooks, R. H. and Corey, A. T., 1966. Properties of porous media affecting fluid flow, *J. Irrigation and Drainage Div., Proc. Am. Soc. Civil Eng. (IR2)* **92**:61–88.

Buckingham, E. 1907. Studies on the movement of soil moisture, *Bull.38* S. USDA, Department of Agriculture, Bureau of soils, Washington, DC.

Cheng, Z. 2004. *Characterization of water flow and solute transport in coarse textured materials*, Phd thesis, University of Heidelberg.

Chouke, R. L., van Meurs, P. and van der Poel, C., 1959. The instability of slow immiscible, viscous liquid-liquid displacements in permeable media, *Trans. AIME.* **216**:188–194.

Cornell-Website .,2003. Preferential Flow WebSite, Department of Biological and Environmental Engineering, Cornell University, http://soilandwater.bee.cornell.edu/Research/pfweb.

Darcy, H. 1856. *Les Fontaines de la Ville de Dijon*, Dalmont, Paris.

Darnault, C. J. G. 2001. Measurement of fluid contents by light transmission in transient three-phase oil-water-air systems in sand, *Water Resour. Res.* **37**:1859–1868.

Darnault, C. J. G., DiCarlo, D. A., Bauters, T. W. J., Steenhuis, T., Parlange, J.-Y., Montemagno, C. D. and Baveye, P., 2002. Visualization and measurement of multiphase flow in porous media using light transmission and synchrotron X-rays, *Ann. N.Y. Acad. Sci.* **972**:103–110.

Darnault, C. J. G., Throop, J. A., DiCarlo, D. A., Rimmer, A., Steenhuis, T. and Parlange, J.-Y., 1998. Visualization by light transmission of oil and water content in transient two-phase flow fields, *J. Contam. Hydrol.* **31**:337–348.

Deinert, M., Parlange, J.-Y., Steenhuis, T. S., Ünlü, K., Selker, J. and Cady, K. B., 2002. Real-time measurement of water profiles in a sand using neutron radiography, *Proceedings of Hydrology Days.* S. 56–63.

Deinert, M., Parlange, J.-Y., Steenhuis, T. S., Ünlü, K., Selker, J. and Cady, K. B., 2004. Measurement of fluid contents and wetting front profiles by real-time neutron radiography, *J. Hydrol.* **290**:192–201.

Dekker, L. W. and Ritsema, C. J., 1994. How water moves in a water repellent sandy soil: 1. Potential and actual water repellency, *Water Resour. Res.* **30(9)**:2507–2517.

Deurer, M., Vogeler, I., Khrapitchev, A. and Scotter, D., 2002. Imaging of water flow in porous media by magnetic resonance imaging microscopy, *J. Environ. Qual.* **31**:487–493.

DiCarlo, D. A. 2004. Experimental measurements of saturation overshoot on infiltration, *Water Resour. Res.* **40**:W04215,doi:10.1029/2003WR002670.

DiCarlo, D. A. 2005. Modeling observed saturation overshoot with continuum additions to standard unsaturated theory, *Advances in Water Resources* **28**:10211027.

DiCarlo, D. A. and Blunt, M. J., 2000. Determination of finger shape using the dynamic capillary pressure, *Water Resour. Res.* **36(9)**:2781–2785.

DiCarlo, D. A., Bauters, T. W. J., Darnault, C. J. G., Steenhuis, T. S. and Parlange, J.-Y., 1999. Lateral expansion of preferential flow paths in sands, *Water Resour. Res.* **35(2)**:427–434.

DiCarlo, D. A., Bauters, T. W. J., Steenhuis, T. S., Parlange, J.-Y. and Bierck, B. R., 1997. High-speed measurements of three-phase flow using synchrotron X-rays, *Water Resour. Res.* **33(4)**:569–576.

Diment, G. A. and Watson, K. K., 1985. Stability analysis of water movement in unsaturated porous materials, 3: Experimental studies, *Water Resour. Res.* **21(7)**:979–984.

Diment, G. A., Watson, K. K. and Blennerhassett, P. J., 1982. Stability analysis of water movement in unsaturated porous materials, 1: Theoretical considerations, *Water Resour. Res.* **18(4)**:1248–1254.

Dullien, F. A. 1992. *Porous Media: Fluid Transport and Pore Structure*, Academic Press, California.

Egorov, A. G., Datov, R. Z., Nieber, J. L. and Sheshukov, A. Y., 2003. Stability analysis of gravity-driven infiltration flow, *Water Resour. Res.* **39(9)**:W1266,doi:10.1029/2002WR001886.

Eliassi, M. and Glass, R. J., 2001. On the continuum-scale modeling of gravity-driven fingers in unsaturated porous media: The inadequacy of the Richards equation with standard monotonic constitutive relations and hysteretic equations of state, *Water Resour. Res.* **37(8)**:2019–2035.

Eliassi, M. and Glass, R. J., 2002. On the porous-continuum modeling of gravity-driven fingers in unsaturated materials: Extension of standard theory with a hold-back-pile-up effect, *Water Resour. Res.* **38**:W1234,doi:10.1029/2001WR001131.

Eliassi, M. and Glass, R. J., 2003. On the porous-continuum modeling of gravity-driven fingers in unsaturated materials: Numerical solution of a hypodiffusive governing equation that incorporates a hold-back-pile-up effect, *Water Resour. Res.* **39**:W1167,doi:10.1029/2002WR001535.

Ferrand, L. A., Milly, P. C. D. and Pinder, G. F., 1986. Dual-gamma attenuation for the determination of porous medium saturation with respect to three fluids, *Water Resour. Res.* **22(12)**:1657–1663.

Flekkøy, E. G., Schmittbuhl, J., Løvoll, F., Oxaal, U., Måløy, K. J. and Aagaard, P., 2002. Flow paths in wetting unsaturated flow: Experiments and simulations, *Phys.Rev.E.* **65**:036312.

Friedman, S. P. 1999. Dynamic contact angle explanation of flow rate-dependent saturation-pressure relationships during transient liquid flow in unsaturated porous media, *J. Adhes. Sci. Technol.* **13**:1495–1518.

Geiger, S. L. and Durnford, D. S., 2000. Infiltration in homogeneous sands and a mechanistic model of unstable flow, *Soil Sci. Soc. Am. J.* **64**:460–469.

Glass, R. J. and Nicholl, M. J., 1996. Physics of gravity fingering of immiscible fluids within porous media: An overview of current understanding and selected complicating factors, *Geoderma.* **70**:133–163.

Glass, R. J. and Yarrington, L., 2003. Mechanistic modeling of fingering, nonmonotonicity, fragmentation, and pulsation within gravity/buoyant destabilized two-phase/unsaturated flow, *Water Resour. Res.* **39(3)**:doi:10.1029/2002WR001542.

Glass, R. J., Parlange, J.-Y. and Steenhuis, T. S., 1991. Immiscible displacement in porous media: Stability analysis of three-dimensional, axisymmetric disturbances with application to gravity-driven wetting front instability, *Water Resour. Res.* **27(8)**:1947–1959.

Glass, R. J., Steenhuis, T. S. and Parlange, J.-Y., 1989a. Wetting front instability, 1: Theoretical discussion and dimensional analysis, *Water Resour. Res.* **25(6)**:1187–1194.

Glass, R. J., Steenhuis, T. S. and Parlange, J.-Y., 1989b. Wetting front instability, 2: Experimental determination of relationships between system parameters and two-dimensional unstable flow field behavior in initially dry porous media, *Water Resour. Res.* **25(6)**:1195–1207.

Glass, R. J., Steenhuis, T. S. and Parlange, J.-Y., 1989c. Mechanism for finger persistence in homogeneous unsaturated porous media: Theory and verification, *Soil Sci.* **148**:60–70.

Gonzales, R. C. and Woods, R. E., 1993. *Digital Image Processing*, Addison-Wesley Publishing Company, Messachusettes, Menlo Park, California, New York.

Green, W. H. and Ampt, G. A., 1911. Studies of soil physics. I. The flow of air and water through soils, *J. Ag. Sci.* **4**:1–24.

Hill, D. E. and Parlange, J.-Y., 1972. Wetting front instability in layered soils, *Soil Sci. Soc. Am. Proc.* **36**:697–702.

Hill, S. 1952. Channeling in packed columns, *Chem. Eng. Sci.* **1**:247–253.

Hillel, D. and Baker, R. S., 1988. A descriptive theory of fingering during infiltration into layered soils, *Soil Sci.* **146**:51–56.

Hoa, N. T. 1981. A new method allowing the measurement of rapid variations of the water content in sandy porous media, *Water Resour. Res.* **17(1)**:41–48.

Hoa, N. T., Gaudu, R. and Thirriot, C., 1977. Influence of the hysteresis effect on transient flows in saturated-unsaturated porous media, *Water Resour. Res.* **13(6)**:992–996.

Jähne, B. 2002. *Digital Image Processing*, 5th edn, Springer, Berlin, Germany.

Jaynes, D. B. 1992. Estimation hysteresis in the soil water retention function, In F. J. L. M. Th. van Genuchten and Lund, L. J., (ed.), *Indirect Methods for Estimating the Hydraulic Properties of Unsaturated Soils* S. University of California, Riverside, CA 92521,S.115–124.

Johns, M. L. and Gladden, L. F., 1998. MRI study of non-aqueous phase liquid extraction from porous media, *Magn. Reson. Imaging.* **16**:655–657.

Jury, W. A., Wang, Z. and Tuli, A., 2003. A conceptual model of unstable flow in unsaturated soil during redistribution, *Vadose Zone J.* **2**:61–67.

Jury, W. M., Gardner, W. R. and Gardner, W. H., 1991. *Soil Physics*, 5th, John Wiley & Sons, New York, United States of America.

Klute, A. and Dirksen, C., 1986. *Methods of soil analysis*, chapter Hydraulic conductivity and diffusivity: Laboratory methods. S. 687–734, Part 1. Physical and Mineralogical Methods, 2nd edn, American Society of Agronomy, Madison, Wisconsin.

Kundur, D. and Hatzinakos, D., 1996. Blind image deconvolution, *IEEE Signal Processing Magazine.* **13, issue 3**:43–64.

Kung, K.-J. S. 1990a. Preferential flow in a sandy vadose zone, 1: Field observation, *Geoderma.* **46**:51–58.

Kung, K.-J. S. 1990b. Preferential flow in a sandy vadose zone, 2: Mechanisms and implications, *Geoderma.* **46**:59–71.

Kutìlek, M. and Nielsen, D. R., 1994. *Soil Hydrology*, Catena Verlag.

Langmaack, M., Schrader, S., Rapp-Bernhardt, U. and Kotzke, K., 1999. Quantitative analysis of earthworm burrow systems with respect to biological soil-structure regeneration after soil compaction, *Biol. Fertil. Soils* **28**:219–229.

Larsson, M. H. and Jarvish, N. J., 1999. Evaluation of a dual-porosity model to predict field-scale solute transport in a macroporous soil, *J. Hydrol.* **215**:153–171.

Lawes, J. B., Gilbert, J. H. and Warington, R., 1882. On the amount and composition of the rain and drainage water collected at rothamstead, *J. Royal Agr. Soc. of England.* **XVIII**:1–71.

Lehmann, P., Stauffer, F., Hinz, C., Dury, O. and Flühler, H., 1998. Effect of hysteresis on water flow in a sand column with a fluctuating capillary fringe, *J. Contam. Hydrol.* **33**:81–100.

Liu, Y., Bierck, R., Selker, J., Steenhuis, T. S. and Parlange, J.-Y., 1993. High intensity x-ray and tensiometry measurements in rapidly changing preferential flow fields, *Soil Sci. Soc. Am. J.* **57**:1188–1192.

Liu, Y., Steenhuis, T. S. and Parlange, J.-Y., 1994a. Formation and persistence of fingered flow fields in coarse grained soils under different moisture contents, *J. Hydrol.* **159**:187–195.

Liu, Y., Steenhuis, T. S. and Parlange, J.-Y., 1994b. Closed form solution for finger width in sandy soils at different water content, *Water Resour. Res.* **30(4)**:949–952.

McBride, J. F. and Miller, C. T., 1994. Nondestructive measurements of phase fractions in multiphase porous-media experiments by using x-ray attenuation, *Cent. Multiphase Res. News* **1**:10–13.

Méheust, Y., Løvoll, G., Måløy, K. J. and Schmittbuhl, J., 2002. Interface scaling in a two-dimensional porous medium under combined viscous, gravity,and capillary effects, *Phys. Rev. E.* **66**:051603.

Menon, M., Robinson, B., Oswald, S. E., Kaestner, A., Abbaspour, K. C., Lehmann, E. and Schulin, R., 2006. Visualization of root growth in heterogeneously contaminated soil using neutron radiography, *Europ. J. Soil Sci.* S. doi.10.1111/j.1365–2389.2006.00870.x.

Mortensen, A. P., Glass, R. J., Hollenbeck, K. and Jensen, K. H., 2001. Visualization of microscale phase displacement processes in retention and outflow experiments: nonuniqueness of unsaturated flow properties, *Water Resour. Res.* **37(6)**:1627–1640.

Niemet, M. and Selker, J., 2001. A new method for quantification of liquid saturation in 2D translucent porous media system using light transmission, *Advances in Water Resources* **24**:651–666.

Niemet, M., Rockhold, M., Weisbrod, N. and Selker, J., 2002. Relationships between gas-liquid interfacial surface area, liquid saturation, and light transmission in variably saturated porous media, *Water Resour. Res.* **38(8)**:W01135,doi:10.1029/2001WR000785.

Oostrom, M., Dane, J. H., Missildine, B. C. and Lenhard, R. J., 1995. Error analysis of dual-energy gamma radiation measurements, *Soil Sci.* **160**:28–42.

Parlange, J.-Y. 1976b. Capillary hysteresis and the relationship between drying and wetting curves, *Water Resour. Res.* **12**:224–228.

Parlange, J.-Y. and Hill, D. E., 1976a. Theoretical analysis of wetting front instability in soils, *Soil Sci.* **122**:236–239.

Philip, J. 1975a. Stability analysis of infiltration, *Soil Sci. Soc. Am. Proc.* **39**:1042–1049.

Philip, J. 1975b. The growth of disturbances in unstable infiltration flows, *Soil Sci. Soc. Am. Proc.* **39**:1049–1053.

Pires, L. F., Bacchi, O. O. S. and Reichardt, K., 2005. Gamma ray computed tomography to evaluate wetting/drying soil structure changes, *Nucl. Inst. Meth. Phys. Res.* **229**:443–456.

Pivetz, B. E. and Steenhuis, T. S., 1995. Soil matrix and macropore biodegradation of 2,4-d, *J. Environ. Qual.* **24**:564–570.

Press, W. H., Teukolsky, S. A., Vetterling, W. T. and Flannery, B. P., 1992. *Numerical Recipes in C*, Cambridge University Press.

Raats, P. A. 1973. Unstable wetting fronts in uniform and nonuniform soils, *Soil Sci. Soc. Am. Proc.* **37**:681–685.

Richards, L. A. 1931. Capillary conduction of liquids through porous mediums, *Physics* **1**:318–333.

Ritsema, C. J. and Dekker, L., 1995. Distribution flow: A general process in the top layer of water repellent soils, *Water Resour. Res.* **31(5)**:1187–1200.

Roth, K. 2006. *Soil Physics. Lecture Notes*, Institute of Environmental physics, University of Heidelberg, http://www.iup.uni-heidelberg.de/institut/forschung/groups/ts/students.

Saffman, P. G. and Taylor, G., 1958. The penetration of a fluid into a porous medium or hele-shaw cell containing a more viscous liquid, *Proc. R. Soc. London,* **245**:312–329.

Schumacher, W. 1864. *Die Physik des Bodens*, Berlin.

Selker, J. S., Parlange, J.-Y. and Steenhuis, T. S., 1992a. Fingered flow in two dimensions, 2: Measurement of matric potential, *Water Resour. Res.* **28(9)**:2513–2521.

Selker, J. S., Parlange, J.-Y. and Steenhuis, T. S., 1992b. Fingered flow in two dimensions, 2: Predicting finger moisture profile, *Water Resour. Res.* **28(9)**:2523–2528.

Sideman, S. 2002. Basic highlights of visualization and imaging in transport phenomena, *Ann. N. Y. Acad. Sci.* **972**:1–344.

Ŝimûnek, J., van Genuchten, M. T. and Ŝejna, M., 2005. *The HYDRUS-1D Software Package for Simulating the One-Dimensional Movement of Water, Heat, and Multiple Solutes in Variably-Saturated Media*, Version 3.0, University of California Riverside.

Stagnitti, F., Parlange, J.-Y., Steenhuis, T. S., Nijssen, B. and Lockington, D., 1994. Modelling the migration of water soluble contaminants through preferred paths in the soil, *In Groundwater Quality Management, eds. K. Kovar and J. Soveri* **IAHS Pub. No. 220**:367–379.

Steenhuis, T. S. and Parlange, J.-Y., 1991. Preferential flow in structured and sandy soils, *Preferential Flow. Proceedings of the National Symposium, December 16 - 17, 1991; Chicago, Illinois. T.J. Gish, A. Shirmohammadi (editors). American Society of Agricultural Engineers, St. Joseph, Michigan.* S. 12–21.

Steenhuis, T. S., Boll, J., Shalit, G., Selker, J. S. and Merwin, I., 1994. A simple equation for predicting preferential flow solute concentrations, *J. Environ. Qual.* **23**:1058–1064.

Steenhuis, T. S., Y.-J. Kim, J.-Y. P., Akhtar, M. S., Richards, B. K., Kung, K.-J. S., Gish, T. J., Dekker, L. W., Ritsema, C. J. and Aburime, S. O., 2001. An equation for describing solute transport in field soils with preferential flow paths, *Preferential Flow, Water Movements and Chemical Transport in the Environment. Second International Symposiums Honoluly. ASAE Proceedings.* S. 137–140.

Stöhr, M. 2003. *Analysis of flow and transport in refractive index matched porous media*, Phd thesis, University of Heidelberg.

Tidwell, V. C. and Glass, R. J., 1994. X-ray and visible light transmission for laboratory measurement of two-dimensional saturation fields in thin-slab systems, *Water Resour. Res.* **30(11)**:2873–2882.

Topp, G. C. and Miller, E. E., 1966. Hysteretic moisture characteristics and hydraulic conductivities for glass-bead media, *Soil Sci. Soc. Am. Proc.* **30**:156–162.

van Genuchten, M. T. 1980. A closed-form equation for predicting the hydraulic conductivity of unsaturated soils, *Soil Sci. Soc. Am. J.* **44**:892–898.

Vogel, H.-J. 2006. Quantim: C software library for scientific image processing,www.iup.uni-heidelberg.de/institut/forschung/groups/ts/tools.

Votrubovà, J., Clslerovà, M., Amin, M. H. G. and Hall, L. D., 2003. Recurrent ponded infiltration into structured soil: A magnetic resonance imaging study, *Water Resour. Res.* **39(12)**:doi:10.1029/2003WR002222.

Walter, M. T., Kim, J.-S., Steenhuis, T. S., Parlange, J.-Y., Heiilig, A., Braddock, R. D., Selker, J. S., and Boll, J., 2000. Funneled flow mechanisms in a sloping layered soil: Laboratory investigation, *Water Resour. Res.* **36(4)**:841–849.

Wang, Z., Feyen, J. and Elrick, D. E., 1998. Prediction of fingering in porous media, *Water Resour. Res.* **34(9)**:2183–2190.

Wang, Z., Tuli, A. and Jury, W. A., 2003. Unstable flow during redistribution in homogeneous soil, *Vadose Zone J.* **2**:52–60.

Wang, Z., Wu, L. and Wu, Q. J., 2000. Water-entry value as an alternative indicator of soil water-repellency and wettability, *J. hydrology.* **231-232**:76–83.

Weitz, D. A., Stokes, J. P., Ball, R. C. and Kushnick, A. P., 1987. Dynamic capillary pressure in porous media: Origin of the viscous-fingering length scale, *Phys. Rev. Lett.* **59**:2967–2970.

Wilson, A. 1988. What color is color?, *The Electronic System Design Magazine* S. 38–44.

Yao, T. and Hendrickx, J. M. H., 1996. Stability of wetting fronts in dry homogenous soils under low infiltration rates, *Soil Sci. Soc. Am. J.* **60**:20–28.

A. Appendix

The following figures show the sequence digital images of the fingering patterns observed by light transmission method during water infiltration (A.1), dry tracer infiltration after stabilization of the water fingers (A.2), and experiments of water infiltration under different flow rates (A.3) into an initially dry layered porous medium. For each experiment, the time is indicated below the images.

Readers can find video clip of the fingering flow experiment during water and dye tracer infiltration into a multi-layered medium (A.1 and A.2) in below link:

http://www.hydrol-earth-syst-sci-discuss.net/3/2595/2006/hessd-3-2595-2006-supplement.zip

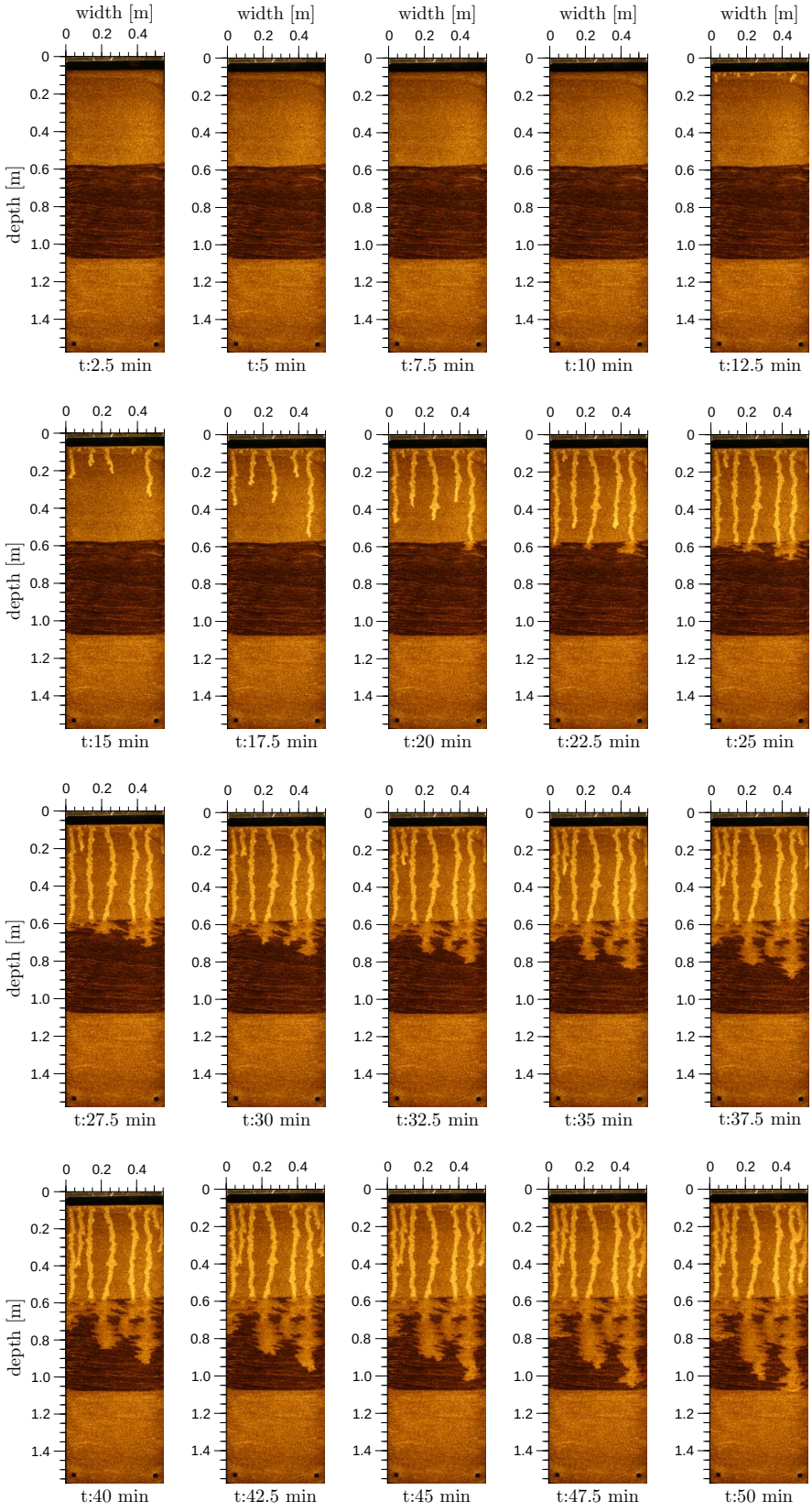
width [m]
depth [m]
t:2.5 min
t:5 min
t:7.5 min
t:10 min
t:12.5 min
t:15 min
t:17.5 min
t:20 min
t:22.5 min
t:25 min
t:27.5 min
t:30 min
t:32.5 min
t:35 min
t:37.5 min
t:40 min
t:42.5 min
t:45 min
t:47.5 min
t:50 min

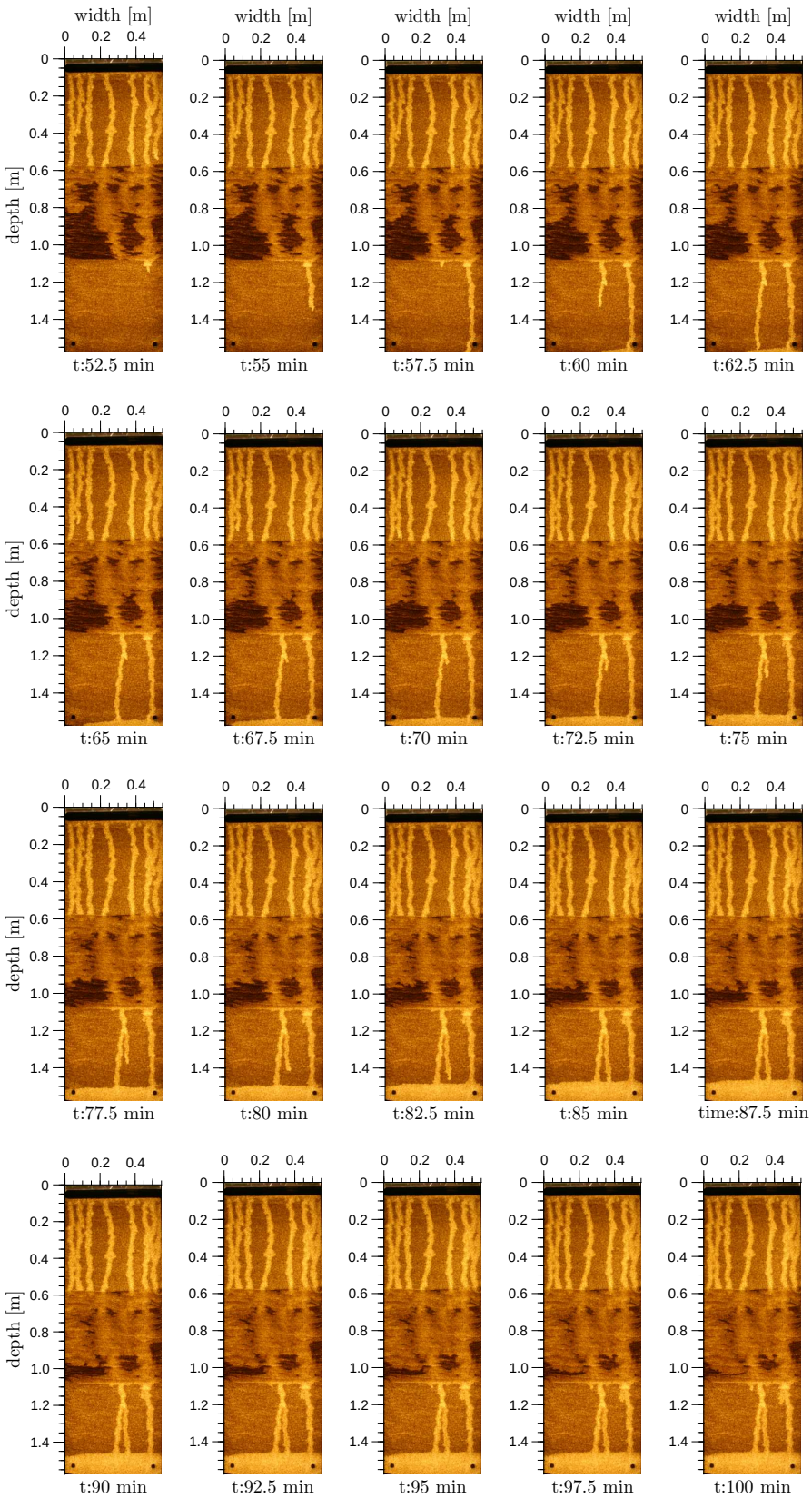

Figure A.1.: Digital images of water fingering experiment into an initially dry porous Hele-Shaw cell observed by light transmission system described in section 5.1 (Fig. 5.1). The time numbers refer to the time after starting of water infiltration.

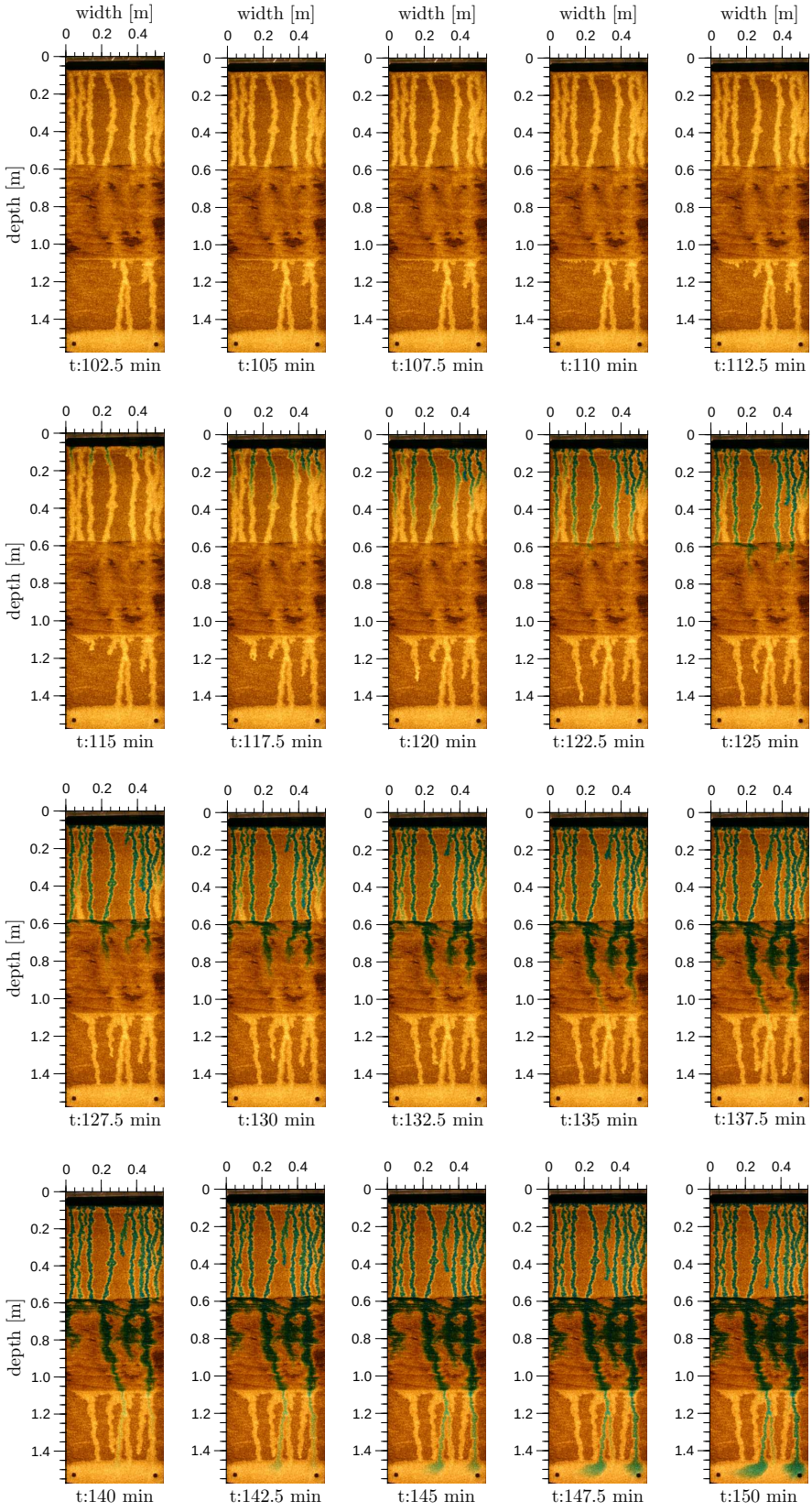
width [m]
depth [m]
t:102.5 min
t:105 min
t:107.5 min
t:110 min
t:112.5 min
t:115 min
t:117.5 min
t:120 min
t:122.5 min
t:125 min
t:127.5 min
t:130 min
t:132.5 min
t:135 min
t:137.5 min
t:140 min
t:142.5 min
t:145 min
t:147.5 min
t:150 min

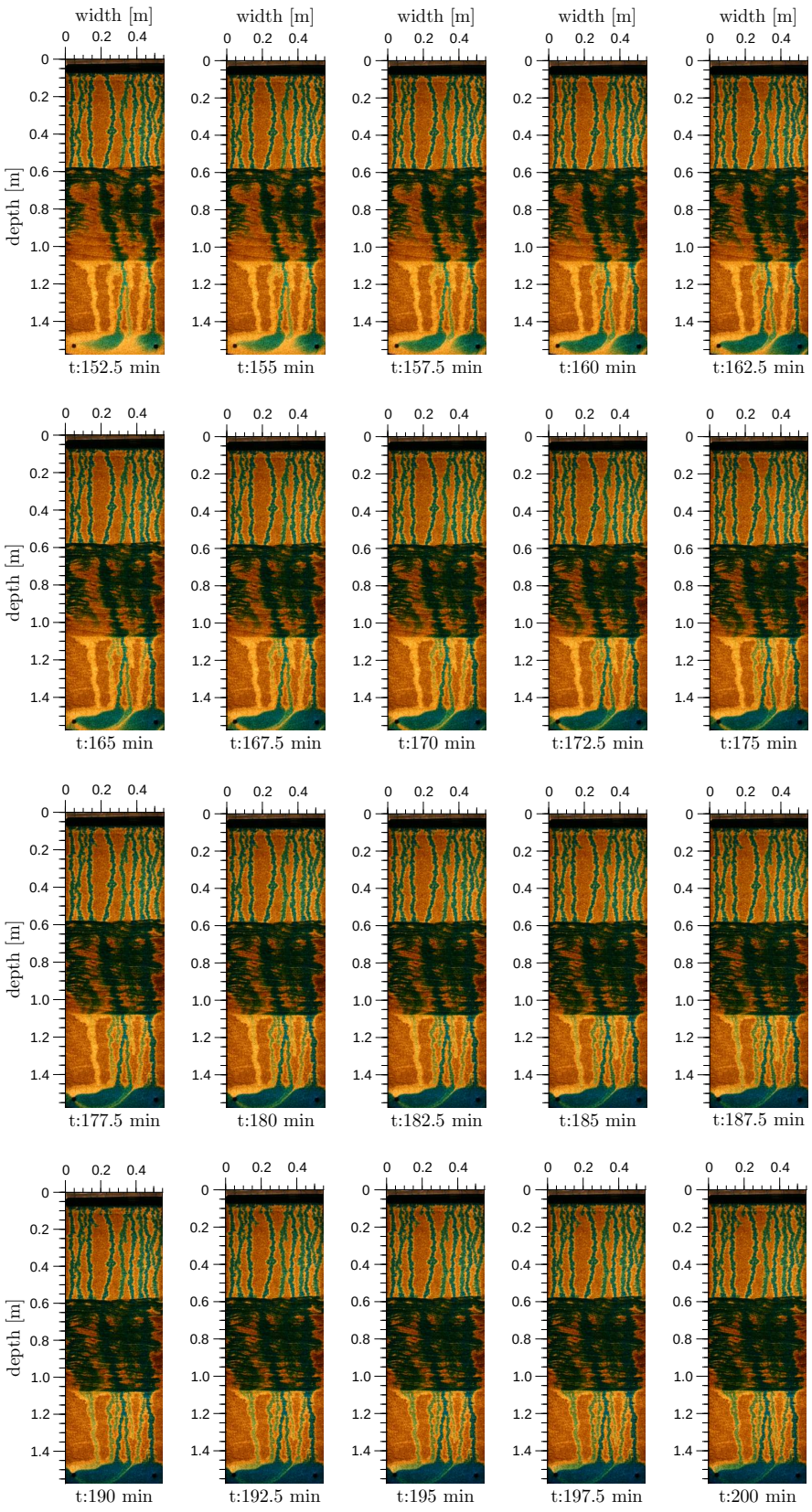

Figure A.2.: Digital images of dye tracer infiltration experiment into stabilized water fingers described in section 5.1 (Fig. 5.4). The time numbers refer to the time after starting of water infiltration.

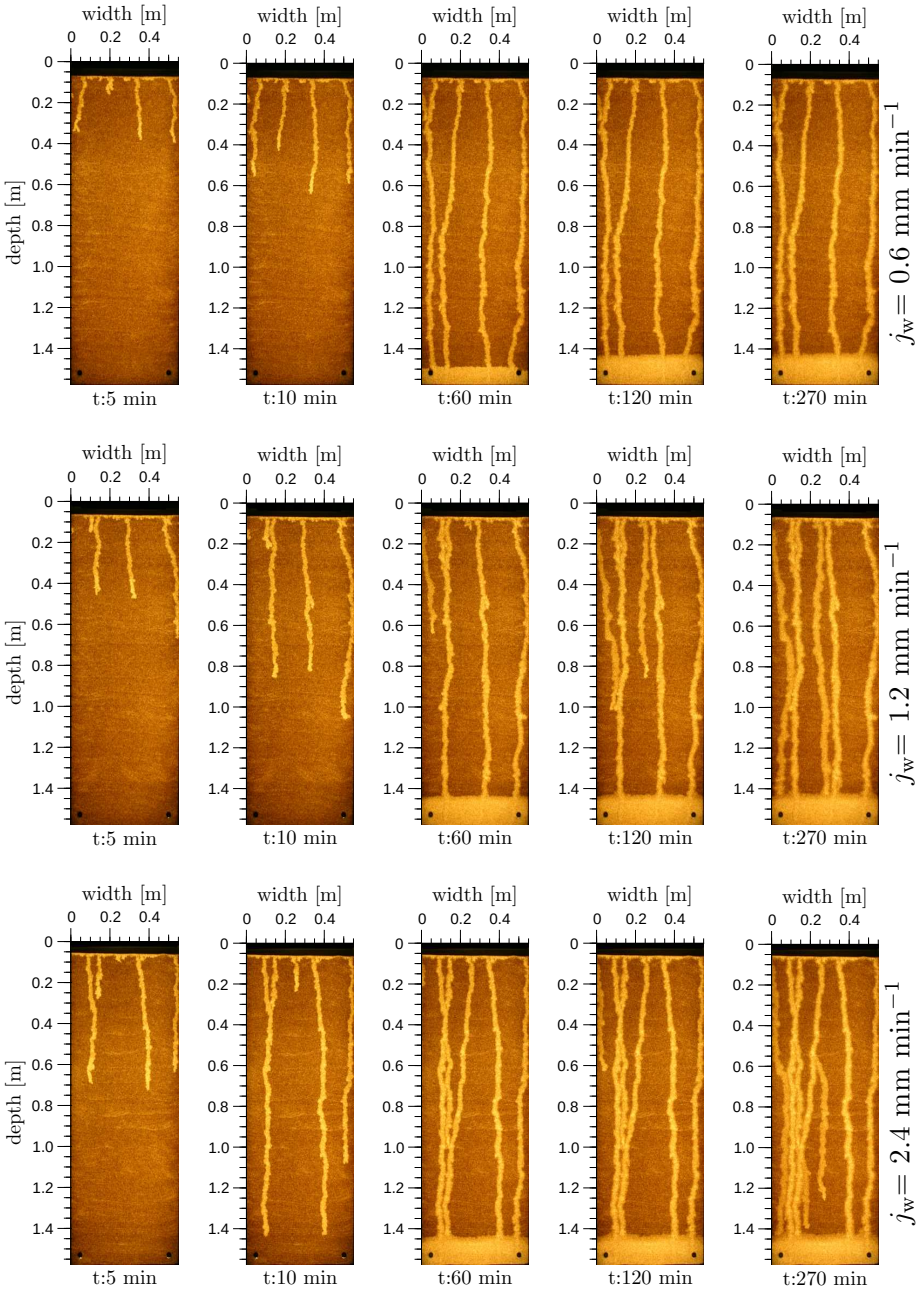
width [m]
0 0.2 0.4
depth [m]
0 0.2 0.4 0.6 0.8 1.0 1.2 1.4
t:5 min
t:10 min
t:60 min
t:120 min
t:270 min
j_w= 0.6 mm min^{-1}
j_w= 1.2 mm min^{-1}
j_w= 2.4 mm min^{-1}

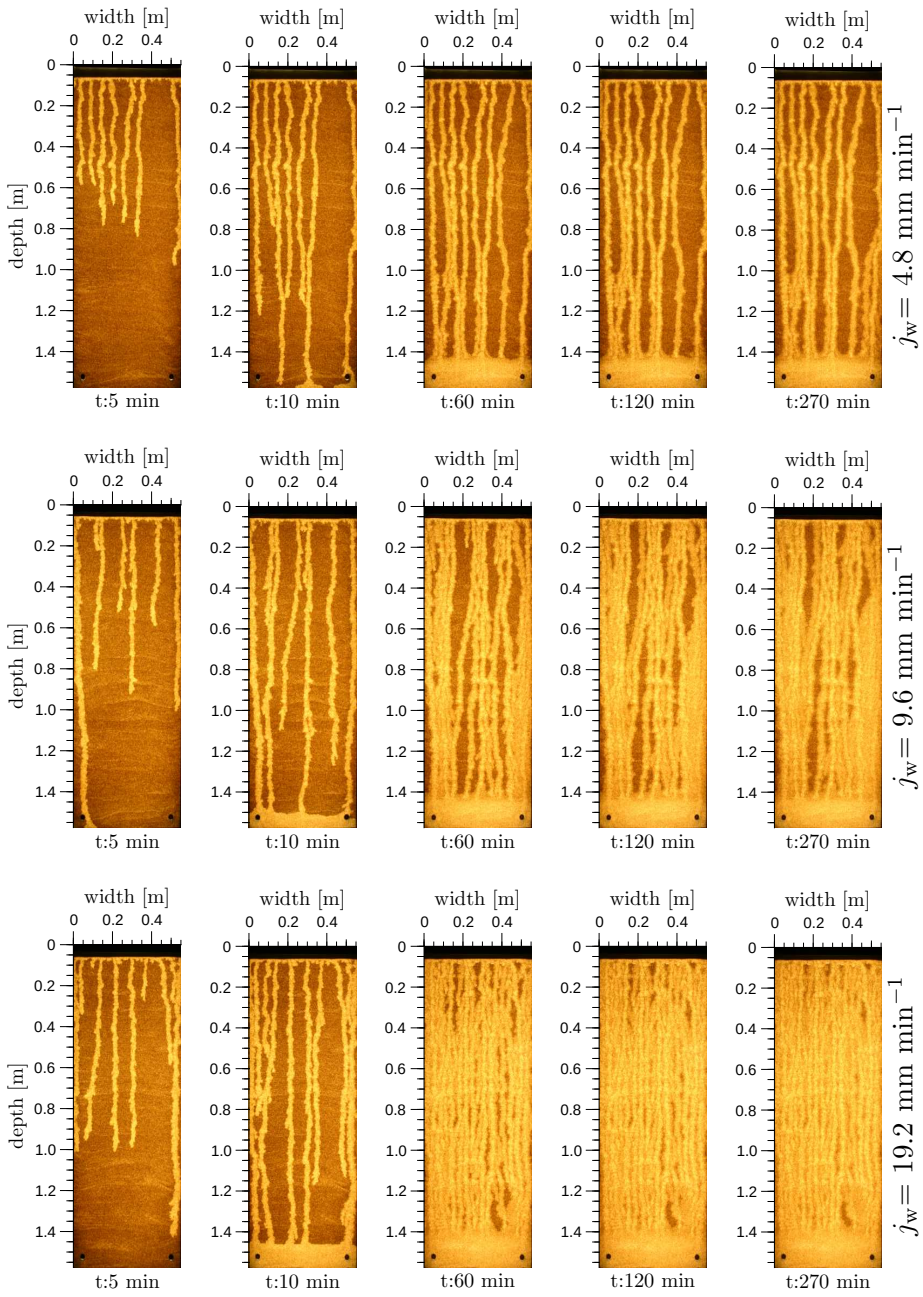

Figure A.3.: Digital images of six separate experiments under different flux infiltration into initially dry porous Hele-Shaw cells. The flow rates are indicated in the right side of the images for each experiment. The time numbers refer to the time after starting initiation of fingers in interface between the fine and the coarse layer.

Acknowledgments

In this project I got help of an enormous number of people which supported and encouraged me in making this work a success. I hope that I didn't forget someone in the following list. So for safety's sake:

I would like to express my heartfelt thanks to everyone who helped me with this project as a specialist or as a friend!!!

- *Prof. Kurt Roth* who gave me the opportunity to work on a very interesting project in his group and I would like to extend my heartfelt thanks for his continual support. I appreciate his scientific ideas and contributions for experimental investigations which set this work on a firm basis. He also created a unique and enjoyable working environment as I could not have asked for better supervisor. Thank you so much.

- *Hans-Jörg Vogel* for the scientific impact and his efforts in understanding of the flow in porous media to a PhD student with no experience in this field. He took the most stupid questions seriously, so I dared to contact him for any problems and questions. He provided a friendly environment for discussion and interpretation of data through this project. His advanced library (Quantim) was very useful for image processing analysis.

- *Prof. Bernd Jähne* that agreed to act as second referee on this thesis. I always used his helpful comments from his book and lectures for image processing part of this project.

- *Ute, Olaf, Volker, Andreas, Zhuhua, Holger, Klaus, Carolin, Moritz, Philip, Alexandra, Benedikt, Patrick, Jörg, Anatja, Nadija, Tobias, David, Mathias and Angelika*, my former and current colleagues in soil physics group at the Institute of Environmental Physics, Heidelberg for their support and a friendly atmosphere and fruitful discussions during the last years. And special thanks to *Andreas, Holger* and *Klaus* for helping me for my computer and programming problems. Thanks friends.

- *Guilia, Björn, Florian, Steffan, Jens, Dominik* and *Xia* who helped me for many successful experiments during their Mini-Research course on this project.

- *Andreas Bayer* for experiments and processing of the X-ray data and *Felix Heimann* for writing of the deconvolution algorithm.
- *Carolin, Holger, Ute, Klaus, Sreejith, Masoumeh, Sarah, Fahim* for making valuable hints and corrections of my dissertation.
- Staff of the workshop at the Institute of Environmental Physics for the enormous efforts for the construction of the experimental Set-Up.
- *Homa*, my lovely wife, who with great patience and tolerance carried with me the burden of my PhD and supported me during the stressful times. She has also endured many long hours waiting for me to come from institute and has provided stability to our family. Without you, none of these could happen. I love you forever!
- My wonderful son *Hooman*, his birth brought exceptional joy and happiness to my life.

And last but not least, my family for their encouragements from so far away and all my friends who accompanied me during the last years.

Financial support for this research was provided by Deutsche Forschungsgemeinschaft (DFG) through project RO: 1080-9/1&2.

Fereidoun Rezanezhad, March 2007